Theses, Dissertations, and Student Research: Department of Physics and Astronomy

Physics and Astronomy, Department of

4-2019

Perturbative generalization of nonparaxial ultrashort tightly-focused elegant Laguerre-Gaussian beams

Andrew M. Vikartofsky

University of Nebraska-Lincoln, avikarto@gmail.com

Follow this and additional works at: https://digitalcommons.unl.edu/physicsdiss

Part of the Atomic, Molecular and Optical Physics Commons, and the Optics Commons

Perturbative generalization of nonparaxial ultrashort tightly-focused elegant Laguerre-Gaussian beams

by

Andrew M. Vikartofsky

A DISSERTATION

Presented to the Faculty of

The Graduate College at the University of Nebraska

In Partial Fulfilment of Requirements

For the Degree of Doctor of Philosophy

Major: Physics and Astronomy

Under the Supervision of Professor Anthony F. Starace

Lincoln, Nebraska

April, 2019

Perturbative generalization of nonparaxial ultrashort tightly-focused elegant Laguerre-Gaussian beams

Andrew M. Vikartofsky, Ph.D.

University of Nebraska, 2019

Adviser: Professor Anthony F. Starace

An analytical method for calculating the electromagnetic fields of a nonparaxial elegant Laguerre-Gaussian (eLG) vortex beam is presented for arbitrary pulse duration, spot size, and LG mode. This perturbative approach provides a numerically tractable model for the calculation of arbitrarily high radial and azimuthal LG modes in the nonparaxial regime, without requiring integral representations of the fields. A key feature of this perturbative model is its use of a Poisson-like frequency spectrum, which allows for the proper description of pulses of arbitrarily short duration. The time-domain representation of this model is presented as a non-recursive closed-form expression to any order of perturbative correction. This presentation enables calculation of the complex EM fields for such general beams without requiring evaluation of any Fourier integrals, and is therefore straightforward to implement for both analytical and numerical applications. Other recent models are discussed and compared.

In addition, numerical simulations are carried out in which high energy electron bunches are generated via vacuum acceleration by a tightly focused eLG beam. By examination of accelerated electron properties far from the beam waist, it is shown that eLG beams of higher radial index can increase the electronic energy gain. The utility of such an acceleration model applied to ensemble acceleration is explored, and compared to standard modern techniques.

ACKNOWLEDGMENTS

Thanks to all of my family, friends, colleagues, and co-authors who have helped make this dissertation possible. In particular, I'd like to acknowledge a few individuals whose insights and assistance have been the most influential over the past five years.

Primarily, I would like to thank my advisor, Anthony Starace, for his unending support and guidance. Not only has he encouraged me to attend conferences and workshops for both academic enrichment and professional development, but has always made himself available to resolve any concerns or confusions I've had. Some of my fondest memories for many years to come will surely include our hours of debate while tweaking sentences in manuscript drafts. I only hope that one day, he will learn to cut and paste with the keyboard.

Liang-Wen Pi was a post-doctoral researcher in the Starace group when I started grad school, and has been an excellent mentor for my entire graduate career. Even after leaving the country for another post-doc and ultimately a faculty position, he has provided some of the best criticisms, recommendations, and advice I could have ever asked for. Were it not for his deep insights and breadth of knowledge, I would have traveled a much longer road to becoming a productive researcher.

Andrew Steinacher, a fellow physicist from my undergrad years who currently works at Wolfram, has provided countless assists regarding the nuances of Mathematica. For all the times I found weird bugs, attempted hacky workarounds, and outright broke the software, he consistently found time to help me make it work. His feedback has been critical in the production of many tools and figures used in my research.

I would also like to thank my other PhD committee members - Doctors Ilya Fabrikant, Brad Shadwick, Kees Uiterwaal, and David Swanson - for reading this dissertation and providing many valuable insights throughout my graduate career. In particular, I'd like to thank Kees Uiterwaal for many hours of stimulating discussion and argument regarding the finer points of optics, angular momentum, and quantum theory.

Contents

List of Figures

Chapter 1

Introduction

1.1   Laguerre-Gaussian modes and optical vortices

Optical vortices, or laser beams that carry orbital angular momentum (OAM), provide a novel means of investigation into laser-matter interactions [1–3]. Consideration of light with nonzero OAM has become increasingly common in many fields including harmonic generation [4–6], particle acceleration [7, 8], and quantum information [9, 10]. The ability to produce vortex beams of light [2, 11–13] or electrons [14–16] with well-defined OAM allows for the study of angular momentum exchange processes when such beams interact with matter. Recently, optical vortex (or "structured light") beams have been used to probe chiral matter [17], to study multipole excitation of atoms as a function of their location with respect to the beam axis [18], to improve vacuum acceleration of electrons [8], and to advance quantum information technologies [11, 19], among numerous other applications.

   In describing such beams mathematically, it is often most convenient to select a set of basis functions which take advantage of the cylindrical symmetry of a laser pulse in the plane perpendicular to the direction of its propagation (Fig. 1.1). The Laguerre-Gaussian (LG) basis represents one such set of functions, and can be used to represent optical
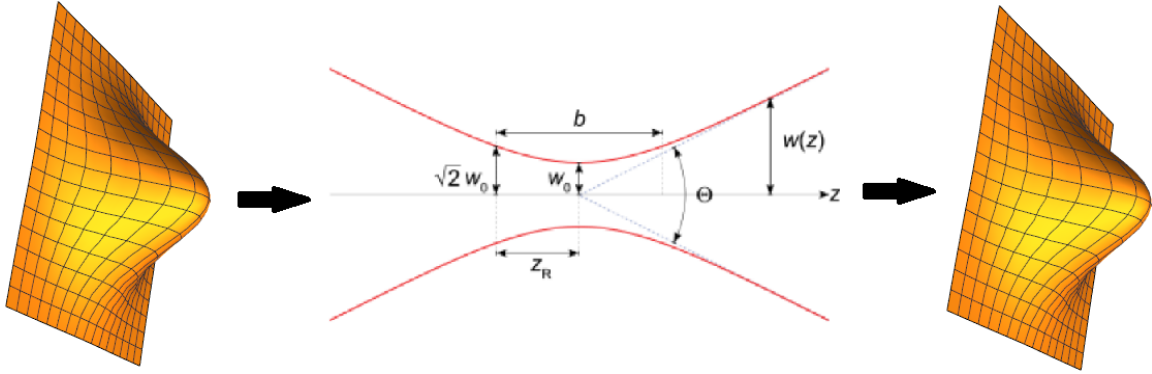
Figure 1.1: A propagating $LG_{0,0}$ (Gaussian) beam focuses then de-focuses in the vicinity of the beam waist. A cross section of the spatial profile of an LG beam near the focal region (center) shows its relevant physical parameters. The beam waist, w_0, is the width of the beam at its tightest focus. The Rayleigh range, Z_R, is the longitudinal distance from the focal plane at which the beam width $w(z)$ grows to $\sqrt{2}\, w_0$. The cylindrical symmetry of the Gaussian pulse is maintained while focusing and de-focusing. (Image modified from Wikipedia)

vortices which carry arbitrarily-many quanta of angular momentum [20].

Laser pulses described in the LG basis are distinguished by two indices, $LG_{n,m}$, where n and m describe the radial and orbital profiles, respectively, of the pulse. The radial mode n represents the number of (non-axial) nodes in the radial intensity profile of the beam. The orbital mode m represents the number of full phase cycles which are experienced in traversing 2π radians about the central axis of a transverse cross section, and indicates the quantized value of orbital angular momentum $m\hbar$ carried by the beam. This mode is also referred to as the winding number or topological charge. Different n and m values are best understood visually, and are shown explicitly in Fig. 1.2.

The OAM associated with an LG beam is an ensemble property manifesting as a global phase structure $\exp(im\phi)$ in the beam's profile, where ϕ is the polar angle (Fig. 1.2D&E). This phase indicates a singularity on axis, where ϕ is undefined, for all nonzero OAM modes. This singularity is the source of the axial nodes in intensity, as seen in Fig. 1.2(A-C). Such modes are often referred to as "donut modes" due to the hole (node) in the center of the circular intensity profile.
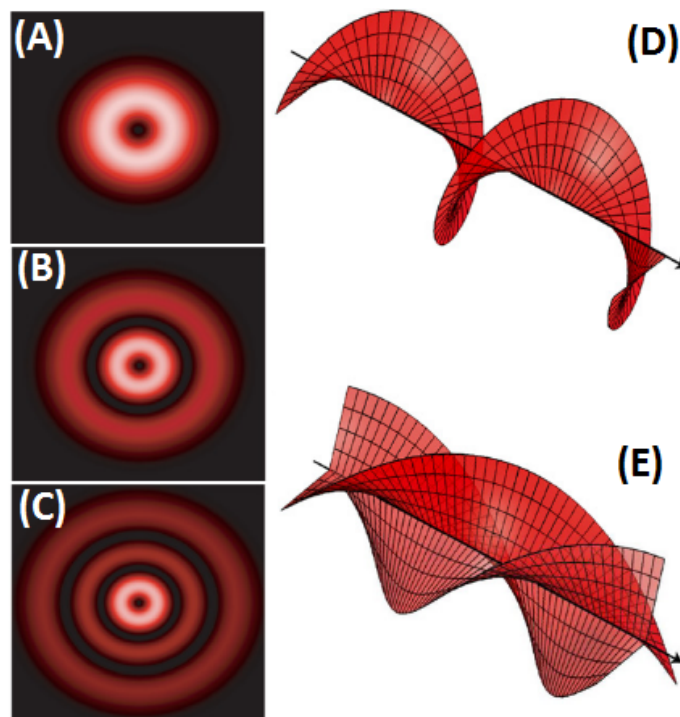
Figure 1.2: Visualization of LG orbital and radial mode numbers. Panels (A),(B),(C) show cross sectional average intensity profiles of beams for $LG_{0,1}$, $LG_{1,1}$, and $LG_{2,1}$ modes, respectively. The dark central spots indicate zero intensity due to an axial phase singularity. Panels (D),(E) show surfaces of constant phase for beams with orbital index $m = 1$ and $m = 3$, respectively. (Images modified from Ref. [2])

One way OAM can be encoded into a beam is by passing a Gaussian source through a spiral phase plate, wherein the thickness of the plate depends on the azimuthal coordinate ϕ [21–24]. Additionally, holograms and forked diffraction gratings provide another means of producing optical vortices (cf. Ref. [25]), but these methods produce resulting beams with significantly lower intensities than that of the source beam. Alternatively, such structured light can also be created in the extreme ultraviolet by means of high-order harmonic generation [5, 26, 27].

1.2 Analytical models

The worldwide effort to develop increasingly powerful lasers will allow the exploration of new physical regimes of intense laser interactions with matter as well as the development of new applications that such intense laser regimes permit [28, 29]. Theoretical modeling of these interactions must begin with accurate descriptions of the driving laser fields, taking into account arbitrary focal spot size, pulse duration, and OAM content, amongst other properties. Traditionally, solving the full Helmholtz problem involves finding six field solutions to the vector Helmholtz equations. Matters are greatly simplified when instead one needs to find only a single solution to the scalar Helmholtz equation (HE),

$$\left(\nabla^2 + k^2\right) U(\mathbf{r}, \omega) = 0. \tag{1.1}$$

The HE is derived through separation of spatial and temporal variables in the wave equation, and the parameter k in Eq. (1.1) represents the wave vector. The one solution to the scalar HE, U, is the beam's phasor, which describes its amplitude distribution.

From a general expression for a phasor, Hertz potentials [30, 31] (alternatively "Hertz vectors" or "polarization potentials") can be used to generate exact expressions for the complex EM fields. The Hertz vectors, defined in Eq. (1.2) for a beam propagating in the $\hat{\mathbf{z}}$-direction with linear polarization in the $\hat{\mathbf{x}}$-direction, are represented in general as the complex phasor with a direction that is chosen based on the beam polarization,

$$\mathbf{\Pi}_e = U(\mathbf{r}, t)\,\hat{\mathbf{x}} \tag{1.2a}$$

$$\mathbf{\Pi}_m = \eta_0\,U(\mathbf{r}, t)\,\hat{\mathbf{y}}, \tag{1.2b}$$

where η_0 is the impedance of free space and $U(\mathbf{r}, t)$ is the Fourier transform of $U(\mathbf{r}, \omega)$.

The Hertz potentials are sometimes referred to as "super potentials" because they

directly generate the usual scalar and vector EM potentials (ϕ and $\mathbf{A}$),

$$\phi = \nabla \cdot \boldsymbol{\Pi}_e \tag{1.3a}$$

$$\mathbf{A} = \frac{1}{c^2}\frac{\partial \boldsymbol{\Pi}_e}{\partial t} + \mu_0 \nabla \times \boldsymbol{\Pi}_m, \tag{1.3b}$$

which in turn generate the EM fields. Consequently, the complex vector fields $\mathbf{E}$ and $\mathbf{B}$ can be obtained directly from the Hertz potentials [30], and therefore from the phasor,

$$\mathbf{E} = \nabla \times \nabla \times \boldsymbol{\Pi}_e - \mu_0 \frac{\partial}{\partial t}\left(\nabla \times \boldsymbol{\Pi}_m\right) \tag{1.4a}$$

$$\mathbf{H} = \nabla \times \nabla \times \boldsymbol{\Pi}_m + \epsilon_0 \frac{\partial}{\partial t}\left(\nabla \times \boldsymbol{\Pi}_e\right). \tag{1.4b}$$

Thus, derivation of an appropriate phasor is the primary task in developing an analytical description of optical fields.

To simplify calculations in the case of loose focusing, for instance, one often adopts the so-called paraxial approximation, which assumes that the beam's amplitude changes more rapidly in the transverse direction than in the direction of propagation ($\hat{z}$). Mathematically, Eq. (1.1) can be expanded with

$$\nabla^2 U = \left(\nabla_\perp^2 + \nabla_z^2\right) U, \tag{1.5}$$

wherein the paraxial approximation can then formally be invoked by claiming $|\nabla_z^2 U| \ll |\nabla_\perp^2 U|$ and dropping the smaller term.

For some applications of optical vortex beams (such as, e.g., vacuum acceleration of charged particles [8]), high field intensities are required to achieve desired results. Experimentally, the highest laser intensities are obtained using tight focusing techniques, in which the laser spot size in the focal region is comparable to the laser field

wavelength. However, such tightly-focused beams cannot be correctly described within the paraxial approximation [32, 33] and thus theoretical simulations of laser-matter interactions under such tight focusing conditions require a detailed description of the laser fields in the focal region that includes nonparaxial effects [33–39]. Multiple nonparaxial analytic representations have been developed to model such tightly focused beams with nonzero OAM (cf. Refs. [32, 40–43]).

The remainder of this dissertation addresses the modeling and application of tightly-focused LG beams which cannot be well-described under the paraxial approximation. Chapter 2 presents one such nonparaxial model, which is an exact solution of the scalar HE. This model, however, contains an error in the original theory which can lead to nonphysical discontinuities in the real electromagnetic (EM) fields. The source of these discontinuities is found, and a corrected theory is provided. These results are published in Ref. [44]. Even with this correction, calculation of the time-domain phasor for arbitrary LG modes remains difficult. Therefore, Chapters 3 and 4 present a novel approach to describing a completely generalized time-domain phasor, and thus EM fields, of nonparaxial LG beams in the perturbative regime. The results of Chapter 3 are published in Ref. [45], while the results of Chapter 4 have been submitted for publication. Finally, Chapter 5 implements this perturbative model to numerically study acceleration of electrons by higher-order LG modes. These results remain unpublished. Some details of our derivations are included in Appendices A and B. Lastly, Fortran and Python codes for calculating the complex phasor from our generalized perturbative model are provided in Appendix C. The Fortran code was used for all electron acceleration results presented in this work.

Chapter 2

Nonphysical Discontinuities in the Source-Sink Model

2.1 Introduction

The *complex point-source* model [46–48] is one tool that has been developed to analytically describe focused beams carrying OAM. This model describes valid solutions of the nonparaxial HE. The complex point-source model assumes that the beam source exists at a complex point whose real value lies along the beam's axis, and that the beam can be represented by an outgoing spherical wave. It was shown by M. Couture and P. A. Belanger [49] that (for an appropriate choice of boundary conditions) the spherical waves represented by this model are equivalent to the paraxial representation of a Gaussian (zero OAM) beam with all perturbative corrections included. The major benefit of this method is that it provides a closed form analytical representation of the beam's phasor, which is the complex function of the beam's spatiotemporal amplitude and phase that satisfies the scalar HE [3, 20]. This is a distinct advantage of the complex point-source model as compared to other models [32, 40, 41], in which the fields are usually defined using either a series or an integral representation. The complex point-source model,

however, still has one major drawback. Namely, the point-source Gaussian phasor solution is known to contain singularities in its square modulus as well as a discontinuity at the beam waist [50].

Solutions of the HE, or any differential equation, must be analytic functions. The discontinuity at the beam waist discussed above implies that the phasor of the point-source model is not an analytic function, since an analytic function must be infinitely differentiable (and hence integrable). The point-source phasor is therefore not a valid solution to the scalar HE, and a model that is free from this problem is required for a physically accurate description of these laser fields.

The *complex source/sink* model [50] was developed to avoid the discontinuity and singularities encountered in the complex point-source model. The complex source/sink model represents the beam as two counter-propagating spherical waves, both centered at the imaginary location used in the complex point-source model. In this new model, the singularities and discontinuity in the square modulus of the Gaussian phasor both vanish.

In this Chapter, it is shown that the discontinuities still arise in phasors generated from the complex source/sink model for all odd OAM modes. The discontinuity in the phasor leads directly to discontinuities in the EM fields. Thus, real fields generated from the complex source/sink phasor are nonphysical for odd OAM values.

This Chapter is organized as follows. In Section 2.2, we demonstrate analytically why the discontinuity appears in the phasor for odd OAM, and why it does not appear for even OAM. It is also shown how the discontinuity can be avoided. In Section 2.3, we present numerical results illustrating the discontinuities in electric field components that result from the discontinuity in the phasor. In Section 2.5, we summarize our results and present our conclusions.

2.2   Discontinuity in the phasor

Using the complex source/sink model, April [43, 51] proposed an analytically exact discontinuity-free representation of the phasor for nonparaxial LG beams of any radial and OAM mode. April's methods have since been adopted in many other works (e.g., [52–59]). As long as one considers only the square modulus of phasor solutions derived from the complex source/sink method, such as April's phasor, the discontinuity and singularities are absent as claimed [43, 60]. This does not mean, however, that the phasors themselves are discontinuity free. As we show in this section, consideration of the real and/or imaginary parts of the source/sink phasor, depending on the choice of initial phase ϕ_0, very clearly reveals a discontinuity at the beam waist for certain parameters. The presence of this axial discontinuity depends on the choice between two representations of the complex radius of curvature of the spherical waves, $\widetilde{R}$ [43, 61].

Most work using April's phasor (e.g., [52–55, 57, 59]) has so far been done with the lowest order LG mode (the "Gaussian mode," which has zero OAM) or by considering the phasor only in the paraxial limit. As we will show, the phasors for these two common cases are not affected by this discontinuity.

Formally, April [43] combined the complex source/sink method with use of a Poisson-like frequency spectrum [40, 62], $f(\omega)$, to analytically represent the generic phasor $U_{p,n}$, describing an $LG_{p,n}$ beam, from which EM fields can be derived using the Hertz potentials [Eq. (1.4)]. For the zero order radial mode ($p = 0$), April's phasor for the nonparaxial LG beam with any OAM index n can be expressed as (see Eqs. (16) & (17) of [43])

$$U_{0,n}(\mathbf{r}, \omega) = \frac{4\cos(n\phi)}{(2n-1)!!} f(\omega) \left(\frac{ka}{2}\right)^{1+n/2} \exp(-ka) P_n^n(\chi) j_n(k\widetilde{R}), \qquad (2.1)$$

where j_n is the spherical Bessel function, a is the confocal parameter of the focused beam, ϕ is the cylindrical angle, and the complex-valued associated Legendre function

$P_n^n(\chi)$ is defined by Eqs. (8.6.6) and (8.6.18) of Ref. [63],

$$P_n^n(\chi) = \left(\chi^2 - 1\right)^{n/2} \frac{d^n}{d\chi^n} \left(\frac{1}{2^n n!} \frac{d^n \left(\chi^2 - 1\right)^n}{d\chi^n} \right), \qquad (2.2)$$

in which the complex argument, χ, is defined by

$$\chi \equiv (z + ia)/\widetilde{R}. \qquad (2.3)$$

There are two choices (cf. Eq. (14) of Ref. [43]) for the complex spherical radius of curvature, $\widetilde{R}$, in Eq. (2.1):

$$\widetilde{R}_1 = \sqrt{\rho^2 + (z + ia)^2} \qquad (2.4\text{a})$$

$$\widetilde{R}_2 = i\sqrt{-\rho^2 - (z + ia)^2}, \qquad (2.4\text{b})$$

where ρ, ϕ, z are the cylindrical coordinates in which $\hat{\mathbf{z}}$ is the direction of propagation, and the principal values of the roots are considered. The Poisson-like frequency spectrum $f(\omega)$ in Eq. (2.1) is defined as (see Eq. (4) of [40] or Eq. (20) of [43])

$$f(\omega) = 2\pi e^{i\phi_0} \left(\frac{s}{\omega_0} \right)^{s+1} \frac{\omega^s \exp(-s\omega/\omega_0)}{\Gamma(s + 1)} \theta(\omega), \qquad (2.5)$$

where s is the spectral parameter [40, 62] (which is related to the bandwidth of the pulse, which in turn is related to its duration), ω_0 is the frequency at which $f(\omega)$ has its maximum, ϕ_0 is the phase of the pulse, and $\theta(\omega)$ is the Heaviside unit step function. In the limit of a narrow spectrum, $s \gg 1$, Eq. (2.5) reduces to a Gaussian spectrum with pulse duration $\tau = \sqrt{2s}/\omega_0$.

It has been stated [43, 61] that neither choice of $\widetilde{R}$ in Eq. (2.4) would cause the phasor to suffer from discontinuities. We will show, however, that only the choice $\widetilde{R}_2$ produces continuous field components across the beam waist for all values of OAM.

Note also that the associated Legendre functions defined in Eq. (2.2) contain a branch cut only for odd index n. The following sections will elucidate the interplay between this branch cut and the choice of $\widetilde{R}$, and show how this determines whether or not the phasors contain discontinuities.

2.2.1   Odd OAM modes

Inspection of Eqs. (2.1)-(2.5) shows that only the last two factors in the phasor may lead to the existence of a discontinuity. We thus focus on these two factors and express Eq. (2.1) as

$$U_{0,n}(\mathbf{r},\omega) = c_n(\phi,\omega)P_n^n(\chi)j_n(k\widetilde{R}), \tag{2.6}$$

where $c_n(\phi,\omega)$ is defined by comparison of Eqs. (2.1) and (2.6). To illustrate how the choice of $\widetilde{R}$ determines whether or not there is a discontinuity in the phasor, we consider the simplest odd OAM mode, $n = 1$. We first use the choice $\widetilde{R}_1$ to demonstrate a discontinuity at the beam waist, $z = 0$.

2.2.1.1   Exact expansion of $U_{0,1}$ in powers of $\widetilde{R}$

Expressing the spherical Bessel function in Eq. (2.6) in terms of sines and cosines [cf. Eqs. (2.18)–(2.20)] and defining the parameter

$$\xi \equiv k\widetilde{R}, \tag{2.7}$$

the $n = 1$ phasor may be expressed as

$$U_{0,1} = c_1 P_1^1(\chi)\left(-\frac{\cos(\xi)}{\xi} + \frac{\sin(\xi)}{\xi^2}\right). \tag{2.8}$$

Replacing the trigonometric functions by their series expansions, we obtain

$$U_{0,1} = c_1 P_1^1(\chi) \left[-\frac{1}{\xi} \sum_{m=0}^{\infty} \frac{(-1)^m \xi^{2m}}{(2m)!} + \frac{1}{\xi^2} \sum_{m=0}^{\infty} \frac{(-1)^m \xi^{2m+1}}{(2m+1)!} \right]. \tag{2.9}$$

Combining the two summations, we obtain:

$$U_{0,1} = c_1 P_1^1(\chi) \frac{1}{\xi} \sum_{m=0}^{\infty} \kappa_m \, \xi^{2m} \tag{2.10a}$$

$$\kappa_m \equiv (-1)^{m+1} \frac{2m}{(2m+1)!} \tag{2.10b}$$

where, from Eq. (2.2),

$$P_1^1(\chi) = \sqrt{\chi^2 - 1}. \tag{2.11}$$

2.2.1.2 $U_{0,1}$ with the choice $\widetilde{R} = \widetilde{R}_1$

Making the choice $\widetilde{R} = \widetilde{R}_1$ [defined in Eq. (2.4a)] in Eqs. (2.3) and (2.7), $U_{0,1}$ in Eq. (2.10a) becomes:

$$U_{0,1} = \sqrt{\frac{-\rho^2}{\rho^2 + (z+ia)^2}} \cdot \frac{1}{\sqrt{\rho^2 + (z+ia)^2}} \, c_1 \sum_{m=0}^{\infty} (\kappa_m k^{2m-1}) \left(\rho^2 + (z+ia)^2 \right)^m. \tag{2.12}$$

We see that the summation in Eq. (2.12) involves integer powers of complex numbers, whereas the prefactors multiplying the summation include two square roots of complex numbers, whose evaluation requires some care. In general, when dealing with products of square roots of complex numbers, it is best to evaluate each square root separately by expressing each complex number in terms of its magnitude and phase before taking its square root. In particular, mistakes can easily be made by not taking into account the branch cuts in the square roots. (For example, $\sqrt{-1} \cdot \sqrt{-1} = i \cdot i = -1$, but $\sqrt{-1 \cdot -1} = \sqrt{1} = 1$ is incorrect if both cases are to consider the same standard branch cut along the negative real axis.) Thus, we have expressed each of the complex arguments

of the two square root prefactors in Eq. (2.12) in polar notation before taking the square roots. The result is:

$$U_{0,1} = c_1 \exp\left(\frac{i}{2}\left(\phi_1 - \phi_2\right)\right) \sum_{m=0}^{\infty} \lambda_m \exp(im\phi_2) \tag{2.13a}$$

$$\phi_1 = \arctan\left(\frac{2az}{-\rho^2 + a^2 - z^2}\right) \tag{2.13b}$$

$$\phi_2 = \arctan\left(\frac{2az}{\rho^2 - a^2 + z^2}\right) \tag{2.13c}$$

$$\lambda_m \equiv \left(\kappa_m k^{2m-1}\right) \rho \left[(\rho^2 + z^2 + a^2)^2 - (2a\rho)^2\right]^{(m-1)/2}. \tag{2.13d}$$

Here, the real numbers λ_m are m-dependent magnitudes, defined in Eq. (2.13d), and ϕ_1 and ϕ_2 are the phases of the complex numbers inside the first and second square root prefactors in Eq. (2.12) (which originate from $P_1^1(\chi)$ and $\widetilde{R}_1$ respectively). The so-called "two-argument" arctan function is defined over $-\pi < \phi \leq \pi$; thus, arctan has a branch cut along the negative real axis. At the beam waist $z = 0$, the imaginary parts of the complex numbers whose phases are given by ϕ_1 and ϕ_2 are zero; thus, the branch cut along the negative real axis of each arctan function in Eqs. (2.13b) and (2.13c) is determined by the region over which the denominators in each of their arguments is negative. At $z = 0$ the denominator of ϕ_1 is negative for $\rho > a$, while that for ϕ_2 is negative for $\rho < a$.

The ϕ_1 and ϕ_2 phase factors multiplying the sum in Eq. (2.13a) always have a phase difference of π across the branch cut due to their overall factor of $1/2$ in the exponential. The key point is that ϕ_1 and ϕ_2 have branch cuts over different regions of the parameter ρ/a. Specifically, $U_{0,1}$ is discontinuous for $\rho > a$ at $z = 0$ owing to the change in sign of $\phi_1/2$ across the branch cut, while for $\rho < a$ it is discontinuous owing to the change in sign of $\phi_2/2$ across the branch cut. Consequently, $U_{0,1}$ is discontinuous across the beam waist at $z = 0$ for all values of ρ/a owing to the discontinuity in the product of phases, $\exp\left(\frac{i}{2}\left(\phi_1 - \phi_2\right)\right)$. These ranges of the ratio ρ/a over which the discontinuities in the

phases $\phi_1/2$, $-\phi_2/2$, and $(\phi_1 - \phi_2)/2$ occur are illustrated in the three panels of Fig. 2.1.

Note that for each term in the sum in Eq. (2.13a), there is a phase factor involving an integer multiple of ϕ_2. However, each of these terms is continuous across the branch cut since each branch contains an integer number m of full periods, resulting in a 2π phase difference across the branch cut. Thus, the terms in the sum do not contribute to any discontinuity.

2.2.1.3 $U_{0,1}$ with the choice $\widetilde{R} = \widetilde{R}_2$

Use of the choice $\widetilde{R} = \widetilde{R}_2$ results instead in the phasor $U_{0,1}$ being continuous, as may be seen using the same arguments as in the previous section. Specifically, we replace $\widetilde{R}_1$ by $\widetilde{R}_2$[defined in Eq. (2.4b)] in Eqs. (2.3) and (2.7) and substitute the results in Eq. (2.10a). Since $\widetilde{R}_1^2 = \widetilde{R}_2^2$, the terms in the summation are continuous across the branch cut. We thus focus on the new square root prefactors (corresponding to those for $\widetilde{R} = \widetilde{R}_1$ in Eq. (2.12)):

$$U_{0,1} \propto \sqrt{\frac{-\rho^2}{\rho^2 + (z + ia)^2}} \cdot \frac{1}{\sqrt{-\rho^2 - (z + ia)^2}}. \tag{2.14}$$

The number inside the first square root factor is the same as in Eq. (2.12); consequently, it has the same phase factor, $\exp(i\phi_1)$. The number inside the square root in the denominator of the second factor in Eq. (2.14) has the phase factor $\exp(i\phi_3)$, where

$$\phi_3 = \arctan\left(\frac{-2az}{-\rho^2 + a^2 - z^2}\right). \tag{2.15}$$

Thus, the phasor has the same form as in Eq. (2.13a), but with a different phase outside the sum, i.e.,

$$U_{0,1} = -ic_1 \exp\left(\frac{i}{2}(\phi_1 - \phi_3)\right) \sum_{m=0}^{\infty} \lambda_m \exp(im\phi_2) \tag{2.16}$$
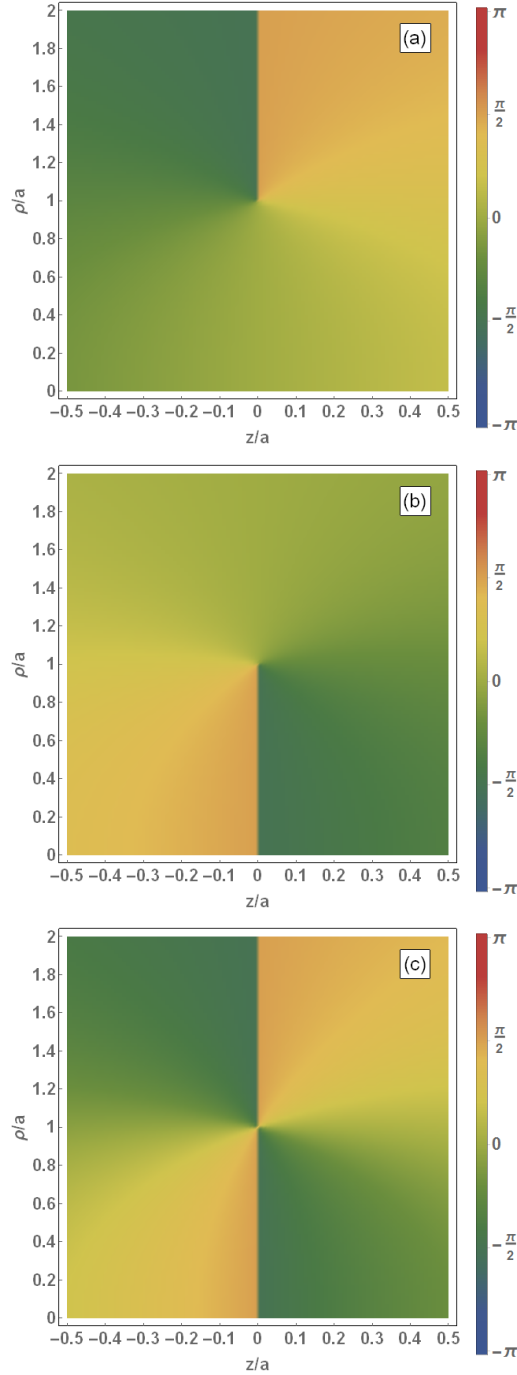
Figure 2.1: The phases (a) $\phi_1/2$, (b) $-\phi_2/2$, and (c) $(\phi_1 - \phi_2)/2$ as functions of ρ/a and z/a, where a is the confocal parameter of the focused laser beam. Values of each phase over the range from $-\pi$ to $+\pi$ are indicated by the vertical color coding strip to the right of each panel. A phase jump of π occurs for $\rho/a > 1$ in (a), for $\rho/a < 1$ in (b), and for all values of ρ/a in (c). See text for discussion.
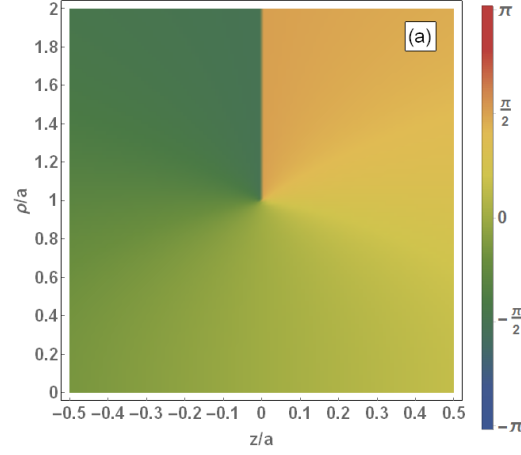
(a)
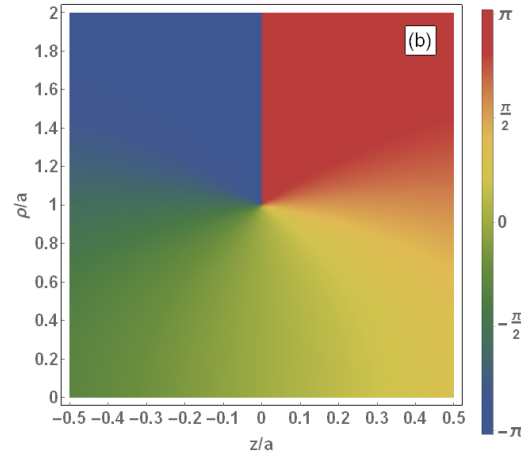
(b)

Figure 2.2: The phases (a) $-\phi_3/2$ and (b) $(\phi_1 - \phi_3)/2$ as functions of ρ/a and z/a, where a is the confocal parameter of the focused laser beam and the behavior of the phase $\phi_1/2$ is shown in Fig. 2.1(a). Values of each phase over the range from $-\pi$ to $+\pi$ are indicated by the vertical color coding strip to the right of each panel. For $\rho/a > 1$ a phase jump of π occurs in (a) and a phase jump of 2π occurs in (b). See text for discussion.

By considering the branch cut in arctan, one can see that both ϕ_1 and ϕ_3 are discontinuous in the same region, namely for $\rho > a$. In both cases, the value changes sign as the $z = 0$ plane is crossed. When these two phase factors are multiplied together as in Eq. (2.16), each one has a phase jump of π (cf. Figs. 2.1(a) and 2.2(a)), so that their product has a phase jump of 2π, as shown in Fig. 2.2(b). Hence, the phasor defined by Eq. (2.16) is continuous across the branch cut.

2.2.1.4 Case of Arbitrary Odd OAM Modes

We may easily see that for any odd OAM index n in Eq. (2.6), the phasor $U_{0,n}$ will exhibit the same behaviors as just shown for the $n = 1$ case. First, the associated Legendre function $P_n^n(\chi)$ in Eq. (2.2) always introduces a square root factor as on the right hand side of Eq. (2.11) for any odd index n, which in turn results in the first square root factor in Eqs. (2.12) and (2.14) regardless of whether one chooses respectively $\widetilde{R} = \widetilde{R}_1$ or $\widetilde{R} = \widetilde{R}_2$. Second, the spherical Bessel function factor j_n in Eq. (2.6) will always introduce the second square root factor in Eqs. (2.12) and (2.14), depending respectively upon whether one chooses $\widetilde{R} = \widetilde{R}_1$ or $\widetilde{R} = \widetilde{R}_2$. One may see this by examining the expression for the spherical Bessel function given in Eq. (2.18). Specifically, for odd n the square root factor comes from the factor $1/\widetilde{R}$ outside the square brackets in Eq. (2.18); for odd n the two summations inside the square brackets in Eq. (2.18) involve only even powers of $\widetilde{R}$ and hence do not contribute any square root factors. Thus, the discontinuity in the phasor $U_{0,n}$ for a particular choice of $\widetilde{R}$ has the same behavior for any odd OAM n.

2.2.2 Even OAM modes

For even OAM modes n, the general expression for the phasor in Eq. (2.1) has the same form as in Eq. (2.6). As has already been noted above, the associated Legendre function defined in Eq. (2.2) does not have a branch cut for even index n. We thus focus on the spherical Bessel function j_n in Eq. (2.6), using the expression for j_n in Eq. (2.18). From Eqs. (2.19) and (2.20) we see that for any OAM mode n the functions P and Q involve respectively even and odd powers of $\widetilde{R}$. For even n, the sine and cosine functions in Eq. (2.18) may be expanded respectively in terms of odd and even powers of $\widetilde{R}$. Thus the two terms inside the square bracket in Eq. (2.18) each involve odd powers of $\widetilde{R}$. Owing to the $1/\widetilde{R}$ factor multiplying the square bracket in Eq. (2.18), the spherical Bessel function j_n for even n may thus be expressed as an expansion in even powers of $\widetilde{R}$. Consequently,
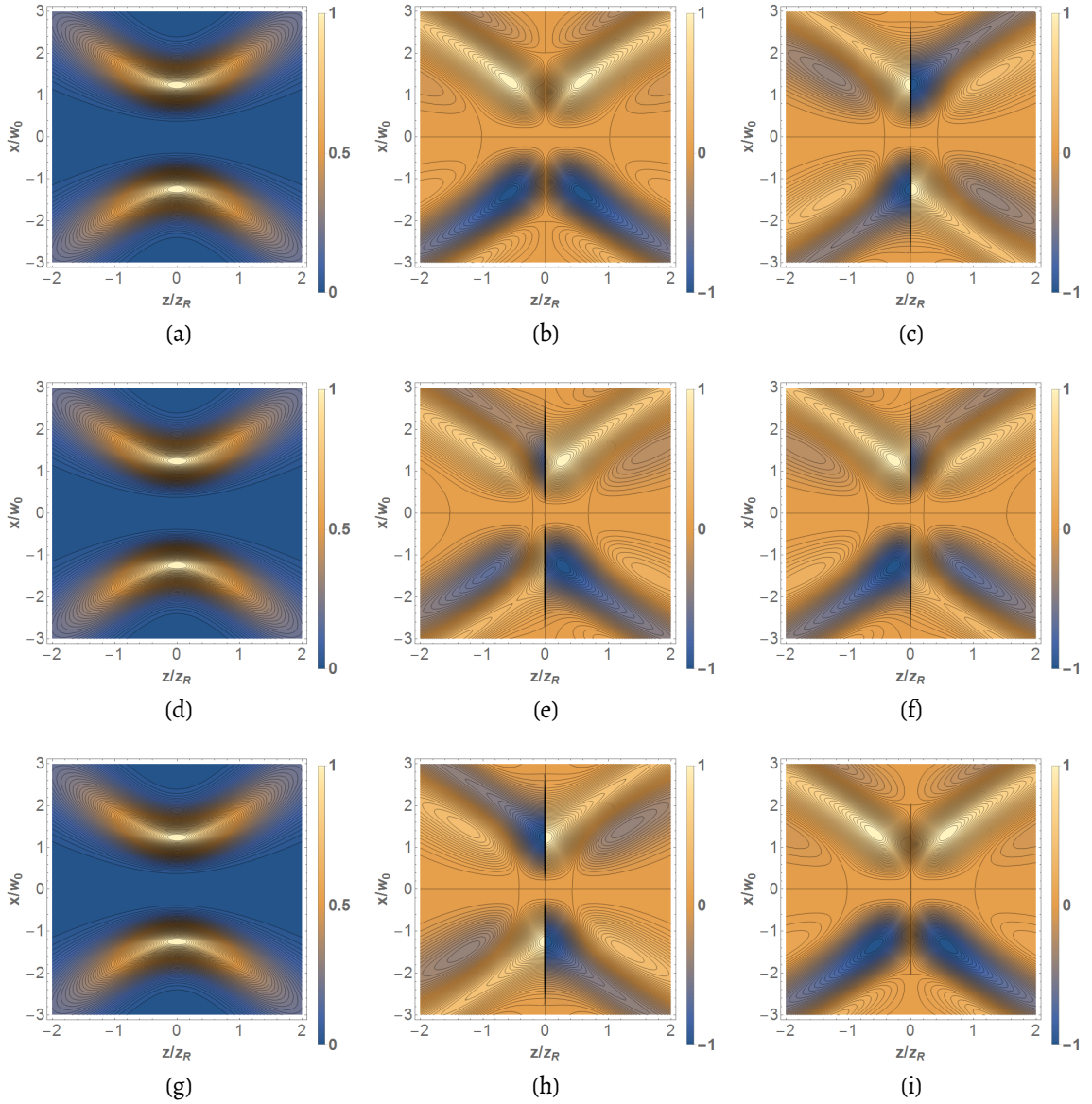
Figure 2.3: The square modulus [(a),(d),(g)], real part [(b),(e),(h)], and imaginary part [(c),(f),(i)] of the phasor $U_{0,n}(\mathbf{r}, t)$ in Eq. (2.17) for n=3 for phases $\phi_0 = 0$ [(a)-(c)], $\phi_0 = \pi/4$ [(d),(e),(f)], and $\phi_0 = \pi/2$ [(g),(h),(i)]. Here, x, y, z are the Cartesian coordinates. The real and imaginary parts of the phasor are normalized to have a maximum amplitude of unity, and were calculated using the choice $\widetilde{R} = \widetilde{R}_1$ at $y = 0$ and $t = z/c$. The linearly polarized beam is assumed to have a spectral parameter $s = 712$, beam waist $w_0 = 2\ \mu m$, wavelength $\lambda = 800\ nm$, and Rayleigh length $z_R \approx 15.7 \mu m$. See text for discussion.

since $\widetilde{R}_1^2 = \widetilde{R}_2^2$ the spherical Bessel function j_n for even n is independent of the choice of the expression used for $\widetilde{R}$. Also, since there are no odd powers of $\widetilde{R}$ in the expression for j_n for even n, no branch cuts are introduced. Thus, the phasor $U_{0,n}$ for even n has no discontinuities.

2.3 Discontinuity in the real fields

We can express the phasor of Eq. (2.1) in the time domain via a Fourier transformation,

$$U_{0,n}(\mathbf{r}, t) = \frac{1}{2\pi} \int U_{0,n}(\mathbf{r}, \omega) \exp(i\omega t) d\omega, \tag{2.17}$$

the result of which is presented for arbitrary n in Eq. (2.22). Recall that the frequency spectrum $f(\omega)$ of the pulse, defined in Eq. (2.5), introduces an overall phase factor $\exp(i\phi_0)$ in both the frequency-dependent and time-dependent phasors in Eqs. (2.1) and (2.17) respectively. Therefore, changes in the initial phase ϕ_0 can affect the occurrence of discontinuities in the real and imaginary components of the phasor.

Figure 2.3 shows explicitly the discontinuities in the time domain phasor for $n = 3$ when using the choice $\widetilde{R} = \widetilde{R}_1$ for three values of the phase ϕ_0. These plots were generated for a linearly polarized beam with spectral parameter $s = 712$, beam waist $w_0 = 2\,\mu m$, wavelength $\lambda = 800\,nm$, and Rayleigh length $z_R = kw_0^2/2$. As expected, no discontinuity is visible in the square modulus of the time domain phasor for any ϕ_0. However, the discontinuity at $z = 0$ is clearly visible in the real and/or imaginary parts of the phasor, depending upon the value of ϕ_0 [cf. panels (c), (e), (f), and (h) of Fig. 2.3].

In Figure 2.4, we plot the longitudinal fields E_z [obtained using Eq. (1.4)] for the odd OAM phasors $U_{0,n}(\mathbf{r}, t)$ for $n = 1$ and $n = 3$ using the choice $\widetilde{R} = \widetilde{R}_1$ and an overall phase $\phi_0 = \pi$. This choice of the phase ϕ_0 yields a discontinuity in the imaginary parts of each of the phasors, which in turn results in discontinuous fields E_z. The corresponding transverse fields (not shown) are continuous across the beam waist at $z = 0$. In general,

for linearly polarized fields, our calculations show that discontinuities in the real part of the time domain phasor lead to discontinuities in the transverse components of **E** and **B** while discontinuities in the imaginary part of the time domain phasor lead to discontinuities in the longitudinal components of the fields. When both the real and imaginary parts of the phasor have discontinuities, the problem appears in all real field components.

(a)

(b)
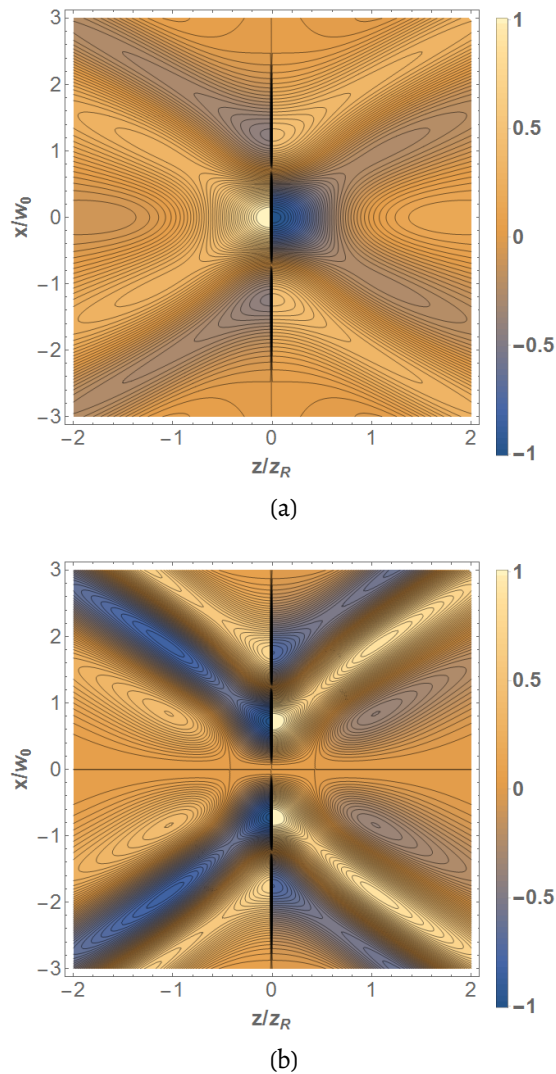
Figure 2.4: Discontinuities in the longitudinal fields E_z [obtained using Eq. (1.4)] across the beam waist $z = 0$ for the odd OAM phasors $U_{0,n}$ for (a) $n = 1$, and (b) $n = 3$. These fields were obtained using the choice $\widetilde{R} = \widetilde{R}_1$ for a phase $\phi_0 = \pi$, $y = 0$, and $t = z/c$. The amplitudes of the fields are normalized to unity. See text for discussion.

As for the case of linear polarization, other beam polarizations will also suffer discontinuous real fields for phasors calculated using the choice $\widetilde{R} = \widetilde{R}_1$. These discontinuities originate in the phasor, which is polarization-independent. The polarization only enters when computing the fields using the Hertz potentials, as Eq. (1.2) demonstrates for the case of linear polarization. The discontinuities may occur in different field components, depending on the field polarization, but they will be present in the real fields nonetheless.

Although our focus in this chapter is on solutions to the nonparaxial HE, a brief mention of the paraxial case is warranted. In the paraxial limit of the phasor (cf. Eq. (5) of Ref. [43]), the terms $P_n^n(\chi)$ and $\widetilde{R}$ do not enter. In fact, to lowest radial order the associated Laguerre polynomials in the paraxial phasor are unity. Thus the real and imaginary parts of the paraxial phasor, by direct inspection, are simple oscillatory functions of z. In this limit, therefore, the problem of discontinuities in the fields does not arise.

2.4 Explicit expression for the phasor $U_{0,n}(\mathbf{r}, t)$

In this Section we present the result of carrying out the Fourier transform of the phasor $U_{0,n}(\mathbf{r}, \omega)$ in Eq. (2.1), which is obtained from Eqs. (16) & (17) of Ref. [43] for the phasor $\tilde{U}_{0,n}^{\sigma}(\mathbf{r}, \omega)$ upon setting $\sigma = e$ and $p = 0$ (and dropping the explicit notation of the parity $\sigma = e$ in our calculations). In order to carry out the Fourier transform in Eq. (2.17), one must expand the spherical Bessel function in Eq. (2.1) using Eq. (10.1.8) of Ref. [63]:

$$j_n(k\widetilde{R}) = \frac{1}{k\widetilde{R}} \left[P\left(n + \frac{1}{2}, k\widetilde{R}\right) \sin\left(k\widetilde{R} - \frac{n\pi}{2}\right) + Q\left(n + \frac{1}{2}, k\widetilde{R}\right) \cos\left(k\widetilde{R} - \frac{n\pi}{2}\right) \right]$$

(2.18)

where

$$P\left(n + \frac{1}{2}, k\widetilde{R}\right) = \sum_{m=0}^{\lfloor n/2 \rfloor} (-1)^m (2k\widetilde{R})^{(-2m)} \frac{(n+2m)!}{(2m)!\,\Gamma(n-2m+1)} \tag{2.19}$$

and

$$Q\left(n + \frac{1}{2}, k\widetilde{R}\right) = \sum_{m=0}^{\lfloor (n-1)/2 \rfloor} (-1)^m (2k\widetilde{R})^{(-2m-1)} \frac{(n+2m+1)!}{(2m+1)!\,\Gamma(n-2m)} \tag{2.20}$$

2.4.1 Result for $U_{0,n}(\mathbf{r}, t)$

Expanding the trigonometric functions in Eq. (2.18) in terms of exponentials and replacing k everywhere by $k = \omega/c$, one may carry out the Fourier transform in Eq. (2.17) by making repeated use of the integral representation of the gamma function (cf. Eq. (6.1.1) of [63]), i.e.,

$$\Gamma(\gamma + 1) = \eta^{\gamma+1} \int_0^\infty \mathrm{d}\omega\, \omega^\gamma \exp(-\eta\omega) \quad , Re\,\eta > 0 \tag{2.21}$$

The result for $U_{0,n}(\mathbf{r}, t)$ is:

$$
\begin{aligned}
U_{0,n}(\mathbf{r}, t) = {} & C_n \cos(n\phi) P_n^n(\chi) \\
& \times \left\{ \sum_{m=0}^{\lfloor n/2 \rfloor} A(n,m) \left(\frac{c}{\widetilde{R}}\right)^{2m+1} \left[(T_-)^{-(s+n/2-2m+1)} - (-1)^n (T_+)^{-(s+n/2-2m+1)} \right] \right. \\
& \left. + \sum_{m=0}^{\lfloor (n-1)/2 \rfloor} D(n,m) \left(\frac{c}{\widetilde{R}}\right)^{2m+2} \left[(T_-)^{-(s+n/2-2m)} + (-1)^n (T_+)^{-(s+n/2-2m)} \right] \right\}
\end{aligned}
\tag{2.22}
$$

In Eq. (2.22) we have defined

$$A(n,m) \equiv \frac{i(-1)^{m+1}(n+2m)!}{(2m)!\,\Gamma(n-2m+1)} \frac{\Gamma(s+n/2-2m+1)}{2^{(2m+1)}\,\Gamma(s+1)} \left(\frac{s}{\omega_0}\right)^{(2m-n/2)} \tag{2.23}$$

$$D(n,m) \equiv \frac{(-1)^m (n + 2m + 1)!}{(2m + 1)!\, \Gamma(n - 2m)} \frac{\Gamma(s + n/2 - 2m)}{2^{(2m+2)}\, \Gamma(s + 1)} \left(\frac{s}{\omega_0}\right)^{(2m+1-n/2)} \tag{2.24}$$

where s and ω_0 are defined in the text below Eq. (2.5),

$$C_n \equiv \exp[i\,(\phi_0 - n\pi/2)] \left(\frac{a}{c}\right)^{(1+n/2)} \frac{2^{(1-n/2)}}{(2n - 1)!!} \tag{2.25}$$

and

$$T_\pm \equiv 1 - \frac{i\omega_0 t}{s} + \frac{a\omega_0}{cs} \pm \frac{i\omega_0 \widetilde{R}}{cs} \tag{2.26}$$

2.4.2   Result for $U_{0,1}(\mathbf{r}, t)$

Setting $n = 1$ in Eq. (2.22), we have

$$C_1 = \exp[i\,(\phi_0 - \pi/2)]\sqrt{2}\left(\frac{a}{c}\right)^{3/2} \tag{2.27}$$

$$A(1, 0) = -i\,\frac{\Gamma(s + 3/2)}{2\,\Gamma(s + 1)} \left(\frac{s}{\omega_0}\right)^{-1/2} \tag{2.28}$$

$$D(1, 0) = \frac{\Gamma(s + 1/2)}{2\,\Gamma(s + 1)} \left(\frac{s}{\omega_0}\right)^{1/2} \tag{2.29}$$

Hence,

$$\begin{aligned}
U_{0,1}(\mathbf{r}, t) = C_1 \cos(\phi) P_1^1(\chi) \Bigg\{ &A(1, 0) \left(\frac{c}{\widetilde{R}}\right) \left[(T_-)^{-(s+3/2)} + (T_+)^{-(s+3/2)}\right] \\
&+ D(1, 0) \left(\frac{c}{\widetilde{R}}\right)^2 \left[(T_-)^{-(s+1/2)} - (T_+)^{-(s+1/2)}\right] \Bigg\}
\end{aligned} \tag{2.30}$$

2.5   Summary

In this Chapter, we have shown (by examining the nonparaxial source/sink phasor) that for all odd OAM modes discontinuities arise across the entire beam waist when the choice $\widetilde{R} = \widetilde{R}_1$ is made for the complex spherical radius. Whether these discontinuities lie in the real or imaginary parts of the phasor depends upon the overall phase ϕ_0 of the laser pulse. In turn, these phasor discontinuities result in nonphysical real electromagnetic field components calculated from the Hertz potentials.

As we have shown, these problems do not exist for even OAM modes. Further, in the paraxial limit, the terms that cause discontinuous behavior are not present in the phasor expression. Thus, real components of paraxial fields are free from discontinuities in the phasor that cause problems in the nonparaxial case.

In essence, these discontinuities arise due to different branch cut selections for each choice of $\widetilde{R}$. The branch cut in the two-argument arctangent is placed along the negative real axis, as is the standard branch cut of the square root used in $\widetilde{R}_2$. The phasor is discontinuous across each of these branches individually but, as we have shown, the discontinuity suffered across both simultaneously is a 2π phase. This results in a continuous description. Choice $\widetilde{R}_1$, on the other hand, does not subscribe to the usual branch cut location. By placing the branch cut for $\widetilde{R}_1$ on, for instance, the positive imaginary axis, the discontinuity suffered when crossing to an adjacent branch of the arctangent is not canceled, and thus nonphysical discontinuities are manifest in the real fields.

Whether considering the fields of vortex beams in vacuum, or interacting with plasmas or other media, proper physical theoretical models are necessary. As this work has shown, discontinuities in the nonparaxial source/sink phasor can be avoided completely by making the choice $\widetilde{R} = \widetilde{R}_2$ for the complex spherical radius. Such a choice avoids discontinuities in the complex phasor for all OAM modes, however, as shown in Sec. 2.4, calculation of higher-order LG modes in the time domain from the source-sink

remains a difficult problem. The next two Chapters present a novel alternative method for deriving (Ch. 3) and generalizing (Ch. 4) such a time-domain description.

Chapter 3

A Perturbative Description of Ultrashort Tightly-Focused eLG Beams

3.1   Introduction

Perturbative solutions for the EM fields beyond the lowest-order paraxial approximation were considered as early as 1975, in which the first few orders of nonparaxial corrections were found [33, 64, 65]. Critically, the first order correction introduces a longitudinal electric field that is absent in the paraxial approximation. Many higher order corrections to the electromagnetic (EM) fields have since been found [34, 38].

Perturbative solutions of the scalar HE provide an alternative approach for treating nonparaxial effects. Solutions for the HE phasor have been obtained primarily by two different methods. One method involves solving for the exact phasor in integral or differential form. This phasor is then expanded perturbatively [65–67]. Alternatively, the HE can be solved one perturbative order at a time, and an exact phasor can be built from the sum of these solutions [49, 64, 68, 69]. With either of these two methods, the HE can be solved under different sets of boundary conditions [70]. Common choices for boundary conditions include: (i) a purely paraxial beam in the focal plane [65, 68, 69]

(where the exact solution is valid in the half space after the focus only, while the perturbative solution is valid in all space), (ii) an oscillatory far-field beam [34, 64], or (iii) an outgoing spherical wave in the far-field [49, 66, 67]. Couture and Belanger [49] showed that the latter, with infinitely many orders of correction, was equivalent to modeling the Gaussian beam with a so-called complex *source-point*.

The complex source-point model warrants additional discussion. It describes the beam as an outgoing spherical wave originating from an imaginary point on the optical axis. The phasor described by this model has a circular singularity in the focal plane since the imaginary location of the point source is related to a circle in real space [71–73]. A boundary condition of far-field counter-propagating spherical waves was implemented to remove the singularity in the complex source-point model [51, 60, 72, 74]. This is known as the complex *source-sink* model, with the source and sink at the same imaginary location along the optical axis. While the singularity is removed in this model, the energy density diverges logarithmically as the transverse coordinate grows large [75]. It has been stated, however, that this energy divergence is irrelevant in practice since neither experiments nor simulations look to sufficiently large transverse distance for it to matter [76, 77].

As our aim in this chapter is to describe tightly-focused optical vortex beams carrying orbital angular momentum, we utilize henceforth LG models of such optical beams. In the remainder of this dissertation, LG beams are classified by two indices n and m as $LG_{n,m}$, with n and m representing the radial and azimuthal profiles, respectively. These are referred to as the LG "modes," of which the lowest order is a Gaussian beam and higher orders can describe vortex beams. In particular, we utilize the so-called elegant LG (eLG) model, wherein the arguments of certain special functions are complex variables. Note that there is a physical difference between LG and eLG models, as discussed by Saghafi and Sheppard [78]. Bandres and Gutiérrez-Vega (BGV) have provided exact integral and differential solutions for monochromatic eLG beams of any LG mode (see Eqs. (16) & (21) of Ref. [67]). These solutions, based on the complex

source-point model, contain the singularity discussed above. In Ref. [67], BGV presented an equally general perturbative solution which does not contain the singularity, since a truncated perturbative model does not exactly satisfy the source-point boundary condition (see Eq. (24) of Ref. [67]).

Nearly all of the analytical models discussed thus far entail a significant limitation: they assume a monochromatic beam. Many modern experiments, particularly those studying high intensity laser-matter interactions, involve optical pulses, shaped pulses, chirped pulses, etc., all of which require a polychromatic description. While long pulses can be well approximated as the product of a temporal Gaussian envelope and a monochromatic field, this description becomes inadequate for ultrashort pulses [79]. Others have employed polychromatic descriptions, but these often assume that k_z is frequency-independent or involve non-LG models (see, e.g., Refs. [80–82]). April [43] generalized his source-sink model [51] for monochromatic eLG fields to allow for polychromatic descriptions by introducing a Poisson-like frequency spectrum [40, 62]. Application of the Hertz potentials [83, 84] then allowed the computation of a complete set of EM fields for an arbitrarily short pulse duration and any LG mode. These fields are free of all singularities [60], and can be made free of all discontinuities (Chap. 2), which are present in the complex source-point models. While Ref. [43] presents a complete model for describing eLG pulses in the frequency domain, the Fourier transform required to achieve a time-domain phasor, and therefore the EM fields, is nontrivial. To our knowledge, this integral has only been carried out for the lowest radial order $n = 0$, as shown in Sec. 2.4. Owing to a sum over radial orders in the frequency-domain phasor of Ref. [43], the Fourier transform for higher radial modes becomes increasingly complicated to calculate.

In this chapter we present an analytical method for calculating the time-domain phasor, and EM fields, of a tightly-focused, arbitrarily-short pulse for any LG mode. Our method generalizes the perturbative approach of BGV [67] by including a Poisson-like

frequency spectrum and calculating the EM fields from the time-domain phasor. We show that our fields agree with those generated from the model of Refs. [43, 44] for the $n = 0$ case, and that fields for higher order LG modes can easily be produced. The primary advantage of this method over that proposed in Ref. [43] is the ability to obtain an explicit expression for the time-domain phasor, thus enabling one to obtain the EM fields by a straightforward prescription.

This chapter is organized as follows. In Section 3.2 we derive the zeroth and first order terms in the perturbative time-domain phasor. In Section 3.3 this derivation is extended to include the second-order correction, outlining a general method for the calculation of higher-order corrections. In Section 3.4 we derive general expressions for the EM fields derived from this time-domain phasor, which are valid for any LG mode and for any order of perturbative correction to the phasor. In Section 3.5 we present a test of the convergence of our perturbative results and examine the necessity of the temporal model we employ. In Section 3.6 we determine the spatial radius of convergence for this perturbative model. Lastly, in Section 3.7 we summarize our results.

3.2 The time-domain phasor to first perturbative order

The derivation of our phasor (the spatiotemporal solution to the scalar HE [85]) begins with the frequency-domain perturbative phasor of BGV (Eq.(24) of Ref. [67]) in cylindrical polar coordinates,

$$
\begin{aligned}
U_{BGV}\left(\mathbf{r}, \omega\right) &= (-1)^{n+m} 2^{2n+m} \exp(ikz + im\phi) \\
&\times h^{2n+m+2} v^{m/2} \exp(-v) \sum_{j=0}^{N} \left(\frac{h^2}{k^2 \mathrm{w}_0^2}\right)^j f_{n,m}^{(2j)}(v) \\
&\equiv U_{0,BGV} + \frac{\epsilon^2}{\beta} U_{2,BGV} + \frac{\epsilon^4}{\beta^2} U_{4,BGV} + \dots \quad ,
\end{aligned}
$$

(3.1)

where $\epsilon \equiv 1/(k\mathrm{w}_0)$ is a small dimensionless parameter, w_0 is the beam waist,

$z_R = k\mathrm{w}_0^2/2$ is the Rayleigh length, $h = (1 + iz/z_R)^{-1/2}$, $\beta = 1/h^2$, $v = h^2\rho^2/\mathrm{w}_0^2$, and N is the term at which the infinite series is truncated. The factors $f_{n,m}^{(2j)}(v)$ can be obtained from Eqs. (25) of Ref. [67] (as discussed in detail in Appendix A). These factors are each linear combinations of associated Laguerre polynomials $L_n^m(v)$, and can be found to any order using the results in Ref. [67].

If we were to evaluate the perturbative expansion of the phasor in Eq. (3.1) to infinite order (i.e., $N \to \infty$), this would be equivalent to describing wave emission from a complex point source (cf. Ref. [49]). The singularity that naturally arises from this point source, however, is avoided by our truncation of the perturbative expansion at some finite order N. This truncation is equivalent to approximating the source-point spherical wave, an effect of which is that we have a singularity-free model. As such, the incoming spherical waves employed in other works are not required to cancel a source-point singularity in our model.

Keeping terms up to order ϵ^2, the sum in the phasor of Eq. (3.1) reduces to

$$\sum_{j=0}^{1} \left(\frac{h}{k\mathrm{w}_0}\right)^{2j} f_{n,m}^{(2j)}(v) = n!L_n^m(v) + \frac{\epsilon^2}{\beta}\left[2(n+1)!L_{n+1}^m(v) - (n+2)!L_{n+2}^m(v)\right]. \quad (3.2)$$

In Eq. (3.2), the associated Laguerre polynomials $L_n^m(v)$ can be expressed as finite sums [86],

$$L_n^m(v) \equiv \sum_{j=0}^{n} G_{n,m,j}\, v^j, \quad (3.3)$$

in which

$$G_{n,m,j} \equiv \frac{(-1)^j(n+m)!}{(n-j)!(m+j)!j!}. \quad (3.4)$$

Since the BGV phasor was derived for the case of a monochromatic field, in order to

describe a temporally finite pulse it must be generalized. We accomplish this by multiplying the BGV phasor by the Poisson-like frequency spectrum $f(\omega)$ presented in Eq. (2.5). Our polychromatic frequency-domain phasor is then defined as,

$$U(\mathbf{r}, \omega) \equiv U_{BGV} f(\omega). \tag{3.5}$$

In order to Fourier transform the phasor in Eq. (3.5) to the time domain, we adopt the condition of isodiffraction, i.e., we assume that every frequency component has the same wavefront radius of curvature. For this choice of complex source-point location, the isodiffraction condition ensures that z_R is constant for all frequency components, whereas the beam waist, $\mathrm{w}_0 = \sqrt{2z_R/k}$, depends on ω through the vacuum dispersion relation $k = \omega/c$, where c is the speed of light [40, 62, 87].

Owing to the introduction of a Poisson-like frequency spectrum to the monochromatic phasor of BGV, implementation of the smallness parameter must be modified slightly. Since ϵ now varies with the frequency, we can use its definition to factor out its frequency dependence,

$$\epsilon^2 = \frac{c}{2z_R\omega} = \frac{c}{2z_R\omega_0}\frac{\omega_0}{\omega} \equiv \epsilon_c^2 \frac{\omega_0}{\omega}, \tag{3.6}$$

where ϵ_c is a frequency-independent (constant) small parameter in terms of the central pulse frequency, ω_0.

With all frequency dependencies accounted for, one can now Fourier transform $U(\mathbf{r}, \omega)$ into the time domain via the unitary transformation

$$U(\mathbf{r}, t) = \frac{1}{\sqrt{2\pi}} \int U(\mathbf{r}, \omega) \exp(-i\omega t) d\omega. \tag{3.7}$$

Using the integral representation of the gamma function [Eq. (2.21)] we obtain the time-domain phasor to $O(\epsilon_c^2)$,

$$U(\mathbf{r}, t) = \Lambda_{n,m} \left[\sum_{j=0}^{n} c_{0,0} \xi^j T^{-(\gamma+1)} + \frac{\epsilon_c^2}{\beta} \left(\sum_{j=0}^{n+1} c_{1,1} \xi^j T^{-\gamma} - \sum_{j=0}^{n+2} c_{1,2} \xi^j T^{-\gamma} \right) \right]. \qquad (3.8)$$

The new variables in Eq. (3.8) are defined as

$$\xi \equiv \frac{\rho^2}{2c\beta z_R} \qquad (3.9a)$$

$$T \equiv 1 + \frac{\omega_0}{s} \left(-\frac{iz}{c} + \xi + it \right) \qquad (3.9b)$$

$$\Lambda_{n,m} \equiv (-1)^{n+m} 2^{2n+m} \sqrt{2\pi} n! \exp(i\phi_0) \xi^{m/2} \beta^{-(n+m/2+1)} \exp(im\phi), \qquad (3.9c)$$

and the constants are defined as

$$c_{0,0} \equiv G_{n,m,j} \left(\frac{\omega_0}{s} \right)^{\gamma-s} \frac{\Gamma(\gamma+1)}{\Gamma(s+1)} \qquad (3.10a)$$

$$c_{1,1} \equiv 2(n+1) G_{(n+1),m,j} \left(\frac{\omega_0}{s} \right)^{\gamma-s-1} \frac{\omega_0 \Gamma(\gamma)}{\Gamma(s+1)} \qquad (3.10b)$$

$$c_{1,2} \equiv \omega_0 (n+1)(n+2) G_{(n+2),m,j} \left(\frac{\omega_0}{s} \right)^{\gamma-s-1} \frac{\Gamma(\gamma)}{\Gamma(s+1)} \qquad (3.10c)$$

$$\gamma \equiv m/2 + s + j. \qquad (3.10d)$$

Further details of this derivation can be found in the next section, where the $O(\epsilon_c^4)$ correction is calculated explicitly.

3.3 The time-domain phasor to order ϵ_c^4

In this Section we derive the $O(\epsilon_c^4)$ correction to the time-domain phasor, starting with the frequency-domain phasor in Eq. (3.1). Considering only the term of order ϵ^4 in

Eq. (3.1), we make the replacements $w_0 \rightarrow \sqrt{2z_R/k}$ and $k \rightarrow \omega/c$ and invoke the condition of isodiffraction, which requires that z_R is constant. We obtain

$$
\frac{\epsilon^4}{\beta^2} U_{4,BGV} = (-1)^{n+m} 2^{2n+m} \exp(i\omega z/c + im\phi) h^{2n+m+2} v^{m/2} \exp(-v) \left[\left(\frac{c}{2\omega\beta z_R} \right)^2 \right.
$$
$$
\left. \times \left\{ 6(n+2)! L_{n+2}^m(v) - 4(n+3)! L_{n+3}^m(v) + \frac{1}{2}(n+4)! L_{n+4}^m(v) \right\} \right].
$$

$$(3.11)$$

Multiplying this result by the Poisson-like frequency spectrum in Eq. (2.5), expressing the associated Laguerre polynomials as sums [see Eqs. (3.3) and (3.4)], and extracting powers of ω within the sums, we obtain

$$
U_4(\omega) = \frac{\Lambda_{n,m}}{\Gamma(s+1)} \exp\left\{ -\omega \left(-\frac{iz}{c} + \xi + \frac{s}{\omega_0} \right) \right\} \left(\frac{s}{\omega_0} \right)^{s+1} \frac{\theta(\omega)\sqrt{2\pi}\epsilon_c^4}{\beta^2}
$$
$$
\times \left[\sum_{j=0}^{n+2} \widetilde{c_{2,2}}\, \xi^j \omega^{\gamma-2} - \sum_{j=0}^{n+3} \widetilde{c_{2,3}}\, \xi^j \omega^{\gamma-2} + \sum_{j=0}^{n+4} \widetilde{c_{2,4}}\, \xi^j \omega^{\gamma-2} \right],
$$

$$(3.12)$$

where some variables defined in Eq. (3.9) have been used, and new constants are defined as follows:

$$
\widetilde{c_{2,2}} \equiv 6\omega_0^2 (n+2)(n+1) G_{(n+2),m,j} \tag{3.13a}
$$

$$
\widetilde{c_{2,3}} \equiv 4\omega_0^2 (n+3)(n+2)(n+1) G_{(n+3),m,j} \tag{3.13b}
$$

$$
\widetilde{c_{2,4}} \equiv \frac{\omega_0^2}{2}(n+4)(n+3)(n+2)(n+1) G_{(n+4),m,j}. \tag{3.13c}
$$

We now Fourier transform $U_4(\omega)$ to the time domain as in Eq. (3.7) to obtain $U_4(t)$,

$$U_4(t) = \frac{\Lambda_{n,m}}{\Gamma(s+1)} \left(\frac{s}{\omega_0}\right)^{s+1} \frac{\epsilon_c^4}{\beta^2} \int_0^\infty \exp(-\omega\eta)$$
$$\times \left[\sum_{j=0}^{n+2} \widetilde{c_{2,2}}\, \xi^j \omega^{\gamma-2} - \sum_{j=0}^{n+3} \widetilde{c_{2,3}}\, \xi^j \omega^{\gamma-2} + \sum_{j=0}^{n+4} \widetilde{c_{2,4}}\, \xi^j \omega^{\gamma-2}\right] d\omega, \tag{3.14}$$

where $\eta = -iz/c + \xi + s/\omega_0 + it$. Using the integral representation of the gamma function in Eq. (2.21), we obtain

$$U_4 = \Lambda_{n,m} \left(\frac{s}{\omega_0}\right)^{s+1} \frac{\epsilon_c^4}{\beta^2} \left[\sum_{j=0}^{n+2} \overline{c_{2,2}}\, \xi^j \eta^{-(\gamma-1)} - \sum_{j=0}^{n+3} \overline{c_{2,3}}\, \xi^j \eta^{-(\gamma-1)} + \sum_{j=0}^{n+4} \overline{c_{2,4}}\, \xi^j \eta^{-(\gamma-1)}\right],$$
$$\tag{3.15}$$

where $\overline{c_{2,\delta}} \equiv \widetilde{c_{2,\delta}}\Gamma(\gamma-1)/\Gamma(s+1)$ for $\delta = 2, 3, 4$.

Taking now the overall prefactor $(s/\omega_0)^{s+1}$ in Eq. (3.15) inside each of the sums and using the definition of T in Eq. (3.9)(b), we can write for any power q,

$$\left(\frac{s}{\omega_0}\right)^{s+1} \eta^{-q} = \left(\frac{s}{\omega_0}\right)^{s+1-q} T^{-q}. \tag{3.16}$$

Defining the coefficients $c_{2,\delta} \equiv \overline{c_{2,\delta}}(s/\omega_0)^{(s+2-\gamma)}$ for $\delta = 2, 3, 4$, the final result for the $O(\epsilon_c^4)$ term $U_4(t)$ is:

$$U_4 = \Lambda_{n,m} \frac{\epsilon_c^4}{\beta^2} \left[\sum_{j=0}^{n+2} c_{2,2}\, \xi^j T^{-(\gamma-1)} - \sum_{j=0}^{n+3} c_{2,3}\, \xi^j T^{-(\gamma-1)} + \sum_{j=0}^{n+4} c_{2,4}\, \xi^j T^{-(\gamma-1)}\right]. \tag{3.17}$$

Adding this result to the $O(\epsilon_c^2)$ phasor $U^{(2)}$ in Eq. (3.8), the complete $O(\epsilon_c^4)$ time-domain phasor $U^{(4)}(t)$ is:

$$U^{(4)} = \Lambda_{n,m} \left[\sum_{j=0}^{n} c_{0,0} \xi^j T^{-(\gamma+1)} + \frac{\epsilon_c^2}{\beta} \left(\sum_{j=0}^{n+1} c_{1,1} \xi^j T^{-\gamma} - \sum_{j=0}^{n+2} c_{1,2} \xi^j T^{-\gamma} \right) \right.$$
$$\left. + \frac{\epsilon_c^4}{\beta^2} \left(\sum_{j=0}^{n+2} c_{2,2} \, \xi^j T^{1-\gamma} - \sum_{j=0}^{n+3} c_{2,3} \, \xi^j T^{1-\gamma} + \sum_{j=0}^{n+4} c_{2,4} \, \xi^j T^{1-\gamma} \right) \right]. \tag{3.18}$$

The calculation of higher order terms would proceed similarly. The upper limits of the sums, their interior coefficients, the leading powers of ϵ_c^2/β, and the integrated powers of ω would change, but otherwise the process would be identical to that demonstrated above.

3.4   The fields

From the expression for the phasor $U(\mathbf{r}, t)$ in Eq. (3.8), Hertz potentials [Eq. (1.2)] can be used to generate expressions for the complex EM fields. The desired polarization of the laser field is determined by the form of these Hertz potentials, and not from any property of the phasor. As an example, for the case of radial polarization the EM fields can be expressed from the phasor as simply

$$\mathbf{E}(\mathbf{r}, t) = \nabla \times \nabla \times (U(\mathbf{r}, t)\hat{\mathbf{z}}) \tag{3.19a}$$

$$\mathbf{H}(\mathbf{r}, t) = \epsilon_0 \frac{\partial}{\partial t} \nabla \times (U(\mathbf{r}, t)\hat{\mathbf{z}}) \tag{3.19b}$$

For different polarizations, these expressions for $\mathbf{E}$ and $\mathbf{H}$ would change (see Table 3 on p. 372 of Ref. [43] and the text at the bottom of p. 361 of Ref. [43] for more details).

In the expressions that follow for the unnormalized EM fields, we have carried out calculations for all but the most simple partial derivatives of the phasor. By leaving these derivative terms in the field equations, we ensure that the expressions remain valid for

higher perturbative orders in which the phasor is modified to have additional terms.

$$
\begin{aligned}
E_\rho = -\frac{i}{\rho} \Bigg\{ & \frac{m(n+m+1)}{\beta z_R}U - \frac{2\omega_0\xi}{sz_R}\frac{\partial^2 U}{\partial\beta\partial T} + \frac{\xi(2n+3m+4)}{\beta z_R}\frac{\partial U}{\partial\xi} \\
& + \frac{\omega_0}{s}\left[\frac{2\xi(n+m+2)}{\beta z_R} + m\left(\frac{\xi}{\beta z_R} + \frac{1}{c}\right)\right]\frac{\partial U}{\partial T} - \frac{m}{z_R}\frac{\partial U}{\partial\beta} + \frac{2\xi^2}{\beta z_R}\frac{\partial^2 U}{\partial\xi^2} \\
& + \frac{2\omega_0\xi}{s}\left(\frac{2\xi}{\beta z_R} + \frac{1}{c}\right)\frac{\partial^2 U}{\partial\xi\partial T} - \frac{2\xi}{z_R}\frac{\partial^2 U}{\partial\xi\partial\beta} + \frac{2\omega_0^2\xi}{s^2}\left(\frac{\xi}{\beta z_R} + \frac{1}{c}\right)\frac{\partial^2 U}{\partial T^2} \Bigg\}
\end{aligned}
\tag{3.20}
$$

$$
E_\phi = \frac{m}{\rho}\left[\frac{n+m+1}{\beta z_R}U + \frac{\omega_0}{s}\left(\frac{\xi}{\beta z_R} + \frac{1}{c}\right)\frac{\partial U}{\partial T} + \frac{\xi}{\beta z_R}\frac{\partial U}{\partial\xi} - \frac{1}{z_R}\frac{\partial U}{\partial\beta}\right]
\tag{3.21}
$$

$$
\begin{aligned}
E_z = \frac{\xi}{\rho^2}\Bigg\{ & -\frac{4\omega_0}{s}(m+1)\frac{\partial U}{\partial T} - 4(m+1)\frac{\partial U}{\partial\xi} \\
& -\frac{4\omega_0^2\xi}{s^2}\frac{\partial^2 U}{\partial T^2} - 4\xi\frac{\partial^2 U}{\partial\xi^2} - \frac{8\omega_0\xi}{s}\frac{\partial^2 U}{\partial\xi\partial T} \Bigg\}
\end{aligned}
\tag{3.22}
$$

$$
B_\rho = -\frac{m\omega_0}{c^2 s\rho}\frac{\partial U}{\partial T}
\tag{3.23}
$$

$$
B_\phi = -\frac{i\omega_0}{c^2 s\rho}\left\{ m\frac{\partial U}{\partial T} + 2\xi\left(\frac{\omega_0}{s}\frac{\partial^2 U}{\partial T^2} + \frac{\partial^2 U}{\partial\xi\partial T}\right)\right\}
\tag{3.24}
$$

As is the case with all radially polarized fields, $B_z = 0$. The perturbative order necessary to achieve convergence will be discussed in the next section.

3.5   Results

3.5.1   Test for accuracy of fields obtained from the perturbative phasor

Depending on the parameters used to describe the optical field, perturbative orders higher than ϵ_c^2 may need to be included in the phasor. These higher order corrections are

needed not only as the spot size is reduced, but also as the radial or azimuthal LG indices are increased. Numerical simulations show that excluding terms above order ϵ_c^2 is sufficient only for the lowest LG modes.

A simple method for checking the convergence of the perturbative expansion of the phasor is to verify that the wave equation is satisfied to within some numerical tolerance. Since the phasor must be a solution to the wave equation [43], we can write explicitly

$$\nabla^2 U = \frac{1}{c^2}\frac{d^2}{dt^2}U. \tag{3.25}$$

One can check directly that the equation is satisfied at any given order of perturbation. If an appropriate perturbative order is used to represent the phasor, numerical comparison of $|\nabla^2 U|$ and $|\partial_t^2 U/c^2|$ will agree, since the wave equation will be satisfied. Disagreement, on the other hand, indicates that additional terms in the perturbative expansion must be included in order to achieve a converged phasor. We note that since all fields are calculated as derivatives of the phasor, use of Eq. (3.25) to check the adequacy of the perturbative expansion is valid for any field polarization, not just for the radially polarized fields calculated above as an example.

To illustrate this technique, a comparison of the left- and right-hand sides of Eq. (3.25) is shown in Fig. 3.1 for three LG modes, calculated for two different orders of perturbative correction. For each of the results in Fig. 3.1, we present the root mean squared error (RMSE) between $|\nabla^2 U|$ and $|\partial_t^2 U/c^2|$ calculated using 200 plot points across the range of ρ/λ shown. Convergence of the perturbative expansion can be claimed if the RMSE is sufficiently small (the exact definition of which depends on the application). The results in Figs. 3.1(d) - 3.1(f) show improved agreement between the left- and right-hand sides of the wave equation over those in Figs. 3.1(a) - 3.1(c), respectively, as the order of perturbation increases from $O(\epsilon_c^2)$ to $O(\epsilon_c^4)$. However, agreement between these terms becomes worse as the LG mode increases from $n = 2$ to $n = 3$ for both the phasors of $O(\epsilon_c^2)$ and those of $O(\epsilon_c^4)$, thus illustrating the need to check for
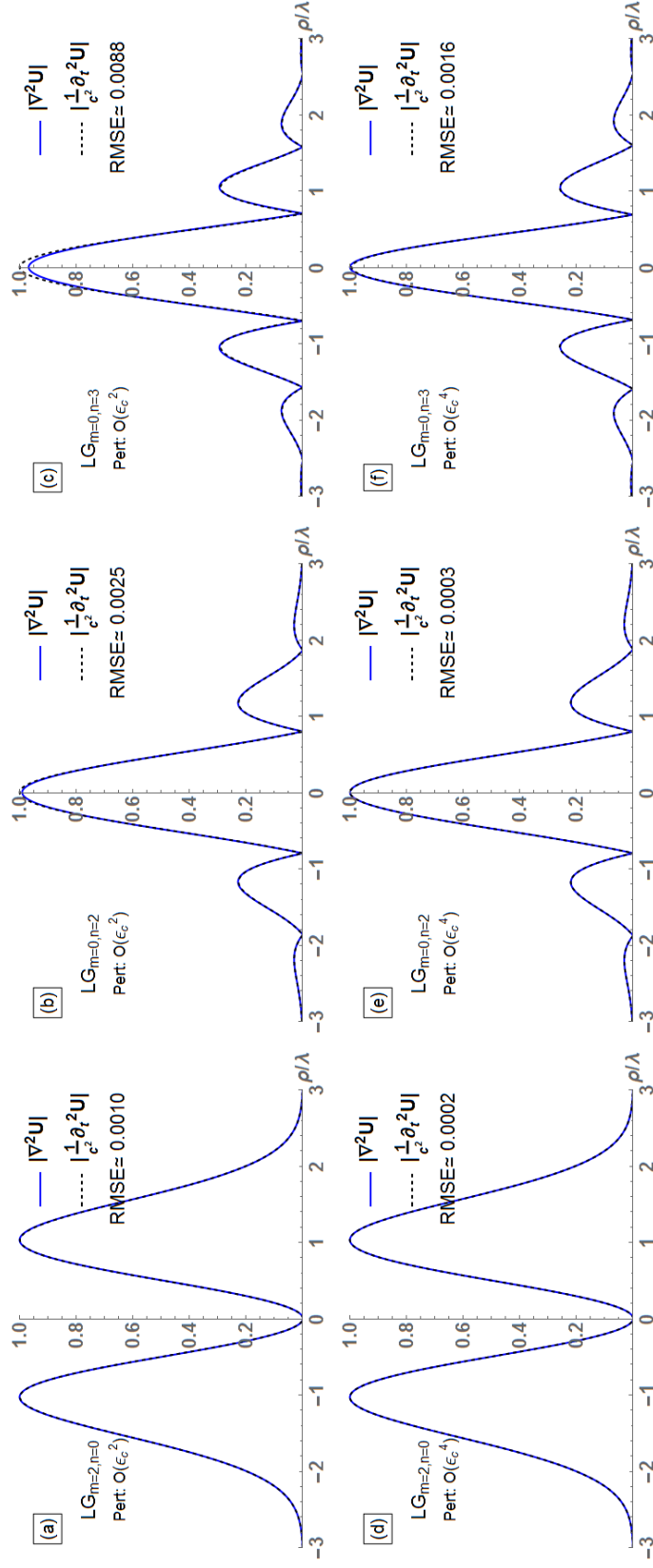
Figure 3.1: Comparison of both sides of the wave equation [Eq. (3.25)] for the phasor, $|\nabla^2 U|$ and $|\partial_t^2 U/c^2|$, for three LG modes, calculated for two different orders of perturbative correction. Panels [(a),(d)] show LG mode $m = 2, n = 0$, panels [(b),(e)] show $m = 0, n = 2$, and panels [(c),(f)] show $m = 0, n = 3$. The phasor contains perturbation terms to order ϵ_c^2 in [(a)-(c)] and to order ϵ_c^4 in [(d)-(f)]. The RMS error decreases when the higher order term is included in the phasor. These plots were made near the beam waist using $s = 70$ and $w_0 = \lambda = 800$ nm ($\epsilon_c^2 \approx 0.0253$).

Figure 3.2: Comparison of numerical values of the relative intensities of fields E_ρ and E_z near the beam waist for the $LG_{0,0}$ mode for two different spectral parameters: (a) s=2848 ($\sim$20-cycle FWHM, 53.4 fs) or (b) s=7 ($\sim$1-cycle FWHM, 2.65 fs). Solid dark (blue) and light (gray) curves are calculated using fields derived from April's phasor [43] ("A"), while the dashed and dash-dot curves are calculated from the fields given in Eqs. (3.20) and (3.22) of this chapter with the phasor to perturbative order ϵ_c^2 ("pert"), all with $w_0 = 1.5\lambda$ and $\lambda = 800$ nm ($\epsilon_c^2 \approx 0.0113$).

convergence. Calculations for other LG modes having indices $n + m \leq 3$ (not shown) have RMSE values similar to those for the LG modes shown in Fig. 3.1 when corrections to similar perturbative orders are included.

We emphasize that the addition of higher order corrections to the phasor does not change the EM field equations that have been derived in Sec. 3.4. The expressions for the EM fields given in Eqs. (3.20)-(3.24) remain valid as the phasor is modified, since these field expressions are written in terms of partial derivatives of the phasor. Thus, use of our field equations for higher perturbative orders is relatively straightforward, requiring only the addition of higher order corrections to the phasor (cf. Sec. 3.3).

In Fig. 3.2 we compare our converged fields from Eqs. (3.20) and (3.22) with those obtained from the closed-form phasor of April [43]. The normalized electric field intensities in the $\hat{\rho}-$ and $\hat{\mathbf{z}}-$directions are shown for each model, for both long and short pulse durations. Excellent agreement is seen between the fields of our model (subscript "pert" in the figure) and those of April (subscript "A"), for both long (Fig. 3.2a) and short (Fig. 3.2b) pulses.

3.5.2 Sensitivity of the fields to the spectral profile

The EM fields are calculated using the time-domain phasor $U(t)$, which may be obtained in one of two ways. The exact way, as done in Sec. 3.2, is to Fourier transform the frequency-domain phasor to the time domain according to Eq. (3.7). An approximate approach is to multiply the monochromatic phasor by a temporal Gaussian envelope, as follows:

$$U(\mathbf{r}, t) = U_{BGV}(\mathbf{r}, \omega_0) \exp \left[-i\omega_0 t - \frac{(t - z/c)^2}{\tau^2} \right].$$ (3.26)

While these two methods may agree for longer pulse durations, it is known that use of a Gaussian temporal envelope as in Eq. (3.26) fails to correctly model the behavior of ultrashort pulses [79].

The problem may be understood by considering the time-frequency uncertainty relation, i.e., that the spectral bandwidth grows as the pulse length decreases. For sufficiently short pulses, the bandwidth becomes so large that negative frequency components enter with appreciable weight. These nonphysical frequencies may cause the electric fields to grow with transverse distance from the optical axis instead of decay, as required for a physically correct model [40].

A Poisson-like frequency spectrum was used in the derivation of our phasor in Sec. 3.2 to correctly model the behavior of ultrashort pulses. Owing to its inherent unit

step function $\Theta(\omega)$, a Poisson-like spectrum removes unphysical negative frequency components from the frequency-domain phasor. Thus, upon Fourier transformation into the time domain, one eliminates the possibility of nonphysical temporal fields.
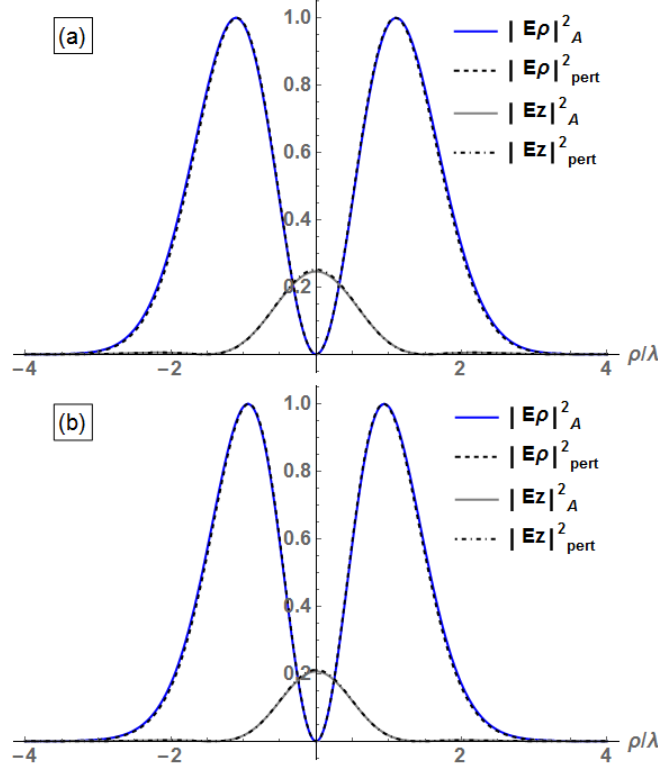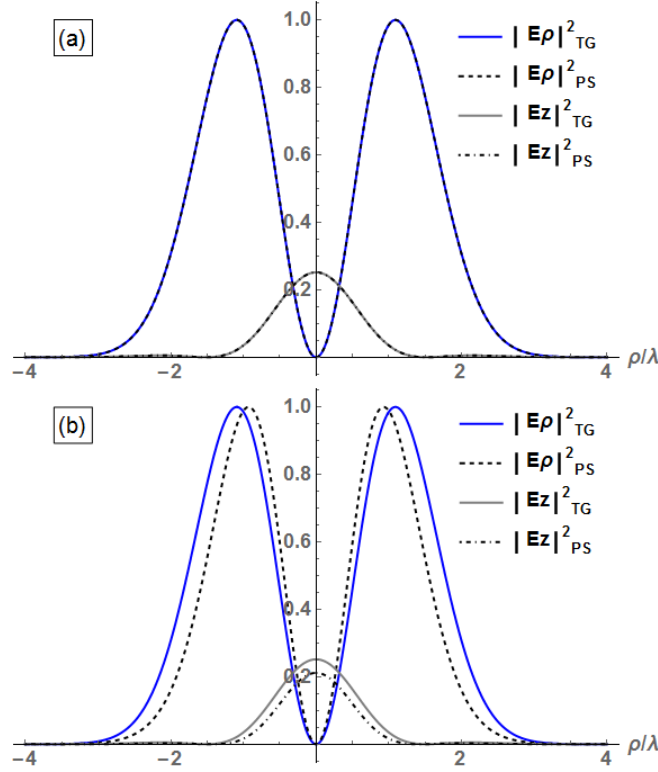

Figure 3.3: Comparison of numerical values of the relative intensities of fields E_ρ and E_z near the beam waist for the $LG_{0,0}$ mode for two different spectral parameters: (a) s=2848 ($\sim$20-cycle FWHM, 53.4 fs) or (b) s=7 ($\sim$1-cycle FWHM, 2.65 fs). Solid dark (blue) and light (gray) curves are calculated using the temporal Gaussian ("TG") model of Eq. (3.26) with the indicated pulse durations, while the dashed and dash-dot curves are calculated using the Fourier transformed Poisson spectrum ("PS") of Eq. (3.7) to order ϵ_c^2, all with $w_0 = 1.5\lambda$ and $\lambda = 800$ nm ($\epsilon_c^2 \approx 0.0113$).

A comparison of the fields calculated from the time-domain phasors defined in Eqs. (3.7) and (3.26) for two different pulse durations is given in Fig. 3.3. As shown in Fig. 3.3(b) for short pulses, the fields generated from a temporal Gaussian envelope [Eq. (3.26)] (subscript "TG") clearly differ from those generated from the Poisson spectrum phasor (subscript "PS"). In contrast, for long pulses, Fig. 3.3(a) shows much better agreement between the fields generated by the two different methods. This better

agreement occurs since the frequency bandwidth of the temporal Gaussian doesn't extend to negative values in the case of a long pulse. Note that the "PS" fields in Fig. 3.3 are the same as the "pert" fields in Fig. 3.2.

3.6   Radius of convergence of the perturbative phasor

Perturbative models require that higher-order terms in the perturbative expansion have smaller magnitude than lower-order terms, so that the infinite series converges. However, the series expansions upon which such perturbations are based often do not have this behavior in all space. For example, the one-dimensional function $1/(x^2 + 1)$ is well-defined at all values on the real axis. Expanding this function in a Maclaurin series gives $1 - x^2 + x^4 + ...$ which only converges in the finite region $|x| < 1$, rendering the series expansion useless outside this radius of convergence. In this section, we estimate the radius of convergence for the perturbative phasor presented in Eq. (3.1) of this chapter.

We begin by considering the magnitude of the frequency-domain phasor in Eq. (3.1). Each term in the perturbative sum contains a factor $f_{n,m}^{(2j)}(v)$, derived in Appendix A, which is a sum of associated Laguerre polynomials. At some perturbative order j, the dominant contribution to $f_{n,m}^{(2j)}(v)$ is

$$f_{n,m}^{(2j)}(v) \approx \frac{(n+2j)!}{j!} L_{n+2j}^m(v), \tag{3.27}$$

since $L_{n+2j}^m(v)$ has the highest power of v amongst all associated Laguerre polynomials contributing to $f_{n,m}^{(2j)}(v)$ [cf. Eqs. (3.2) and (3.3)]. The term in $L_{n+2j}^m(v)$ having the highest power of v is $G_{(n+2j,m,n+2j)}v^{n+2j}$ [cf. Eq. (3.3)]. Making use of Eq. (3.4), and noting that $|h| = (1 + z^2/z_R^2)^{-1/4}$, one can write the magnitude of the dominant contribution to the jth-order term of Eq. (3.1) as

$$\left|U^{(2j)}\right| \approx \frac{2^{2n+m}\epsilon^{2j}}{j!} \left(1 + \frac{z^2}{z_R^2}\right)^{-\frac{1}{2}(2n+3j+m+1)} \exp\left[-\frac{\rho^2}{\mathrm{w}_0^2\left(1 + z^2/z_R^2\right)}\right]\left(\frac{\rho}{\mathrm{w}_0}\right)^{2n+4j+m}.$$
(3.28)

As noted above, the radius of convergence is defined by the spatial region in which the term of order j is smaller than the term of order $j-1$. To find such a region, we calculate the difference $\left|U^{(2j)}\right| - \left|U^{(2j-2)}\right| < 0$. Given that $\rho \geq 0$ and $z^2 \geq 0$, this inequality can only be satisfied for

$$\rho < \left[j\left(1 + \frac{z^2}{z_R^2}\right)^{3/2}\frac{\mathrm{w}_0^4}{\epsilon^2}\right]^{1/4}.$$
(3.29)

It is sufficient to say that the phasor is converged if this condition is satisfied for all j, and the maximum allowed value of ρ increases with larger j. Therefore, the radius of convergence ρ_c is determined by the minimal case of $j = 1$,

$$\rho < \left[\left(1 + \frac{z^2}{z_R^2}\right)^{3/2}\frac{\mathrm{w}_0^4}{\epsilon^2}\right]^{1/4} \equiv \rho_c.$$
(3.30)

Note that ρ_c is defined for any z and is independent of the LG modes n and m.

This radius of convergence is demonstrated in Fig. 3.4, wherein the magnitude of the perturbative phasor given in Eq. (3.28) is plotted as a function of ρ and z for up to three orders of perturbative correction. The minimum radius of convergence ρ_c is given in Eq. (3.30), which corresponds to the line between regions 0 and 1 in Fig. 3.4. The space with ρ-values below this line corresponds to the region of perturbative convergence, or the region in which the 0th-order phasor is dominant.
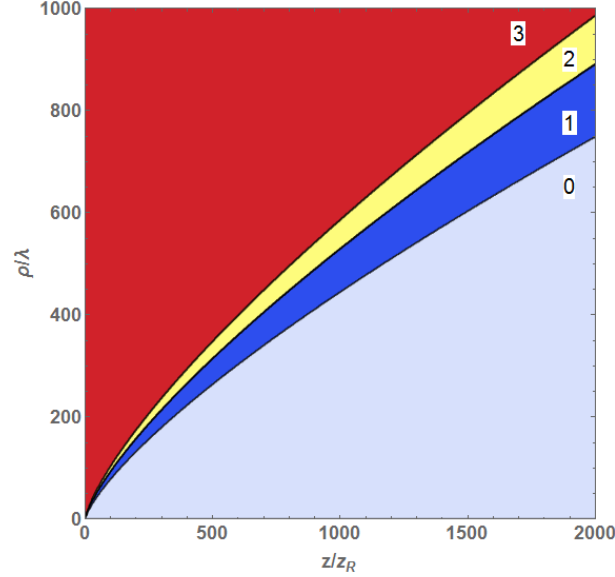
Figure 3.4: Illustration of the radius of convergence for the phasor in Eq. (3.1), demonstrated by the dominant perturbative order j as a function of spatial location. Each region is labeled by the perturbative order $j \in [0, 3]$ that is largest therein. The region in which the $j = 0$ term dominates is the region in which the perturbation is converged. This plot was made using $\mathrm{w}_0 = \lambda = 800$ nm $[\epsilon = 1/(2\pi)]$.

3.7   Summary

In this chapter we have presented an analytic method for calculating the EM fields of a tightly focused, arbitrarily-short laser pulse of any radial and azimuthal LG mode. In brief, the EM fields are obtained from the time-domain phasor, whose analytic expression to the ϵ_c^2 perturbative order is given in Eq. (3.8). An example for obtaining the phasor to higher orders in ϵ_c^2 is given in Sec. 3.3. For the case of radially-polarized EM fields, Eqs. (3.19) - (3.24) show how to obtain the EM fields from the phasor of any perturbative order. With only lowest order perturbative corrections included, these fields are consistent with the field model of April [43] for the Gaussian mode over a wide range of pulse durations. Use of a Poisson-like frequency spectrum was essential to obtain this agreement, as this spectrum eliminates the possibility of negative frequency modes that lead to unphysical fields for ultrashort pulses.

Invoking the condition of isodiffraction is necessary for solving the Fourier integral of the phasor when transforming it into the time domain. The phasor for a completely general nonparaxial eLG beam, valid for arbitrarily short pulses, has never to our knowledge been expressed in the time domain without use of the isodiffraction condition, as otherwise the necessary Fourier integral becomes prohibitively complicated. For nonparaxial complex source-point models, this condition of isodiffraction requires that the imaginary distance to the source point, z_R in this case, remains frequency-independent.

A major benefit of our perturbative model is its scalability to higher radial and orbital LG modes. Expressions for the time-domain EM fields for these higher LG modes using other models usually requires the calculation of infinite sums or the evaluation of integrals involving special functions of complex variables. The integrals over these complex special functions, for arbitrary LG modes, are difficult to evaluate. In our model, all EM fields are written simply in terms of the phasor and its elementary derivatives.

Chapter 4

Generalization to Arbitrary Perturbative Order in the Time Domain

4.1 Introduction

Perturbative models have long provided a straightforward means of calculating the EM fields of optical beams with various spatiotemporal structures [33, 45, 64, 65, 67]. To be generally applicable, such models must allow for the accurate description of beams which are focused to arbitrarily-small spot sizes, have arbitrarily-short temporal durations [45], and carry arbitrarily-many quanta of orbital angular momentum (OAM) [45, 66, 67], among other properties. The OAM carried by such beams is expressed in the form of optical vortices [2, 11–13], whereby the phase of a beam's EM fields exhibits a helical structure about the optical axis.

Perturbative models generally entail a power series expansion in a parameter that is small in the paraxial limit of loose focusing, such as $(k\mathrm{w}_0)^{-1}$ [33, 34, 38, 45, 60, 64, 65, 67] or $(k_\perp/k)$ [67], where k is the wave number and w_0 is the beam waist. The zeroth order term of such a series represents the optical beam in the paraxial limit, and higher order terms introduce nonparaxial corrections. Notably, the first-order correction introduces the

longitudinal electric field that is characteristic of nonparaxial beams [33]. In practice, perturbative models retain terms only up to a predetermined order of perturbation, at which point the infinite series is truncated.

A perturbative model describing tightly-focused eLG beams was presented by BGV in Ref. [67], but this result was limited to a frequency-domain description for the case of monochromatic fields. Chapter 3 extended this description in two ways: i) it modified the model of BGV by introducing a frequency spectrum, thus allowing for the description of pulses with arbitrary temporal duration; and ii) it Fourier transformed this modified frequency-domain phasor into the time domain, from which one can obtain the EM fields by straightforward differentiation. The first two orders of perturbative correction to the time-domain phasor were also presented in Chapter 3, and a method for generating higher order corrections was described in detail.

A main benefit of using such perturbative models is the ability to calculate the EM fields using relatively simple expressions at each retained order of perturbative correction. While exact models, such as that of Ref. [43], accurately describe such beams in the frequency domain, it can be cumbersome to generate the corresponding time-domain descriptions, which are required for calculating the EM fields. In particular, the Fourier transformations necessary to bring the frequency-domain models into the time domain are often difficult to carry out owing to the mathematically-complicated nature of exact descriptions, particularly as the LG mode indices become large.

A major issue for perturbative descriptions, of course, is the convergence of the perturbation series describing the EM fields. For the model presented in Chapter 3, it was shown that the number of terms that must be retained in the perturbation series in order to achieve convergence depends not only on the spot size of the beam but also on the LG mode. For beams carrying large values of OAM (which can be created, e.g., in high-harmonic generation processes [6, 13, 26]), the perturbative order required to

achieve convergence can become large. Thus, the ability to express a time-domain phasor to arbitrary perturbative order would be of great utility for general application of perturbative models to the calculation of EM fields in cases becoming increasingly relevant in experiments involving tightly-focused, highly-structured pulses of light.

In this chapter we generalize the perturbative results of Chap. 3 by extending the time-domain description to arbitrarily-high perturbative order as a non-recursive, closed-form analytic expression. This generalized time-domain phasor allows one to implement the perturbative model without requiring explicit calculation of any Fourier integrals, which would be prohibitively difficult to calculate individually for each term of an arbitrarily-high order of perturbative correction. Instead, the EM fields can be calculated immediately from straightforward derivatives of the generalized time-domain phasor we present here.

This Chapter is organized as follows. In Section 4.2 the third-order correction to the phasor presented in Chapter 3 is explicitly derived in the time domain via Fourier integration. We then propose a generalization of this time-domain phasor that is valid to any perturbative order. In Sections 4.3 and 4.4, our proposed generalized time-domain phasor is derived analytically. An integral result used in these derivations is derived in Appendix B. Finally, in Sec. 4.5 we summarize our results.

4.2 The time-domain phasor

The polychromatic time-domain phasor presented in Chap. 3 is an exact solution to the scalar HE. In Chap. 3 a second-order perturbative expression for this phasor was derived that is appropriate for describing the spatiotemporal profile of an arbitrarily-short laser pulse of any LG mode focused to an arbitrarily-small spot size. The result therein is perturbative in the small parameter $\epsilon_c^2 \equiv c/(2z_R\omega_0)$, where z_R is the Rayleigh range, ω_0 is the central frequency of the pulse, and c is the speed of light. In Section 4.2.1, we

extend this time-domain description up to the third order correction (i.e., up to order ϵ_c^6) via explicit Fourier transformation. Then in Section 4.2.2 we compare the second-order phasor with its third-order correction [Eqs. (3.18) and (4.8) respectively] and suggest how the time-domain phasor can be almost completely predicted to any perturbative order. In Section 4.4 of this paper, we then prove analytically (using some necessary results derived in Section 4.3) the proposed expression of the time-domain phasor in Section 4.2.2 for any perturbative order.

4.2.1 Derivation of the third-order correction

We now proceed to derive the time-domain phasor, $U^{(6)}(t)$, which is correct to third order in the parameter ϵ_c^2. According to the procedure given in Sec. 3.3, we start from the perturbative, monochromatic frequency-domain phasor of BGV [67], replicated from Eq. (3.1) for convenience,

$$
\begin{aligned}
U_{BGV}\left(\mathbf{r}, \omega\right) &= (-1)^{n+m} 2^{2n+m} \exp(ikz + im\phi) \\
&\quad \times h^{2n+m+2} v^{m/2} \exp(-v) \sum_{j=0}^{N} \left(\frac{h^2}{k^2 \mathbf{w}_0^2}\right)^j f_{n,m}^{(2j)}(v) \\
&\equiv U_{0,BGV} + \frac{\epsilon^2}{\beta} U_{2,BGV} + \frac{\epsilon^4}{\beta^2} U_{4,BGV} + \dots \quad ,
\end{aligned}
\tag{4.1}
$$

in which $\mathbf{w}_0$ is the beam waist, $z_R = k\mathbf{w}_0^2/2$ is the Rayleigh length, $h = (1 + iz/z_R)^{-1/2}$, $\beta = 1/h^2$, and $v = h^2\rho^2/\mathbf{w}_0^2$ are dimensionless parameters, and the factors $f_{n,m}^{(2j)}(v)$ are presented by BGV as terms in a series expansion (cf. Appendix A). In order to describe short-pulse fields, we multiply Eq. (4.1) with a Poisson-like frequency spectrum [cf. Eq. (2.5)]. Henceforth, we follow the prescription in Sec. 3.3 to derive here the third-order correction to the time-domain phasor.

Considering only the third-order term in Eq. (4.1), where $f^{(6)}$ is given in Eq. (25) of Ref. [67] [see Eq. (4.11d) below], we make the replacements $\mathbf{w}_0 \to \sqrt{2z_R/k}$ and $k \to \omega/c$ to show explicitly the frequency dependencies. We also invoke here the condition of

isodiffraction, which requires that z_R is independent of frequency [40, 62, 87]. The third-order frequency-domain phasor term is then

$$
\begin{aligned}
\frac{\epsilon^6}{\beta^3} U_{6,BGV} = {}& (-1)^{n+m} 2^{2n+m} \exp(i\omega z/c + im\phi) \\
& \times h^{2n+m+2} v^{m/2} \exp(-v) \left[\left(\frac{c}{2\omega\beta z_R} \right)^3 \right. \\
& \times \left\{ 20(n+3)! L_{n+3}^m(v) - 15(n+4)! L_{n+4}^m(v) \right. \\
& \left. \left. + 3(n+5)! L_{n+5}^m(v) - \frac{1}{6}(n+6)! L_{n+6}^m(v) \right\} \right].
\end{aligned}
\tag{4.2}
$$

Upon multiplying this result by the Poisson-like frequency spectrum in Eq. (2.5), the description becomes polychromatic. Therefore, the small parameter ϵ, which is appropriate for monochromatic fields, must be replaced with the frequency independent small parameter ϵ_c defined in Eq. (3.6). Then, expressing the associated Laguerre polynomials in Eq. (4.2) as sums [see Eqs. (3.3) and (3.4)], substituting $v = \xi\omega$, and extracting powers of ω within the sums, we obtain finally

$$
\begin{aligned}
U_6(\omega) = {}& \frac{\Lambda_{n,m}}{\Gamma(s+1)} \exp\left\{ -\omega\left(-\frac{iz}{c} + \xi + \frac{s}{\omega_0} \right) \right\} \\
& \times \left(\frac{s}{\omega_0} \right)^{s+1} \frac{\Theta(\omega)\sqrt{2\pi}\epsilon_c^6}{\beta^3} \left[\sum_{j=0}^{n+3} \widetilde{c_{3,3}}\, \xi^j \omega^{\gamma-3} \right. \\
& - \sum_{j=0}^{n+4} \widetilde{c_{3,4}}\, \xi^j \omega^{\gamma-3} + \sum_{j=0}^{n+5} \widetilde{c_{3,5}}\, \xi^j \omega^{\gamma-3} \\
& \left. - \sum_{j=0}^{n+6} \widetilde{c_{3,6}}\, \xi^j \omega^{\gamma-3} \right],
\end{aligned}
\tag{4.3}
$$

where some variables defined in Eq. (3.9) and the preceding paragraph have been used, and new coefficients $\widetilde{c_{3,\delta}}$, $\delta \in [3, 6]$ are defined as follows:

$$\widetilde{c_{3,3}} \equiv 20\omega_0^3 \frac{(n+3)!}{n!} G_{(n+3),m,j} \tag{4.4a}$$

$$\widetilde{c_{3,4}} \equiv 15\omega_0^3 \frac{(n+4)!}{n!} G_{(n+4),m,j} \tag{4.4b}$$

$$\widetilde{c_{3,5}} \equiv 3\omega_0^3 \frac{(n+5)!}{n!} G_{(n+5),m,j} \tag{4.4c}$$

$$\widetilde{c_{3,6}} \equiv \frac{\omega_0^3}{6} \frac{(n+6)!}{n!} G_{(n+6),m,j}. \tag{4.4d}$$

We now Fourier transform $U_6(\omega)$ to the time domain using Eq. (3.7) to obtain $U_6(t)$,

$$
\begin{aligned}
U_6(t) = & \frac{\Lambda_{n,m}}{\Gamma(s+1)} \left(\frac{s}{\omega_0}\right)^{s+1} \frac{\epsilon_c^6}{\beta^3} \int_0^\infty \exp(-\omega\eta) \\
& \times \left[\sum_{j=0}^{n+3} \widetilde{c_{3,3}}\, \xi^j \omega^{\gamma-3} - \sum_{j=0}^{n+4} \widetilde{c_{3,4}}\, \xi^j \omega^{\gamma-3} \right. \\
& \left. + \sum_{j=0}^{n+5} \widetilde{c_{3,5}}\, \xi^j \omega^{\gamma-3} - \sum_{j=0}^{n+6} \widetilde{c_{3,6}}\, \xi^j \omega^{\gamma-3} \right] d\omega,
\end{aligned}
\tag{4.5}
$$

where $\eta \equiv -iz/c + \xi + s/\omega_0 + it$. Making use of the integral representation of the gamma function [cf. Eq. (2.21)], the Fourier integral in Eq. (4.5) can be evaluated to obtain

$$
\begin{aligned}
U_6(t) = \Lambda_{n,m} \left(\frac{s}{\omega_0}\right)^{s+1} \frac{\epsilon_c^6}{\beta^3} & \left[\sum_{j=0}^{n+3} \overline{c_{3,3}}\, \xi^j \eta^{-(\gamma-2)} - \sum_{j=0}^{n+4} \overline{c_{3,4}}\, \xi^j \eta^{-(\gamma-2)} \right. \\
& \left. + \sum_{j=0}^{n+5} \overline{c_{3,5}}\, \xi^j \eta^{-(\gamma-2)} - \sum_{j=0}^{n+6} \overline{c_{3,6}}\, \xi^j \eta^{-(\gamma-2)} \right],
\end{aligned}
\tag{4.6}
$$

where $\overline{c_{3,\delta}} \equiv \widetilde{c_{3,\delta}} \Gamma(\gamma-2)/\Gamma(s+1)$ for $\delta \in [3,6]$.

Taking now the overall prefactor $(s/\omega_0)^{s+1}$ in Eq. (4.6) inside each of the sums and using the definition of T in Eq. (3.9), we can write for any power q,

$$\left(\frac{s}{\omega_0}\right)^{s+1} \eta^{-q} = \left(\frac{s}{\omega_0}\right)^{s+1-q} T^{-q}. \tag{4.7}$$

Defining the coefficients $c_{3,\delta} \equiv \overline{c_{3,\delta}}(s/\omega_0)^{(s+3-\gamma)}$ for $\delta \in [3,6]$, the final result for the third-order term $U_6(t)$ is:

$$U_6(t) = \Lambda_{n,m} \frac{\epsilon_c^6}{\beta^3} \left[\sum_{j=0}^{n+3} c_{3,3}\, \xi^j T^{-(\gamma-2)} - \sum_{j=0}^{n+4} c_{3,4}\, \xi^j T^{-(\gamma-2)} \right. $$
$$\left. + \sum_{j=0}^{n+5} c_{3,5}\, \xi^j T^{-(\gamma-2)} - \sum_{j=0}^{n+6} c_{3,6}\, \xi^j T^{-(\gamma-2)} \right]. \tag{4.8}$$

Finally, combining this result with that for the phasor including corrections up to second order [Eq. (3.18)], the complete third-order time-domain phasor is written as

$$U^{(6)} = \Lambda_{n,m} \left[\sum_{j=0}^{n} c_{0,0}\xi^j T^{-(\gamma+1)} + \frac{\epsilon_c^2}{\beta} \left(\sum_{j=0}^{n+1} c_{1,1}\xi^j T^{-\gamma} - \sum_{j=0}^{n+2} c_{1,2}\xi^j T^{-\gamma} \right) \right.$$
$$+ \frac{\epsilon_c^4}{\beta^2} \left(\sum_{j=0}^{n+2} c_{2,2}\, \xi^j T^{1-\gamma} - \sum_{j=0}^{n+3} c_{2,3}\, \xi^j T^{1-\gamma} + \sum_{j=0}^{n+4} c_{2,4}\, \xi^j T^{1-\gamma} \right)$$
$$+ \frac{\epsilon_c^6}{\beta^3} \left(\sum_{j=0}^{n+3} c_{3,3}\, \xi^j T^{-(\gamma-2)} - \sum_{j=0}^{n+4} c_{3,4}\, \xi^j T^{-(\gamma-2)} + \sum_{j=0}^{n+5} c_{3,5}\, \xi^j T^{-(\gamma-2)} \right.$$
$$\left. \left. - \sum_{j=0}^{n+6} c_{3,6}\, \xi^j T^{-(\gamma-2)} \right) \right]. \tag{4.9}$$

4.2.2 Proposed expression for the phasor to perturbative order Δ

Comparing the terms of each perturbative order in the third-order time-domain phasor shown in Eq. (4.9), one surmises that a term corresponding to a correction of perturbative order α has the form:

$$U_{(2\alpha)}(t) = \Lambda_{n,m} \left[\frac{\epsilon_c^{2\alpha}}{\beta^\alpha} \sum_{\delta=\alpha}^{2\alpha} \left\{ \sum_{j=0}^{n+\alpha} \left(c_{\alpha,\delta}\xi^j T^{-\gamma-1+\alpha} \right) \right\} \right], \tag{4.10}$$

Before proving this result, one must first determine the general form of the coefficients $c_{\alpha,\delta}$. As shown thus far, up to correction $\alpha = 3$, these coefficients are related to the coefficients in the expressions for the factors $f_{n,m}^{2j}(v)$ that appear in the

monochromatic frequency-domain phasor of BGV [Eq. (4.1)]. The first four of these factors are given in Eq. (25) of Ref. [67], i.e., for $j \in [0, 3]$:

$$f_{n,m}^{(0)}(v) = n! L_n^m(v) \tag{4.11a}$$

$$f_{n,m}^{(2)}(v) = 2(n+1)! L_{n+1}^m(v) - (n+2)! L_{n+2}^m(v) \tag{4.11b}$$

$$f_{n,m}^{(4)}(v) = 6(n+2)! L_{n+2}^m(v) - 4(n+3)! L_{n+3}^m(v)$$
$$+ \frac{1}{2}(n+4)! L_{n+4}^m(v) \tag{4.11c}$$

$$f_{n,m}^{(6)}(v) = 20(n+3)! L_{n+3}^m(v) - 15(n+4)! L_{n+4}^m(v)$$
$$+ 3(n+5)! L_{n+5}^m(v) - \frac{1}{6}(n+6)! L_{n+6}^m(v). \tag{4.11d}$$

Comparing Eqs. (3.10), (3.13), and (4.4) to (4.11), one can immediately see that the numerical coefficients of $c_{\alpha,\delta}$ are exactly those of $f^{(2\alpha)}(v)$ (up to a sign). For example, the three numerical coefficients of $c_{3,\delta}$ in Eq. (4.4), namely $(20, 15, 3, 1/6)$, are exactly those of the three terms of $f^{(6)}(v)$ in Eq. (4.11) (up to a sign).

In order to obtain a closed-form analytic expression for the correction of order α to the time-domain phasor in Eq. (4.10), two tasks are therefore necessary. First, a general expression for the factors $f_{n,m}^{(2\alpha)}(v)$ in Eq. (4.1) must be derived for any perturbative order Δ. This derivation is presented in Sec. 4.3. Second, the order α correction to the frequency-domain phasor shown in Eq. (4.1) must be multiplied by a Poisson-like frequency spectrum and then Fourier-transformed into the time domain. This derivation is presented in Sec. 4.4.

For convenience, we present here the final result for the complete time-domain phasor, containing all corrections up to order $\alpha = \Delta$:

$$U^{(2\Delta)}(t) = \sum_{\alpha=0}^{\Delta} U_{(2\alpha)}(t)$$

$$= \Lambda_{n,m} \sum_{\alpha=0}^{\Delta} \left[\frac{\epsilon_c^{2\alpha}}{\beta^{\alpha}} \sum_{\delta=\alpha}^{2\alpha} \left\{ \sum_{j=0}^{n+\delta} \left(c_{\alpha,\delta} \xi^j T^{-\gamma-1+\alpha} \right) \right\} \right], \tag{4.12}$$

where the coefficients $c_{\alpha,\delta}$ are given by

$$c_{\alpha,\delta} \equiv \kappa_{\alpha,\delta} G_{(n+\delta),m,j} \frac{(n+\delta)!}{n!} \omega_0^{\alpha} \left(\frac{s}{\omega_0} \right)^{s-\gamma+\alpha} \frac{\Gamma(\gamma+1-\alpha)}{\Gamma(s+1)}, \tag{4.13}$$

with

$$\kappa_{\alpha,\delta} = \frac{(-1)^{\delta-\alpha}}{(\delta-\alpha)!} \binom{2\alpha}{2\alpha-\delta}, \tag{4.14}$$

and T and γ having been defined in Eq. (3.9) and Eq. (3.10), respectively.

Equations (4.12)-(4.14) are the main results of this Chapter. They provide a closed-form analytic expression for the time-domain phasor $U^{(2\Delta)}(t)$ correct to an arbitrary perturbative order Δ in the parameter ϵ_c^2. This phasor can be utilized directly to calculate the fields for a general eLG mode without requiring the calculation of any Fourier integrals. It is easily confirmed that Eq. (4.12) is consistent with the result for $\Delta = 2$ in Eq. (3.18) and that the $\alpha = 3$ correction in Eq. (4.3) is consistent with Eq. (4.10) for $U_{(2\alpha)}(t)$. A full derivation of the Fourier transformation necessary to obtain Eqs. (4.12)-(4.14) are presented in Sec. 4.4, after first deriving expressions for the factors $f_{n,m}^{(2\alpha)}(v)$ in the next section.

4.3 Explicit derivation of $f_{n,m}^{(2\alpha)}(v)$

In this section, we derive a general expression for the factors $f_{n,m}^{(2\alpha)}(v)$ for any α. We begin by finding a generating function $\Psi(x,y)$ for the associated Laguerre polynomials, $L_n^n(y)$. We then connect this generating function to the results of BGV [67] in order to

determine a general analytic expression for $f_{n,m}^{(2\alpha)}(v)$.

4.3.1 A generating function for $L_n^n(y)$

We seek a generating function for an associated Laguerre polynomial with equal upper and lower indices,

$$\Psi(x,y) = \sum_{n=0}^{\infty} x^n L_n^n(y). \tag{4.15}$$

An associated Laguerre polynomial is expressible as an integral of a Bessel function of the first kind, as given by Eq. (22.10.14) of Ref. [88]:

$$L_n^n(y) = \frac{e^y y^{-n/2}}{n!} \int_0^{\infty} dt \, e^{-t} t^{3n/2} J_n\left(2\sqrt{ty}\right). \tag{4.16}$$

By substituting Eq. (4.16) into Eq. (4.15), one obtains

$$\Psi(x,y) = e^y \int_0^{\infty} dt \, e^{-t} \sum_{n=0}^{\infty} \left[\frac{a^n}{n!} J_n\left(2\sqrt{ty}\right) \right], \tag{4.17}$$

where $a \equiv xt^{3/2}y^{-1/2}$. This sum can be rewritten as a Bessel function using Eq. (19.9.1) of Ref. [89],

$$\sum_{n=0}^{\infty} \left[\frac{a^n}{n!} J_n\left(2\sqrt{ty}\right) \right] = J_0\left(\sqrt{4ty - 4a\sqrt{ty}} \right)$$
$$= J_0\left(2i\sqrt{x}\sqrt{t^2 - \frac{ty}{x}} \right). \tag{4.18}$$

Making this replacement in Eq. (4.17),

$$\Psi(x,y) = e^y \int_0^{\infty} dt \, e^{-t} J_0\left(2i\sqrt{x}\sqrt{t^2 - \frac{ty}{x}} \right), \tag{4.19}$$

one notices that the integral can be solved by applying Eq. (6.616.1) of Ref. [90],

$$\int_0^\infty \mathrm{d}x\, e^{-t} J_0\left(2i\sqrt{x}\sqrt{t^2 - \frac{ty}{x}}\right)$$

$$= \frac{1}{\sqrt{1-4x}} \exp\left[\frac{y}{2x}\left(\sqrt{1-4x}-1\right)\right]. \tag{4.20}$$

The result for the generating function in Eq. (4.15) is thus

$$\Psi(x,y) = \frac{1}{\sqrt{1-4x}} \exp\left[y\left(1 + \frac{\sqrt{1-4x}-1}{2x}\right)\right]. \tag{4.21}$$

4.3.2 Derivation of $f_{n,m}^{(2\alpha)}(v)$ from $\Psi(x,y)$

In Ref. [67], the factors $f_{n,m}^{(2\alpha)}(v)$ are generated from a series $G^{(2\alpha)}$ which is not explicitly defined for $\alpha > 3$. However, comparing Eqs. (16) & (22) of Ref. [67] (as shown explicitly in Appendix A), one sees that

$$\sum_{\alpha=0}^\infty \epsilon^{(2\alpha)} G^{(2\alpha)} = \frac{1}{\sqrt{1-\epsilon^2\Omega}} \exp\left(\frac{\sqrt{1-\epsilon^2\Omega}-1}{2\epsilon^2 h^2} + \frac{\Omega}{4h^2}\right), \tag{4.22}$$

where $\epsilon \equiv 1/(kw_0)$ has been defined as the small parameter of the perturbation, which at this point is monochromatic, and $\Omega \equiv w_0^2 k_\perp^2$. By taking $x = \epsilon^2\Omega/4$ and $y = \Omega/(4h^2)$ in Eq. (4.21), we see immediately by comparison to Eq. (4.22) that

$$\Psi(x,y) = \sum_{n=0}^\infty x^n L_n^n(y) = \sum_{\alpha=0}^\infty \epsilon^{(2\alpha)} G^{(2\alpha)}. \tag{4.23}$$

While not necessary, it is sufficient that the equality on right-hand side of Eq. (4.23) is satisfied by demanding each term in both sums are equal, i.e.,

$$G^{(2\alpha)} = \left(\frac{\Omega}{4}\right)^\alpha L_\alpha^\alpha\left(\frac{\Omega}{4h^2}\right). \tag{4.24}$$

By substituting this definition of $G^{(2j)}$ into the alternative expression for the monochromatic frequency-domain phasor given in Eq. (22) of Ref. [67], we obtain

$$U_{BGV} = \frac{1}{2}(-1)^{n+m} \exp(ikz \pm im\phi) \mathrm{w}_0^{2n+m+2}$$

$$\times \sum_{\alpha=0}^{\infty} \left(\frac{1}{4k^2}\right)^{\alpha} \int_0^{\infty} k_{\perp}^{2n+m+1} e^{-p^2 k_{\perp}^2} \qquad (4.25)$$

$$\times k_{\perp}^{2\alpha} L_{\alpha}^{\alpha} \left(p^2 k_{\perp}^2\right) J_m(k_{\perp}\rho) \mathrm{d}k_{\perp},$$

in which we have set $p^2 = i(z - iz_R)/(2k) = [\mathrm{w}_0/(2h)]^2$. The integral in Eq. (4.25) can be evaluated via the result given in Eq. (B.6),

$$U_{BGV} = (-1)^{n+m} 2^{2n+m} \exp(ikz \pm im\phi)$$

$$\times h^{2n+m+2} v^{m/2} e^{-v} \sum_{\alpha=0}^{\infty} \left(\frac{h}{k\mathrm{w}_0}\right)^{2\alpha} \qquad (4.26)$$

$$\times \left[\sum_{i=0}^{\alpha} a_{\alpha,i}(n + \alpha + i)! L_{n+\alpha+i}^m(v)\right],$$

where the coefficients $a_{\alpha,i}$ are defined in Eq. (B.3). From Eq. (24) of Ref. [67], we have that

$$U_{BGV} = (-1)^{n+m} 2^{2n+m} \exp(ikz \pm im\phi)$$

$$\times h^{2n+m+2} v^{m/2} e^{-v} \sum_{\alpha=0}^{\infty} \left(\frac{h}{k\mathrm{w}_0}\right)^{2\alpha} \qquad (4.27)$$

$$\times \left[f_{n,m}^{(2\alpha)}\right].$$

Comparing Eqs. (4.26) & (4.27), and noting that the factors within the square brackets must be equal, we see that the general expression for the factors $f_{n,m}^{(2\alpha)}$ of Ref. [67] is

$$f_{n,m}^{(2\alpha)}(v) = \sum_{i=0}^{\alpha} a_{\alpha,i}(n + \alpha + i)! L_{n+\alpha+i}^m(v). \qquad (4.28)$$

Replacing the coefficients $a_{\alpha,i}$ by their definition in Eq. (B.3), the factors $f_{n,m}^{(2\alpha)}(v)$ are given explicitly as

$$f_{n,m}^{(2\alpha)}(v) = \sum_{i=0}^{\alpha} \frac{(-1)^i}{i!} \binom{2\alpha}{\alpha - i} (n + \alpha + i)! \, L_{n+\alpha+i}^m(v). \qquad (4.29)$$

Making the change of variable $i = \delta - \alpha$, and using the definition of $\kappa_{\alpha,\delta}$ given in Eq. (4.14), Eq. (4.29) can be rewritten as

$$f_{n,m}^{(2\alpha)}(v) = \sum_{\delta=\alpha}^{2\alpha} \kappa_{\alpha,\delta}(n+\delta)!\, L_{n+\delta}^{m}(v), \qquad (4.30)$$

thus making explicit the connection between the coefficients of $f^{(2\alpha)}$ and those of $\kappa_{\alpha,\delta}$.

4.4 Explicit derivation of the generalized time-domain phasor

In this section an explicit derivation of the generalized time-domain phasor up to arbitrary perturbative order α is provided, ultimately arriving at the expression given in Eq. (4.12). To this end, one starts with the monochromatic frequency-domain phasor of BGV, $U_{BGV}(\mathbf{r}, \omega)$, given in Eq. (4.1) [45, 67]. This phasor is then made polychromatic by multiplication with a Poisson-like frequency spectrum, $f(\omega)$, given in Eq. (2.5). Finally, a Fourier integral is performed to obtain the general time-domain phasor $U(\mathbf{r}, t)$. In what follows, we assume the condition of isodiffraction as described in Sec. 4.2.1

4.4.1 Generalization in the frequency domain

We define the polychromatic frequency-domain phasor as
$U^{(2\alpha)}(\mathbf{r}, \omega) \equiv f(\omega)U_{BGV}(\mathbf{r}, \omega)$, where $f(\omega)$ is given in Eq. (2.5) and U_{BGV} is given in Eq. (4.1). This expression is correct to order α in the perturbative small parameter ϵ^2, which, however, depends on the frequency ω. Before carrying out the Fourier transformation, we therefore replace all instances of ϵ^2 by the frequency-independent small parameter ϵ_c^2 defined in Eq. (3.6). Then, all frequency dependent terms can be contained in new perturbative terms $\overline{U}_{2\alpha}(\omega)$, namely,

$$U^{(2\alpha)}\left(\mathbf{r},\omega\right) = f(\omega)\left(U_{0,BGV} + \frac{\epsilon^2}{\beta}\,U_{2,BGV} + \cdots + \frac{\epsilon^{2\alpha}}{\beta^\alpha}\,U_{2\alpha,BGV}\right)$$
$$\equiv \overline{U}_0(\omega) + \frac{\epsilon_c^2}{\beta}\,\overline{U}_2(\omega) + \cdots + \frac{\epsilon_c^{2\alpha}}{\beta^\alpha}\,\overline{U}_{2\alpha}(\omega), \tag{4.31}$$

in which we have defined

$$\overline{U}_{2\alpha}(\omega) \equiv f(\omega)\frac{\omega_0^\alpha}{\omega^\alpha}\,U_{2\alpha,BGV}. \tag{4.32}$$

A term of arbitrary perturbative order from Eq. (4.32) can be written explicitly as

$$\overline{U}_{2\alpha}(\omega) = (-1)^{n+m}2^{2n+m}\exp(ikz + im\phi + i\phi_0)$$
$$\times \left(\frac{\omega_0}{\omega}\right)^\alpha\left(\frac{s}{\omega_0}\right)^{s+1}\frac{\omega^s\exp(-s\omega/\omega_0)}{\Gamma(s+1)}\Theta(\omega) \tag{4.33}$$
$$\times (2\pi)h^{2n+m+2}v^{m/2}\exp(-v)f_{n,m}^{(2\alpha)}(v).$$

Making use of Eqs. (4.30) and (4.14) (the generalizations of $f^{(2\alpha)}$ and $\kappa_{\alpha,\delta}$, respectively), and the definition of the associated Laguerre polynomial in Eq. (3.3), the frequency-dependence of the terms $f_{n,m}^{(2\alpha)}(v)$ in Eq. (4.33) can be shown explicitly as

$$f_{n,m}^{(2\alpha)}(v) = \sum_{\delta=\alpha}^{2\alpha}\kappa_{\alpha,\delta}(n+\delta)!L_{n+\delta}^m(v)$$
$$= \sum_{\delta=\alpha}^{2\alpha}\left[\kappa_{\alpha,\delta}(n+\delta)!\sum_{j=0}^{n+\delta}G_{(n+\delta),m,j}\xi^j\omega^j\right], \tag{4.34}$$

where constants defined in Eqs. (3.4) and (3.9a) have been used, and $\xi\omega = v$. Employing the definition of $\Lambda_{n,m}$ from Eq. (3.9c), as well as the vacuum dispersion relation $k = \omega/c$, we obtain the order α correction for the frequency-domain phasor in Eq. (4.33) as

$$\overline{U}_{2\alpha}(\omega) = \sqrt{2\pi}\,\frac{\Lambda_{n,m}}{n!}\exp\left(\frac{i\omega z}{c}\right)\left(\frac{s}{\omega_0}\right)^{s+1}\frac{\omega^s\exp(-s\omega/\omega_0)}{\Gamma(s+1)}\left(\frac{\omega_0}{\omega}\right)^\alpha\Theta(\omega)$$
$$\times \omega^{m/2}\exp(-\xi\omega)\sum_{\delta=\alpha}^{2\alpha}\left[\kappa_{\alpha,\delta}(n+\delta)!\sum_{j=0}^{n+\delta}G_{(n+\delta),m,j}\xi^j\omega^j\right]. \tag{4.35}$$

4.4.2 Generalization in the time domain

The time-domain representation of Eq. (4.35) is obtained through Fourier integration [see Eq. (3.7)]:

$$
\begin{aligned}
\overline{U}_{2\alpha}(t) &= \frac{1}{\sqrt{2\pi}} \int_{-\infty}^{\infty} e^{-i\omega t} \, \overline{U}_{2\alpha}(\omega) \, \mathrm{d}\omega \\
&= \frac{\omega_0^{\alpha} \Lambda_{n,m}}{n! \Gamma(s+1)} \left(\frac{s}{\omega_0}\right)^{s+1} \sum_{\delta=\alpha}^{2\alpha} \left[\kappa_{\alpha,\delta}(n+\delta)! \right. \\
&\quad \times \left. \sum_{j=0}^{n+\delta} G_{(n+\delta),m,j} \xi^j \int_0^{\infty} \omega^{\gamma-\alpha} \exp(-\eta\omega) \, \mathrm{d}\omega \right],
\end{aligned}
\tag{4.36}
$$

where $\eta \equiv -iz/c + \xi + s/\omega_0 + it$ and $\gamma \equiv s + m/2 + j$. The integral is evaluated using Eq. (2.21), yielding

$$
\begin{aligned}
\overline{U}_{2\alpha}(t) &= \frac{\omega_0^{\alpha} \Lambda_{n,m}}{n! \Gamma(s+1)} \left(\frac{s}{\omega_0}\right)^{s+1} \sum_{\delta=\alpha}^{2\alpha} \left[\kappa_{\alpha,\delta}(n+\delta)! \right. \\
&\quad \times \left. \sum_{j=0}^{n+\delta} G_{(n+\delta),m,j} \xi^j \Gamma(\gamma+1-\alpha) \eta^{-(\gamma+1-\alpha)} \right].
\end{aligned}
\tag{4.37}
$$

Moving all factors except $\Lambda_{n,m}$ into the inner sum, and making the substitutions indicated in Eqs. (4.13) and (4.7), the time-domain representation of the order α perturbative term $\overline{U}_{2\alpha}$ takes the form

$$
\overline{U}_{2\alpha}(t) = \Lambda_{n,m} \sum_{\delta=\alpha}^{2\alpha} \left[\sum_{j=0}^{n+\delta} c_{\alpha,\delta} \xi^j T^{-\gamma-1+\alpha} \right].
\tag{4.38}
$$

Corresponding to the *frequency-domain* phasor to order α in Eq. (4.31), the generalized *time-domain* phasor including all terms up to perturbative order Δ is

$$
\begin{aligned}
U^{(2\Delta)}(t) &= \sum_{\alpha=0}^{\Delta} \frac{\epsilon_c^{2\alpha}}{\beta^{\alpha}} \, \overline{U}_{2\alpha}(t) \\
&= \Lambda_{n,m} \sum_{\alpha=0}^{\Delta} \left[\frac{\epsilon_c^{2\alpha}}{\beta^{\alpha}} \sum_{\delta=\alpha}^{2\alpha} \left\{ \sum_{j=0}^{n+\delta} c_{\alpha,\delta} \xi^j T^{-\gamma-1+\alpha} \right\} \right],
\end{aligned}
\tag{4.39}
$$

which agrees exactly with Eq. (4.12), as predicted.

4.5   Summary

In this chapter we have derived an analytic expression, postulated in Eq. (4.12) and derived explicitly in Eq. (4.39), for the time-domain phasor presented in Chap. 3. This generalized time-domain phasor can be used to calculate the EM fields of an arbitrarily-tightly focused eLG beam of any LG mode and arbitrarily-short temporal duration. Our closed-form analytic result allows one to calculate the phasor to arbitrarily-high order Δ, in the perturbative small parameter ϵ_c^2, without having to evaluate any Fourier integrals. This model is thus straightforward to implement, either analytically or numerically.

An alternative method for deriving the factors $f_{n,m}^{(2\alpha)}(v)$ is outlined in Appendix A.2, where the series expansion method of BGV is followed explicitly. As discussed in Appendix A.2, there is a potential connection between that alternative method and the non-iterative derivation of integer partitions, which to our knowledge is an unsolved problem in the field of combinatorics in modern mathematics. Mathematicians or mathematical physicists may thus find this possible connection of significant interest.

Chapter 5

Electron Acceleration with Higher Order eLG Beams

5.1 Introduction

The production and control of particle beams is of central importance in modern physics. High quality electron beams with small temporal and angular confinement are required for ultrafast electron diffraction and microscopy [91], electron tomography [92], and free electron lasers [93] including utility as an x-ray source. Similarly, proton beams are currently used in particle colliders [94] and cancer treatment [95], for example.

In simulations studying vacuum acceleration schemes, electron beams are often produced by injecting a low density gas of highly-charged ions near the focus of an intense laser field [37, 96]. Here, the gas is often chosen such that the electrons, bound in the deep potential wells of the highly-charged ions, are ionized near the peak amplitude of the laser field. This results in a rapid acceleration of the electrons, which can achieve GeV energies with a driving intensity of some 10^{18} W/cm^2. Free electrons have also been used by many authors as the initial state to be accelerated, thus removing the need to perform calculations involving the ionization process (e.g., [97–99]). Vacuum

acceleration schemes such as these all require an initial density of ions (or free electrons) to be sufficiently low, roughly $10^{22}/m^3$, in order to ignore any plasma effects during acceleration [100].

However, various acceleration schemes that depend on these plasma effects have also been developed, such as plasma wakefield acceleration, laser wakefield acceleration, beat-wave acceleration, and self-modulated wakefield acceleration (cf. [101] and references therein). Here, electrons are trapped between fronts of the plasma waves through some particular mechanism, such as ionization or self-injection. These waves rapidly propagate through a plasma, dragging the electrons along to (often) GeV energies. Plasma acceleration has long been regarded as more practical than vacuum acceleration due to a higher possible electric field strength in the plasma as compared to that in many conventional laser systems [97], or a shorter acceleration distance being needed to produce electrons of similar energies (on the order of GeV/cm with a plasma density of $10^{18}/cm^3$).

Further, vacuum acceleration by laser fields is said to be impossible owing to the Lawson-Woodward theorem [102–104], which indicates that a free electron can't experience a net energy gain over one full period of interaction with such a wave; any energy imparted to an electron as a pulse overtakes it will be lost again as the pulse passes, owing to a reversal of the force direction. This does not occur with focused lasers since the intensity profile is not a constant in time, and thus vacuum acceleration by tightly focused beams becomes possible. Further, the Lawson-Woodward theorem neglects nonlinear effects such as the ponderomotive force [101], which in reality must be taken into account (especially for high-intensity fields).

Significant progress has recently been made in developing methods of vacuum acceleration that begin to bridge the gap between previous vacuum and plasma acceleration results. For instance, Vaziri studied the effects of driving acceleration from an electron gas with a vortex beam under the paraxial approximation. It was found that

GeV electron energies could be achieved with small angular distribution for certain initial conditions of the system [8]. Additionally, Varin found that by exploiting the strong longitudinal electric field of radially polarized $LG_{0,0}$ beams, free electrons could experience an on-axis acceleration gradient on the order of GeV per millimeter [105].

Acceleration with radially-polarized beams is attractive since the fields E_z have their maximum on-axis where E_ρ is zero [Fig. 5.1 (a)]. This allows axial electrons to be accelerated longitudinally with negligible transverse displacement. Electron ensembles that start near the beam waist center can thus be accelerated to high energies with a very small spatial and temporal distribution. One can see from Figs. 5.1 (b) & 5.1 (c) that as the radial LG mode increases above zero, the maximum strength of E_z relative to that of E_ρ increases dramatically.

As the radial LG index increases, a greater number of nodes enter the cross-sectional intensity profile of the beam (cf. Fig. 1.2 or Fig. 5.1). Therefore, for a beam of fixed energy, the intensity must become localized in increasingly smaller spatial regions as n is increased. Since the majority of the area under E_z is near the origin, this is where most of the energy will be located. This additional localized intensity near the axis should allow particles in that region to experience greater longitudinal forces during the acceleration process, and therefore achieve a higher final kinetic energy.

In this chapter, we present a vacuum acceleration scheme that expands on the results of Refs. [59, 105] by using a radially-polarized $LG_{n,0}$ beam with $n \neq 0$. Such beams achieve a higher peak longitudinal field intensity on axis than $LG_{0,0}$ beams, and thus are interesting to explore in the context of particle acceleration. In Section 5.2, the details of the numerical model implemented for electron acceleration are described. In Section 5.3, the results of these simulations are shown and analyzed for both single particle and ensemble cases.
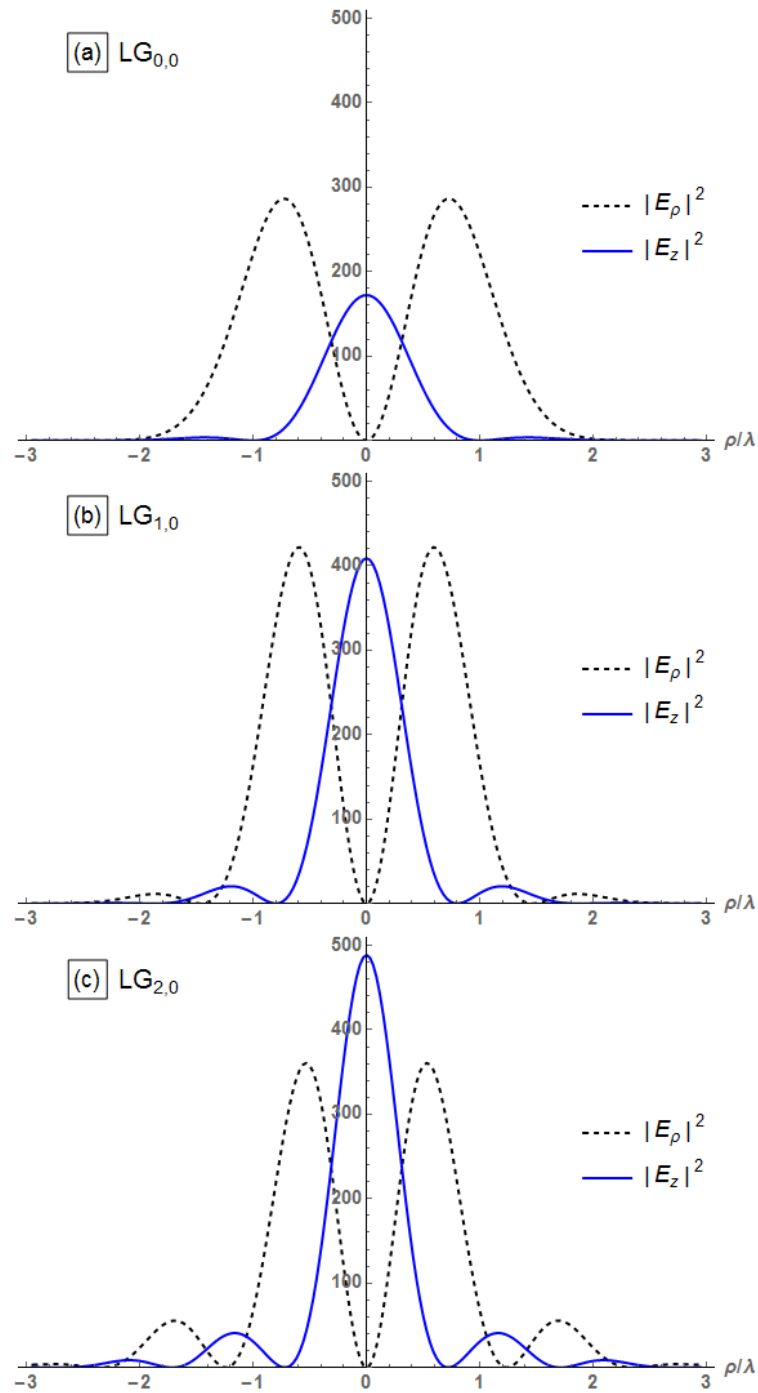
Figure 5.1: Absolute squares of the unnormalized radially-polarized fields E_ρ (black dashed) and E_z (solid blue) along a cross section at the beam waist for LG modes (a) $LG_{0,0}$, (b) $LG_{1,0}$, and (c) $LG_{2,0}$. The fields E_z have their maximum about $\rho = 0$ where E_ρ is minimal, allowing near-axis electrons to be accelerated longitudinally with negligible transverse force. As the radial LG mode increases, the maximum magnitude of E_z grows, allowing for greater electronic energy gains for beams of higher radial modes.

5.2 Numerical model

Using the perturbative field model introduced in Chapters 3 & 4 of this work, a Fortran code was developed to study the acceleration of free stationary electrons by a tightly-focused radially-polarized eLG beam. This perturbative description was chosen to expand on the results of Ref. [59] since generalizing LG modes of higher radial index in the time-domain using the exact model of Ref. [43] remains, to our knowledge, an open problem. An adaptive step size Bulirsch-Stoer algorithm [106] was then implemented to solve the relativistic classical equations of motion for an electron under the influence of the Lorentz force $\mathbf{F} = q(\mathbf{E} + \mathbf{v} \times \mathbf{B})$, where expressions for the unnormalized radially-polarized complex EM fields are given in Eqs. (3.20)-(3.24). These electrons were propagated to $120\,fs$, with the zero of time being set to coincide with the pulse center crossing $z = 0$.

Simulations were run for both 1) single particle trajectories and 2) acceleration of particle ensembles, each with $LG_{0,0}$, $LG_{1,0}$, and $LG_{2,0}$ beam geometries. As indicated in Fig. 3.1 (e), including perturbative terms up to ϵ_c^4 was sufficient for these calculations. In all cases the laser had central wavelength $\lambda_0 = 800\,nm$ and was focused to a beam waist of $w_0 = 785\,nm \approx 0.981\,\lambda_0$, thus requiring a nonparaxial description. The spectral parameter, presented in Eq. (2.5), was $s = 70$, resulting in a pulse with FWHM of about $8.370\,fs$, or about 3.136 cycles. Using a pulse energy of $2.5\,mJ$ resulted in a peak power of $P \approx 300\,GW$ with a peak intensity of $I = 1.543 \times 10^{19}\,W/cm^2$. These parameters were chosen to conform with the simulations of Marceau et al. [54].

Ensemble simulations were run with 500,000 electrons initially at rest and randomly distributed in a region $x_0 \in [-\lambda_0, \lambda_0]$, $z_0 \in [-3\lambda_0, 3\lambda_0]$, where z is the longitudinal coordinate and x, y are the transverse Cartesian coordinates. Owing to the azimuthal symmetry of $m = 0$ modes, $y_0 = 0$ was used to reduce computational load without impacting results. All particles which had final positions $z_f > 0$ were collected for analysis. For single particle trajectory simulations, the electrons were placed initially

at rest at the origin. In both cases, electrons which at any time step exceeded the boundaries of the perturbative radius of convergence defined in Sec. 3.6 were removed from the simulation.

Inter-electron Coulomb interactions were ignored in these simulations. At relativistic speeds approaching c, the electric repulsion in the transverse direction between two electrons is canceled by the respective magnetic attraction. Longitudinal spread, and therefore the temporal duration, of the produced electron bunches would be increased by including these effects. Still, Ref. [54] found good agreement in bunch durations accelerated by the Gaussian mode of a radially-polarized beam in the cases of 3D particle-in-cell simulations ($1.09fs$), and similar simulations in the single-particle limit ($0.73fs$).

Ideally, acceleration results would be fully optimized by a detailed numerical analysis of the parameter space which includes (but is not limited to) initial particle position and momentum, initial laser phase, time of ionization in the pulse, pulse energy, pulse duration, focal spot size, and wavelength, for every reasonable LG mode. However, this is a very large task computationally and has not been explored here fully. In the following section regarding acceleration results for both single particles and ensembles, only the initial phase of the laser was chosen by pseudo-optimization of ϕ_0 at each LG mode. With all other beam parameters held constant, the initial phase was varied over the eight cardinal and primary intercardinal phases for each of modes $LG_{0,0}$, $LG_{1,0}$, and $LG_{2,0}$. Of these results, the best for each LG mode was selected for analysis ("best" was taken to mean the largest energy gain for single particles, and highest axial electron density with largest average kinetic energy for ensembles).

5.3   Results and discussion

5.3.1   Single-particle acceleration trajectories

To illustrate the potential for using higher-order radial LG modes to enhance energy gain during electron acceleration, simulations were run in which single particles starting at the origin were accelerated by $LG_{0,0}$, $LG_{1,0}$, and $LG_{2,0}$ beams. These results are shown in Fig. 5.2. Hu and Starace [96] had previously found that for the Gaussian mode, final electron energy was enhanced by ionizing the electron near the peak of the driving pulse. To check if these results held at higher radial modes, simulations were run both in the cases of free electrons at rest [5.2 (a)] and electrons assumed to be initially tightly-bound, and therefore accelerated starting at the pulse center [5.2 (b)] ("ionized" at the peak of the pulse).

For each of these simulations, the overall phase, ϕ_0, of the laser field displayed was chosen such that the electron had the largest final kinetic energy. For the case of free electrons [5.2 (a)] these values correspond to $\phi_0 = \pi/2$, $\phi_0 = 3\pi/4$, and $\phi_0 = 7\pi/4$ for the $n = 0$, $n = 1$, and $n = 2$ trajectories, respectfully. For the case of tightly-bound electrons [5.2 (b)] these values correspond to $\phi_0 = 3\pi/2$, $\phi_0 = \pi/2$, and $\phi_0 = 3\pi/2$ for the $n = 0$, $n = 1$, and $n = 2$ trajectories, respectfully.

For all three LG modes simulated, total energy gain was confirmed to be enhanced by assuming ionization at the peak intensity of the driving laser field. Additionally, the electron accelerated by the $LG_{0,0}$ mode did not achieve the maximum energy in either of the free or bound electron cases. However, since the acceleration dynamics are extremely sensitive to initial laser phase and particle location, these results are not particularly illustrative beyond showing the possibility for increased energy gain at higher LG modes. For a more comprehensive result, the next section examines acceleration of a pseudo-randomly placed initial ensemble of particles.
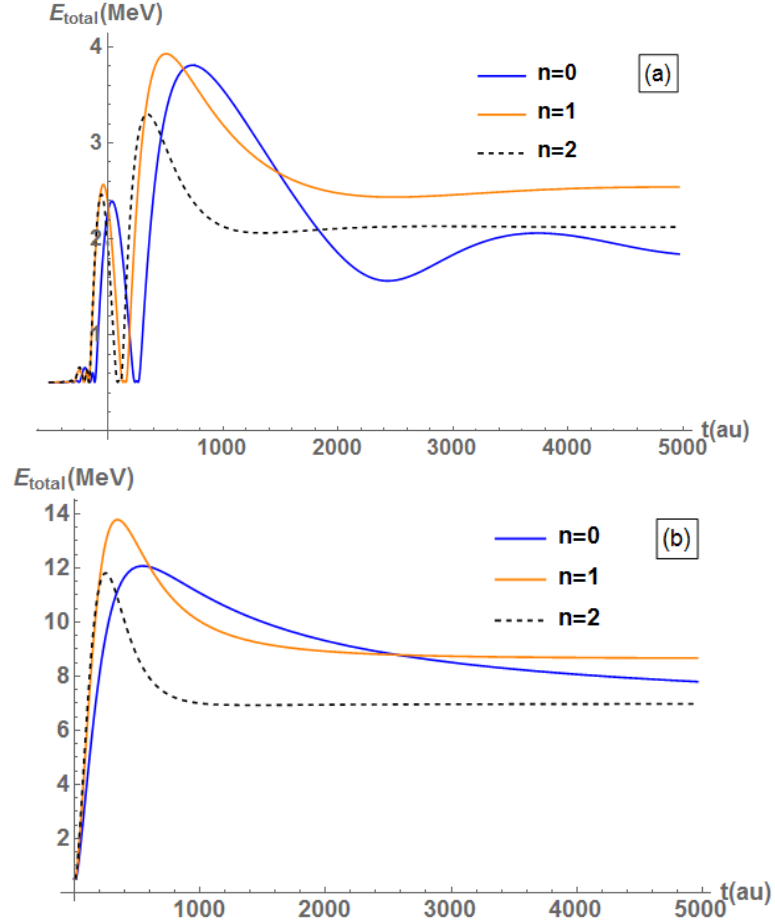
Figure 5.2: Energy along trajectories for an electron initially at rest at the origin acceler-ated by $LG_{0,0}$ (solid dark blue), $LG_{1,0}$ (solid light orange), and $LG_{2,0}$ (dashed black) beams. Results are shown for cases of both (a) interaction with the entire pulse, and (b) assumed ionization at the pulse peak [$t = 0$]. In either case, the $LG_{0,0}$ electron does not have the highest post-acceleration energy. Note that "au" denotes atomic units.

5.3.2 Ensemble acceleration results

In Fig. 5.3, results for ensemble accelerations by lasers of the first three radial LG modes are shown. To generate these plots, ensemble simulations were run for the eight cardinal and primary intercardinal phases for each of the modes $LG_{0,0}$, $LG_{1,0}$, and $LG_{2,0}$. For each LG mode, the eight resulting electron distributions were analyzed numerically to determine which initial phase produced the best electron bunch, determined by locating axial regions of highest electron density in windows of length $3\lambda_0$ ($\approx 8fs$) along the z-axis and width $2\lambda_0$ centered about $x = 0$. Electrons outside this window were filtered

out of the shown results, which could be achieved experimentally by passing the unfiltered beam through an annular hole (x-filtering) and selecting only electrons within a certain energy range (z-filtering).

For the modes $LG_{0,0}$, $LG_{1,0}$, and $LG_{2,0}$, the best final electron bunches were identified in the cases of initial laser phases $\phi_0 = 3\pi/2$, $\phi_0 = 3\pi/4$, and $\phi_0 = 0$, respectively. In each panel of Fig. 5.3, the vertical dashed lines mark the ensemble average longitudinal position. Since all simulations were run out to a final time of $120 fs$, this position is related to the average kinetic energy of the electron bunch. Unlike the results in the single-particle case, the ensemble average kinetic energy decreases at each higher radial mode. This can be seen from the lower ensemble average z positions, decreasing from $36.98\lambda_0$ at $n = 0$ to $34.79\lambda_0$ at $n = 1$, and finally $31.49\lambda_0$ at $n = 2$. Further, final total charge of these electron bunches decreased at higher LG modes, dropping from $1.45 fC$ at $n = 0$ to $0.64 fC$ at $n = 1$ and finally $0.55 fC$ at $n = 2$.

For the $LG_{0,0}$ mode, Ref. [54] reported $1.1 fC$ electron pulses with durations of roughly $1 fs$ and final average positions between $34\lambda_0$ and $35\lambda_0$ for a similar acceleration scheme. Since the results of that work were generated using the exact phasor model of Ref. [43], which is described by different boundary conditions than the perturbative model used in this work, one would not expect exact agreement. Further, Ref. [54] noted that full ionization dynamics play a central role in determining the properties of the accelerated electrons, as their results for electrons initially bound in Hydrogen and Helium showed very different structures in the final electron distributions.

To our knowledge, no ensemble vacuum acceleration simulations have been published which use higher order radial LG modes. As such, the remainder of this section is dedicated to explaining the degradation in produced electron beam quality as the radial mode is increased. To begin, one considers the regions of initial electron density (x_0, z_0) which contribute to the final electron ensembles. This region of viable initial positions shrinks as the radial index is raised (Fig. 5.4), due in part to the increased
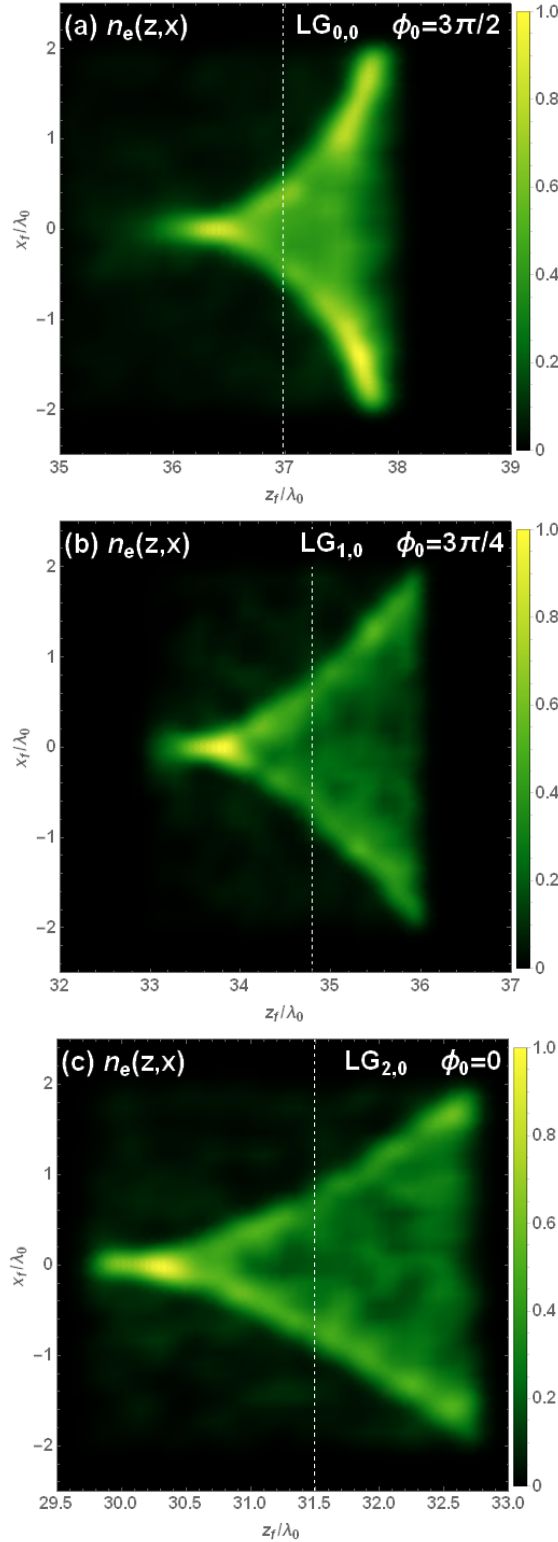
Figure 5.3: Normalized electron density maps for the final ensembles of electrons generated from acceleration by (a) $LG_{0,0}$, (b) $LG_{1,0}$, or (c) $LG_{2,0}$ beams. The shown region represents a filtered selection of all accelerated electrons, for which initial phases of the driving laser were chosen to maximize bunch charge and kinetic energy while minimizing angular and temporal distributions. The dashed white line denotes the ensemble average position.

intensity of E_ρ away from the beam waist (Fig. 5.5).

Figure 5.4 shows the initial positions of electrons which remain in the ensembles post-acceleration for the cases of unfiltered (yellow) and filtered (red) electrons. Unfiltered electrons are those which stay within the perturbative radius of convergence and have final position $z > 0$, which is further reduced to the filtered set based on bunch quality as described previously. For unfiltered electrons (yellow), the region of initial distribution that survives to $120\,fs$ significantly decreases as the radial LG mode increases. In agreement with the results of Marceau et al. [54], the filtered electrons (red) from acceleration by the Gaussian mode come primarily from a region $2 \lesssim z/\lambda_0 \lesssim 3$ and $|x/\lambda_0| \lesssim 0.75$. At higher order modes, the primary band of such electrons near $z \approx 3$ is noticeably smaller than for the Gaussian mode.

One reason for this reduction in ensemble retention is illustrated in Fig. 5.5. While Fig. 5.1 showed E_z dominating E_ρ in magnitude at $z = 0$, Fig. 5.5 shows that as one looks away from the beam waist this dominance does not persist. In particular, the results of Fig. 5.4 show that ideal electrons are almost exclusively being born into the continuum near $z = 3\lambda_0$ for higher modes, at which point the fields E_ρ have greater magnitudes than E_z (as shown in Fig. 5.5). This allows for transverse forces to dominate interactions with many more electrons at higher radial modes, pushing them outside of the perturbative radius of convergence. For the $n = 0$, $n = 1$, and $n = 2$ modes, 42.39%, 51.31%, and 61.95%, respectively, of the initial distribution was removed from the simulation for exceeding the boundaries of the perturbative radius of convergence. Even if such electrons were not immediately removed from the simulation, they would achieve transverse coordinates too large to contribute to the selected axial electron bunches.

In addition to the overall magnitudes of the fields E_ρ and E_z, it is essential to consider their phases across the region of initial electron distribution. The ideal case for electron acceleration is one in which the field E_z is negative while the field E_ρ simultaneously is positive. This allows the electron to be pushed in the direction of the
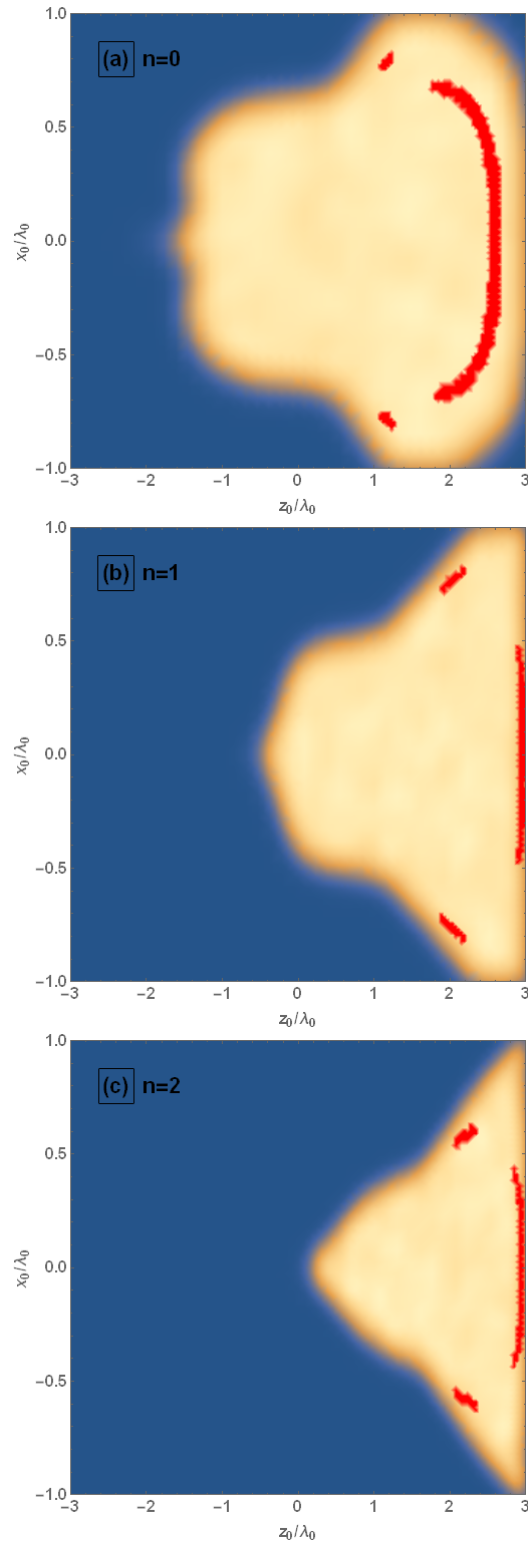
Figure 5.4: Initial positions of electrons captured in total (yellow) and post-filtering (red) are shown for the cases of ensemble acceleration by (a) $LG_{0,0}$, (b) $LG_{1,0}$, and (c) $LG_{2,0}$ beams. For both filtered and unfiltered results, as the radial index increases there are fewer initial positions from which accelerated electrons remain in the ensemble.

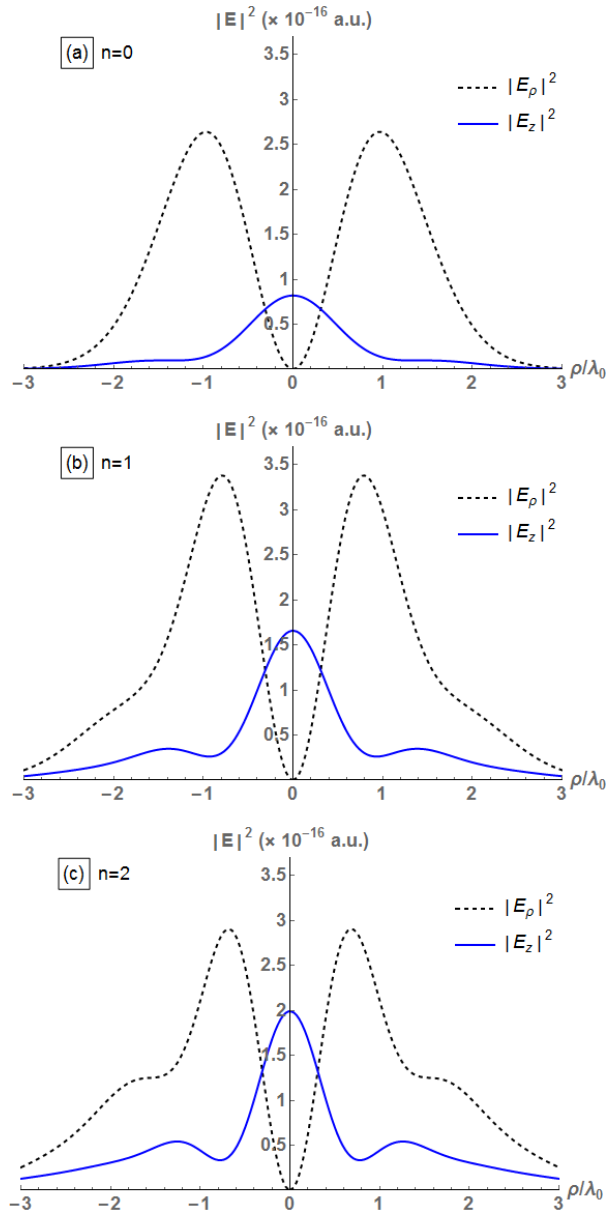Figure 5.5: Unnormalized field intensities at $z = 3\lambda_0$ for (a) $LG_{0,0}$, (b) $LG_{1,0}$, and (c) $LG_{2,0}$ beams. Unlike at the beam waist (Fig. 5.1), the maximum value of $|E_z|^2$ is not greater than the maximum of $|E_\rho|^2$ for any radial mode at $z = 3\lambda_0$. Electrons which are assumed to be ionized at such points are more vulnerable to transverse acceleration by E_ρ.

beam's propagation while also being pulled towards the optical axis, where E_z is larger and E_ρ is smaller. Figure 5.6, Fig. 5.7, and Fig. 5.8 analyze these phase properties for the cases of $LG_{0,0}$, $LG_{1,0}$, and $LG_{2,0}$ modes, respectively.

In each of these figures, panels (a) show histograms of the initial positions of the electrons retained post-filtering. The blue histograms represent the initial z_0 distribution while the red histograms represent the initial x_0 distribution. As expected, the transverse distribution is roughly symmetric across $x = 0$ due to the azimuthal symmetry of $m = 0$ modes. In the longitudinal direction, there is no symmetry and only one region of relevant initial density. The locations of these initial bin maxima for x_0 and z_0 are labeled on each of the (a) panels.

Having located the optimal initial positions for these electrons, panels (b) of Fig. 5.6 through Fig. 5.8 examine the phases of the fields E_z and E_ρ in the vicinity of these points $(z_{0,max}, x_{0,max})$ at the time of ionization. One notices immediately that the ideal conditions for electron acceleration ($E_z < 0$ and $E_\rho > 0$) are not simultaneously held at the points of optimal ionization, denoted by the crossing of the yellow grid lines in Fig. 5.6 through Fig. 5.8, for any LG modes. In fact, all LG modes exhibit the same profile at these optimal points, namely that $E_z < 0$ and $E_\rho < 0$ with $|E_z| < |E_\rho|$. However, in all three cases, the ideal electron encounters a field configuration in which these ideal conditions are satisfied almost immediately after ionization, as is explored in the following paragraph.

The reason that these phases at the points of ionization constitute ideal initial conditions is made clear in panels (c) of Fig. 5.6 through Fig. 5.8, which show the normalized fields E_z and E_ρ along the trajectory of an electron which was ionized at these optimal locations. For all three LG modes, the fields E_ρ almost immediately became large and positive along the trajectory, drawing the electrons towards the axis where they are accelerated forwards by a strongly negative E_z. These electrons surf along the wavefront under such ideal acceleration conditions for about $24.37\ as$, $15.01\ as$, and

Figure 5.6: For the $LG_{0,0}$ mode with initial phase $\phi_0 = 3\pi/2$, (a) histograms of starting positions z_0 and x_0 of the final bunched electrons, (b) phases of the real fields E_ρ (red) and E_z (blue) about the maximum of z_0 bins, and (c) normalized fields E_ρ (red) and E_z (blue) along the trajectory of a single electron starting at the position indicated by the maximum of z_0 and x_0 bins. In (b) the opaque black plane denotes $|E| = 0$ and the yellow gridlines denote the most populated x_0 and z_0 bin positions. Note that "au" denotes atomic units.
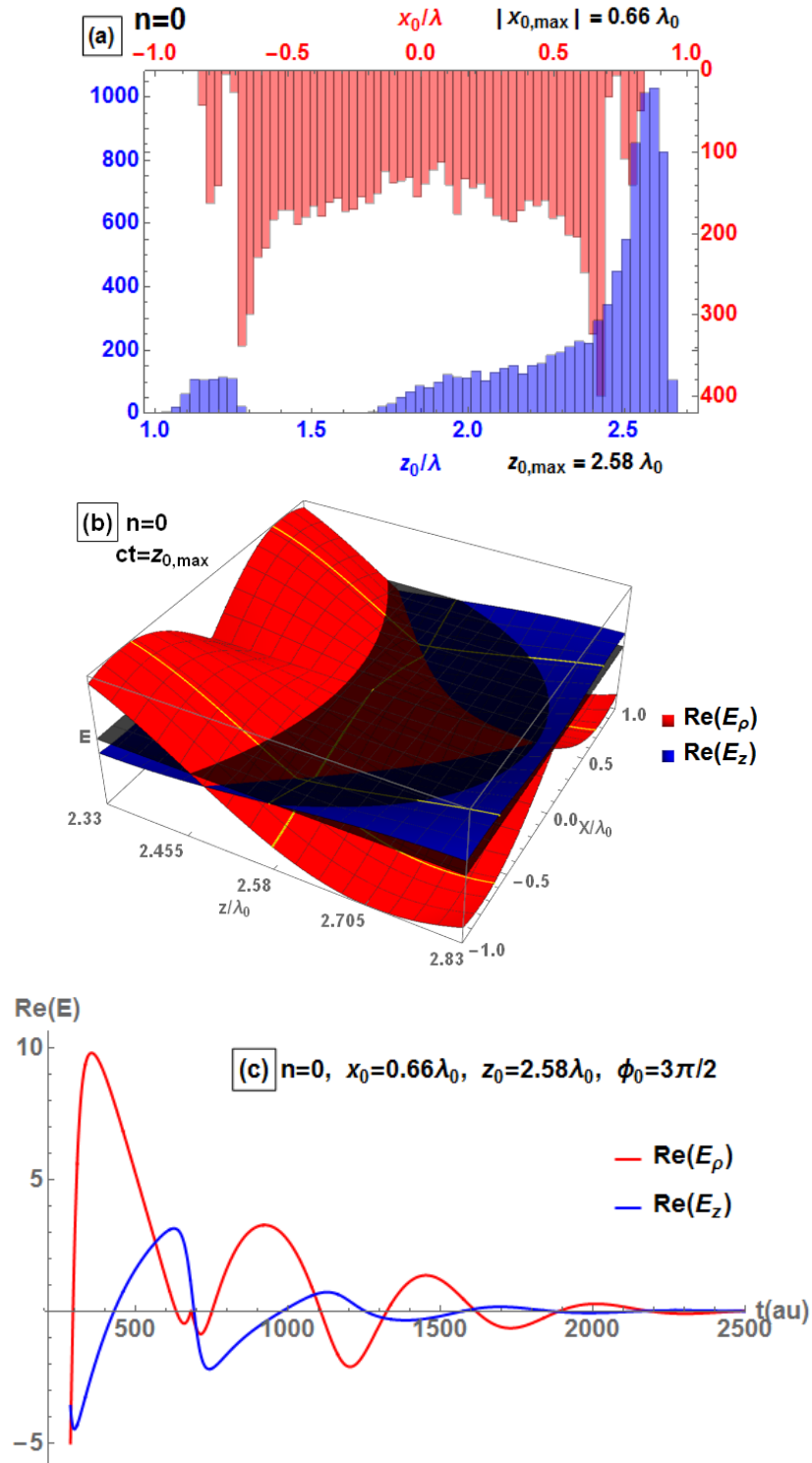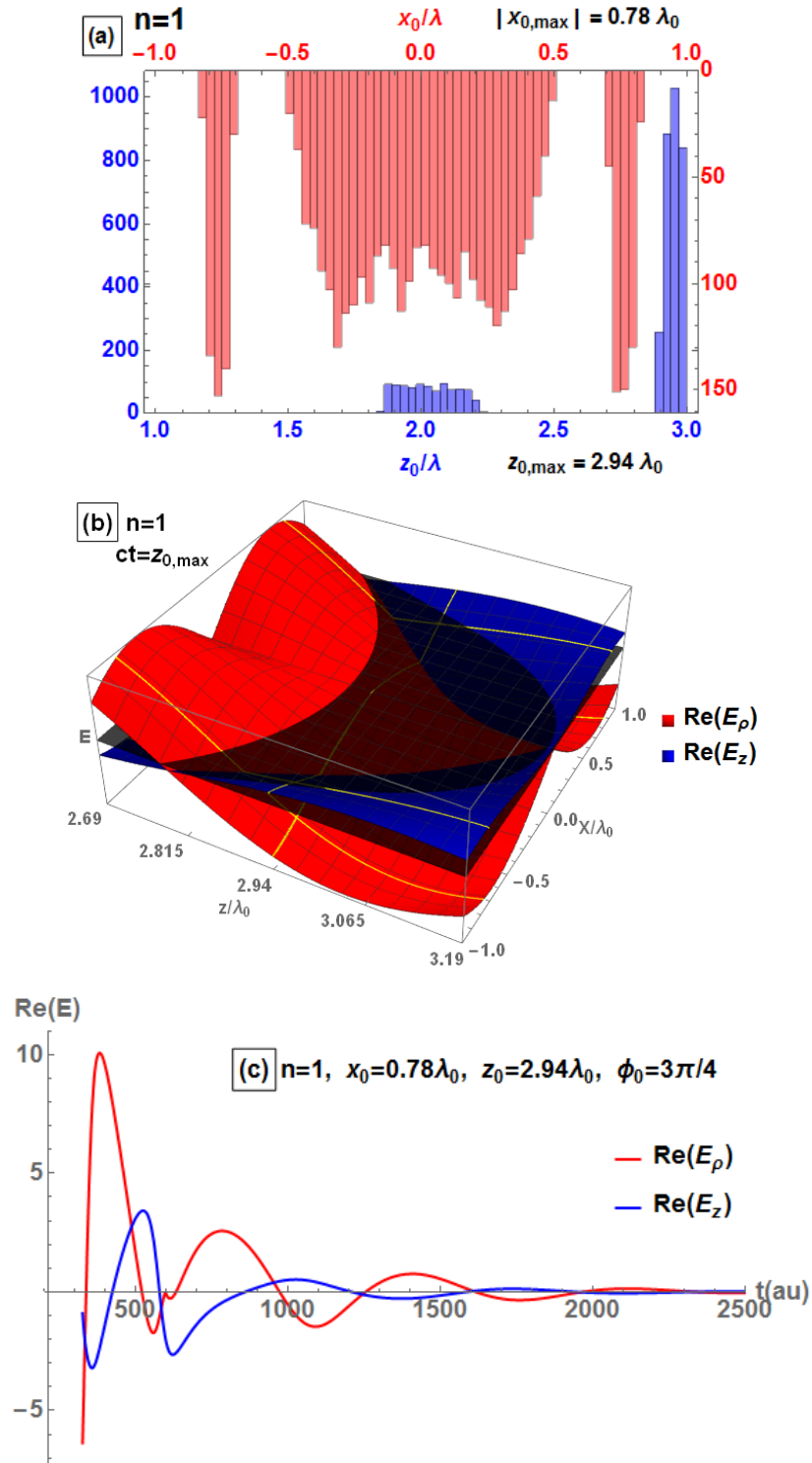
Figure 5.7: For the $LG_{1,0}$ mode with initial phase $\phi_0 = 3\pi/4$, (a) histograms of starting positions z_0 and x_0 of the final bunched electrons, (b) phases of the real fields E_ρ (red) and E_z (blue) about the maximum of z_0 bins, and (c) normalized fields E_ρ (red) and E_z (blue) along the trajectory of a single electron starting at the position indicated by the maximum of z_0 and x_0 bins. In (b) the opaque black plane denotes $|E| = 0$ and the yellow gridlines denote the most populated x_0 and z_0 bin positions. Note that "au" denotes atomic units.
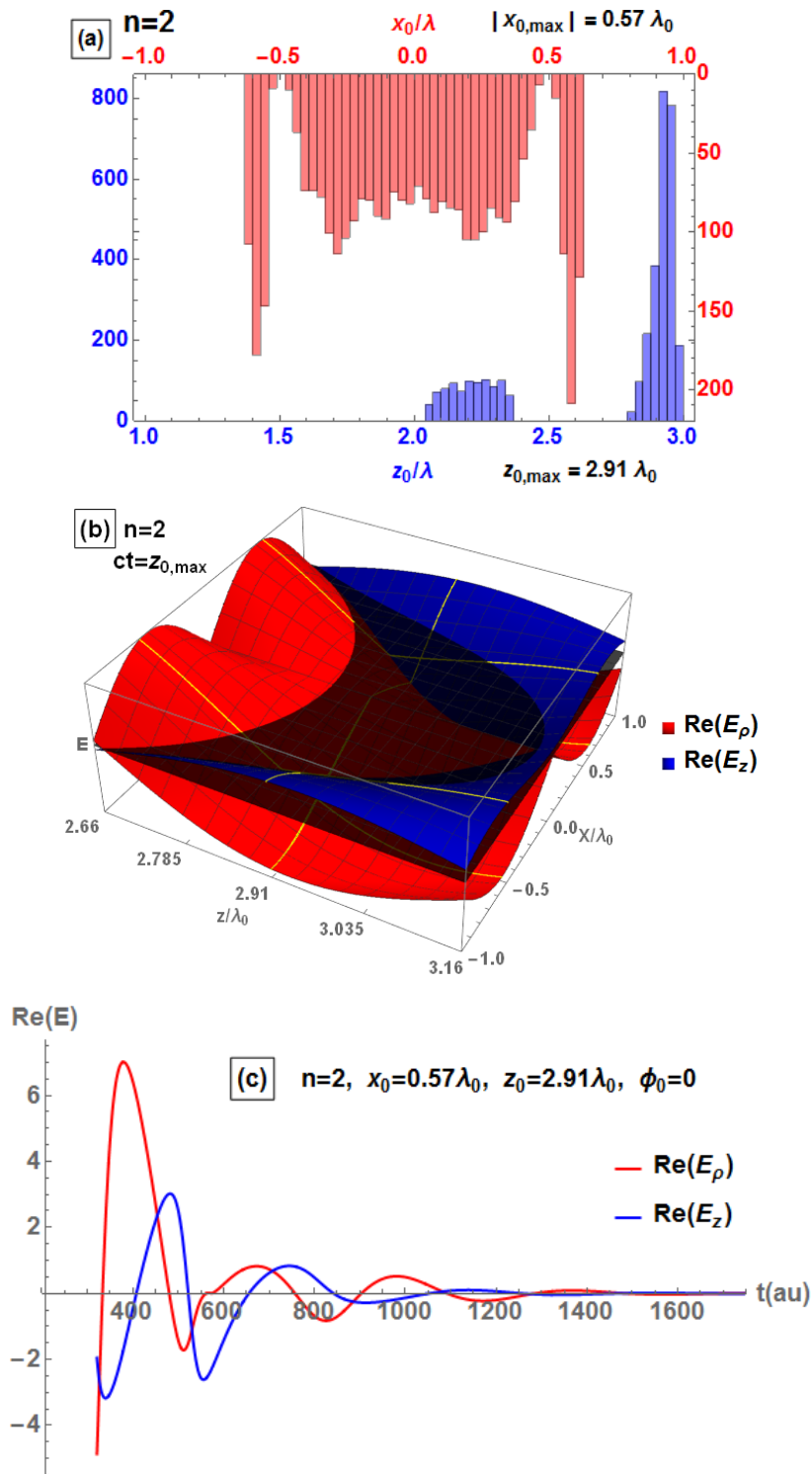
Figure 5.8: For the $LG_{2,0}$ mode with initial phase $\phi_0 = 0$, (a) histograms of starting positions z_0 and x_0 of the final bunched electrons, (b) phases of the real fields E_ρ (red) and E_z (blue) about the maximum of z_0 bins, and (c) normalized fields E_ρ (red) and E_z (blue) along the trajectory of a single electron starting at the position indicated by the maximum of z_0 and x_0 bins. In (b) the opaque black plane denotes $|E| = 0$ and the yellow gridlines denote the most populated x_0 and z_0 bin positions. Note that "au" denotes atomic units.

$13.42\ as$ for the cases of $n = 0$, $n = 1$, and $n = 2$, respectively. It is during these intervals that the most significant portion of the acceleration occurs. It is thus clear why ensemble average kinetic energies are reduced when the radial LG index is increased as shown in Fig. 5.4; the field geometries at higher radial indices lead to a shorter temporal window in which optimally-positioned electrons can be accelerated by fields of optimal phase combination.

The region of initial positions which produce well-columnated high-energy electrons could possibly be increased in size by further optimization of the full parameter space, including, perhaps, using nonzero OAM beams. Results might also be improved by the application of an external magnetic field to assist in the acceleration process. Reference [107] reported up to 70% increased energy gain in the case of acceleration by a radially-polarized Gaussian pulse in the presence of an external magnetic field. Further, it may be possible to combine multiple driving laser fields in the same spatiotemporal region such that ideal acceleration phases exist for longer periods of a trajectory and over a larger region of the initial particle distribution. In short, there remains much to explore in the full optimization problem for vacuum acceleration.

Appendix A

BGV's Calculation of the Factors $f^{(2j)}(v)$

A.1 Calculation by Series Expansion

We begin with the frequency-domain phasor, for any LG mode, of BGV in integral form (Eq. (16) of Ref. [67]),

$$
\begin{aligned}
U_{n,m} = \int_0^\infty &(-\alpha)^{2n+m}(-1)^n \exp(\pm im\phi)\mathrm{w}_0^{2n+m} \\
&\times \left[\frac{z_R}{k_z}\exp\left(ik_z(z-iz_R)-kz_R\right)\right] \\
&\times J_m(\alpha\rho)\alpha\,d\alpha,
\end{aligned}
\tag{A.1}
$$

where $\alpha \equiv k_\perp$ and $k^2 = k_\perp^2 + k_z^2$. An intermediate result of Ref. [67] is that the phasor of Eq. (A.1) above is equivalent to an infinite series representation given by Eq.(22) of Ref. [67],

$$
\begin{aligned}
U_{n,m} = \int_0^\infty &(-\alpha)^{2n+m}(-1)^n \exp(\pm im\phi)\mathrm{w}_0^{2n+m} \\
&\times \left[\frac{\mathrm{w}_0^2}{2}\exp(ikz)\exp\left(-\frac{i\alpha^2}{2k}(z-iz_R)\right)\right. \\
&\left.\sum_{j=0}^\infty \frac{G^{(2j)}}{(k\mathrm{w}_0)^{(2j)}}\right] J_m(\alpha\rho)\alpha\,d\alpha.
\end{aligned}
\tag{A.2}
$$

Comparing these two equations, it is clear that the terms inside the square brackets

of each expression must be equal. Making use of the relation $z_R = k\mathrm{w}_0^2/2$ and our previous definition of h from Eq. (3.1), and defining $\Omega \equiv \mathrm{w}_0^2 k_\perp^2$, the terms in square brackets of Eqs. (A.1) and (A.2) can be equated and solved for the infinite sum, yielding

$$\sum_{j=0}^{\infty} \epsilon^{(2j)} G^{(2j)} = \frac{1}{\sqrt{1 - \epsilon^2 \Omega}} \exp\left(\frac{\sqrt{1 - \epsilon^2 \Omega} - 1}{2\epsilon^2 h^2} + \frac{\Omega}{4h^2}\right) \tag{A.3}$$

In the above expression, we again define $\epsilon \equiv 1/(k\mathrm{w}_0)$ since the description at this point is monochromatic. The RHS can then be expanded in a Taylor series about $\epsilon^2 = 0$. Collecting powers of ϵ^2 in this expansion yields the perturbative terms $G^{(2j)}$,

$$\sum_{j=0}^{\infty} \epsilon^{(2j)} G^{(2j)} = O\left(\epsilon^8\right) + 1 + \epsilon^2 \left(\frac{\Omega}{2} - \frac{\Omega^2}{16h^2}\right) + \epsilon^4 \left(\frac{3\Omega^2}{8} - \frac{\Omega^3}{16h^2} + \frac{\Omega^4}{512h^4}\right)$$
$$+ \epsilon^6 \left(\frac{5\Omega^3}{16} - \frac{15\Omega^4}{256h^2} + \frac{3\Omega^5}{1024h^4} - \frac{\Omega^6}{24576h^6}\right). \tag{A.4}$$

These results confirm Eq. (23) of Ref. [67], and elucidate how to extend the method to arbitrarily large j. These terms $G^{(2j)}$ are then used in Eq. (A.2) along with the integral

$$\int_0^{\infty} \alpha^{2n+m} \exp\left(-p^2 \alpha^2\right) J_m(\alpha\rho)\alpha \, \mathrm{d}\alpha$$
$$= \frac{n!}{2} p^{-(2n+m+2)} \left(\frac{\rho}{2p}\right)^m L_n^m \left(\frac{\rho^2}{4p^2}\right) \exp\left(-\frac{\rho^2}{4p^2}\right) \tag{A.5}$$

to produce the factors $f^{(2j)}(v)$ given by BGV in Ref. [67].

A.2 Limitations of the Series Approach

In Ref. [67], the factors $f^{(2j)}(v)$ were originally calculated one at a time from each term in $G^{(2j)}$, which we introduced in Eq. (A.3). To calculate $G^{(2j)}$ for a particular j, one carries out a Taylor series expansion of the right-hand side of Eq. (A.3) about $\epsilon^2 = 0$, the first terms of which are given in Eq. (A.4). As one clearly sees, calculation of an arbitrary-high

order term in this expansion is not simple. Referring to the right-hand side of Eq. (A.3) as $\mathfrak{F}$, by the product rule for differentiation, each ϵ^2 derivative acting on $\mathfrak{F}$ must act on both the prefactor and the exponential. The action of arbitrarily many such derivatives takes the form

$$\frac{d^j \mathfrak{F}}{d\epsilon^{2j}} = \sum_{i=0}^{j} \left\{ \left[\frac{\Omega^i}{(1 - \epsilon^2 \Omega)^{(1+2i)/2}} \prod_{i'=1}^{i} \left(\frac{2i'-1}{2} \right) \right] \times \left[\frac{d^{j-i}}{d\epsilon^{2(j-i)}} e^{\mathfrak{E}} \right] \binom{j}{i} \right\}, \tag{A.6}$$

where the first set of square brackets represents derivatives of the prefactor, the argument of the exponential in Eq. (A.3) is denoted by $\mathfrak{E} \equiv (\sqrt{1 - \epsilon^2 \Omega} - 1)/(2\epsilon^2 h^2) + \Omega/(4h^2)$, and the binomial coefficients occur owing to the product rule.

To evaluate the second set of square brackets in Eq. (A.6), one requires an expression for arbitrarily many derivatives of an exponential function. This result can be found via Faà di Bruno's formula, which represents arbitrarily many derivatives of a composition of sufficiently differentiable functions [108, 109]. Faà di Bruno's formula, however, involves a sum over all possible integer partitions of the derivative order (cf. § 24.2.1 of Ref. [88]). Integer partitions are still an area of active research in combinatorics, and while there exist formulas for the *number* of partitions of an arbitrary integer there is, to our knowledge, presently no known analytical representation for the partitions themselves. As such, the partitions of a given integer are often generated through iterative algorithmic approaches [110, 111] (e.g requiring knowledge of the partitions of q to calculate those of $q + 1$). This prevents one from writing a non-recursive expression for the derivatives in Eq. (A.6), and therefore from obtaining analytically a general solution for the coefficients of $f^{(2j)}(v)$ for arbitrary order j.

It remains an open question how this alternative method for deriving the factors $f^{(2j)}$, which requires knowledge of integer partitions, could be related to the

generalization presented in Ch. 4. The potential for discovering an analytical representation for the partitions of any integer is an exciting prospect, and researchers in combinatorics or mathematical physics may thus find this connection of interest.

Appendix B

Result for the Integral in Eq. (4.25)

In this appendix, we derive the result for the integral of a particular product of an associated Laguerre polynomial and a Bessel function that appears in Eq. (4.25). We start with the integral in Eq. (8) of Ref. [67]:

$$
\begin{aligned}
&\int_0^\infty k_\perp^{2n+m} e^{-p^2 k_\perp^2} J_m(k_\perp \rho)\, k_\perp\, \mathrm{d}k_\perp \\
&= \frac{n!}{2} p^{-(2n+m+2)} \left(\frac{\rho}{2p}\right)^m L_n^m\left(\frac{\rho^2}{4p^2}\right) \exp\left(-\frac{\rho^2}{4p^2}\right).
\end{aligned}
\tag{B.1}
$$

We define now a similar integral,

$$
I_{n,m}^{(2\alpha)}(\rho,p) \equiv \int_0^\infty k_\perp^{2n+m+1} e^{-p^2 k_\perp^2} k_\perp^{2\alpha} L_\alpha^\alpha\left(p^2 k_\perp^2\right) J_m(k_\perp \rho) \mathrm{d}k_\perp,
\tag{B.2}
$$

The series representation of the associated Laguerre polynomials is given by Eq. (8.970.1) of Ref. [90]:

$$
L_\alpha^\alpha(x) = \sum_{i=0}^\alpha \frac{(-1)^i}{i!} \binom{2\alpha}{\alpha-i} x^i \equiv \sum_{i=0}^\alpha a_{\alpha,i}\, x^i.
\tag{B.3}
$$

Substituting Eq. (B.3) into Eq. (B.2), we obtain

$$I_{n,m}^{(2\alpha)}(\rho, p) = \int_0^\infty k_\perp^\theta e^{-p^2 k_\perp^2} k_\perp^{2\alpha} J_m(k_\perp \rho) \sum_{i=0}^\alpha a_{\alpha,i} p^{2i} k_\perp^{2i} \mathrm{d}k_\perp$$

$$= \sum_{i=0}^\alpha a_{\alpha,i} p^{2i} \int_0^\infty k_\perp^{2n+m+1+2\alpha+2i} e^{-p^2 k_\perp^2} J_m(k_\perp \rho) \mathrm{d}k_\perp. \tag{B.4}$$

This integral can be solved directly by application of Eq. (B.1) with the replacement $n \to (n + \alpha + i)$:

$$I_{n,m}^{(2\alpha)} = \sum_{i=0}^\alpha a_{\alpha,i} \left[\frac{(n+\alpha+i)!}{2} p^{-(2n+m+2\alpha+2)} \left(\frac{\rho}{2p} \right)^m L_{n+\alpha+i}^m \left(\frac{\rho^2}{4p^2} \right) \exp \left(-\frac{\rho^2}{4p^2} \right) \right]$$

$$= \frac{1}{2} \left(\frac{\rho}{2p} \right)^m \exp \left(-\frac{\rho^2}{4p^2} \right) p^{-(2n+m+2\alpha+2)} \sum_{i=0}^\alpha a_{\alpha,i}(n+\alpha+i)! L_{n+\alpha+i}^m \left(\frac{\rho^2}{4p^2} \right). \tag{B.5}$$

Using the definitions $p = \mathrm{w}_0/(2h)$ [see text below Eq. (4.25)] and $v = h^2 \rho^2 / \mathrm{w}_0^2$ [see text below Eq. (4.1)], we can write $v = \rho^2/(4p^2)$. Rewriting Eq. (B.5) in terms of v and using $p = \mathrm{w}_0/(2h)$, we obtain the following result for the integral defined in Eq. (B.2):

$$I_{n,m}^{(2\alpha)} = \int_0^\infty k_\perp^{2n+m+1} e^{-p^2 k_\perp^2} k_\perp^{2\alpha} L_\alpha^\alpha \left(p^2 k_\perp^2 \right) J_m(k_\perp \rho) \mathrm{d}k_\perp$$

$$= \frac{1}{2} v^{m/2} e^{-v} \left(\frac{2h}{\mathrm{w}_0} \right)^{2n+m+2\alpha+2} \sum_{i=0}^j \left[a_{\alpha,i}(n+\alpha+i)! \, L_{n+\alpha+i}^m(v) \right], \tag{B.6}$$

where the coefficients $a_{\alpha,i}$ are defined in Eq. (B.3).

Appendix C

Fortran and Python Implementations of the Perturbative Model

Fortran code for calculating the perturbative time-domain EM fields can be found on my github page at the following URL. This code was used for all electron acceleration results presented in this work.

https://github.com/avikarto/accelerationCode

Additionally, Python code for calculating the generalized perturbative time-domain phasor can be found on my github page at the following URL:

https://github.com/avikarto/pertFields
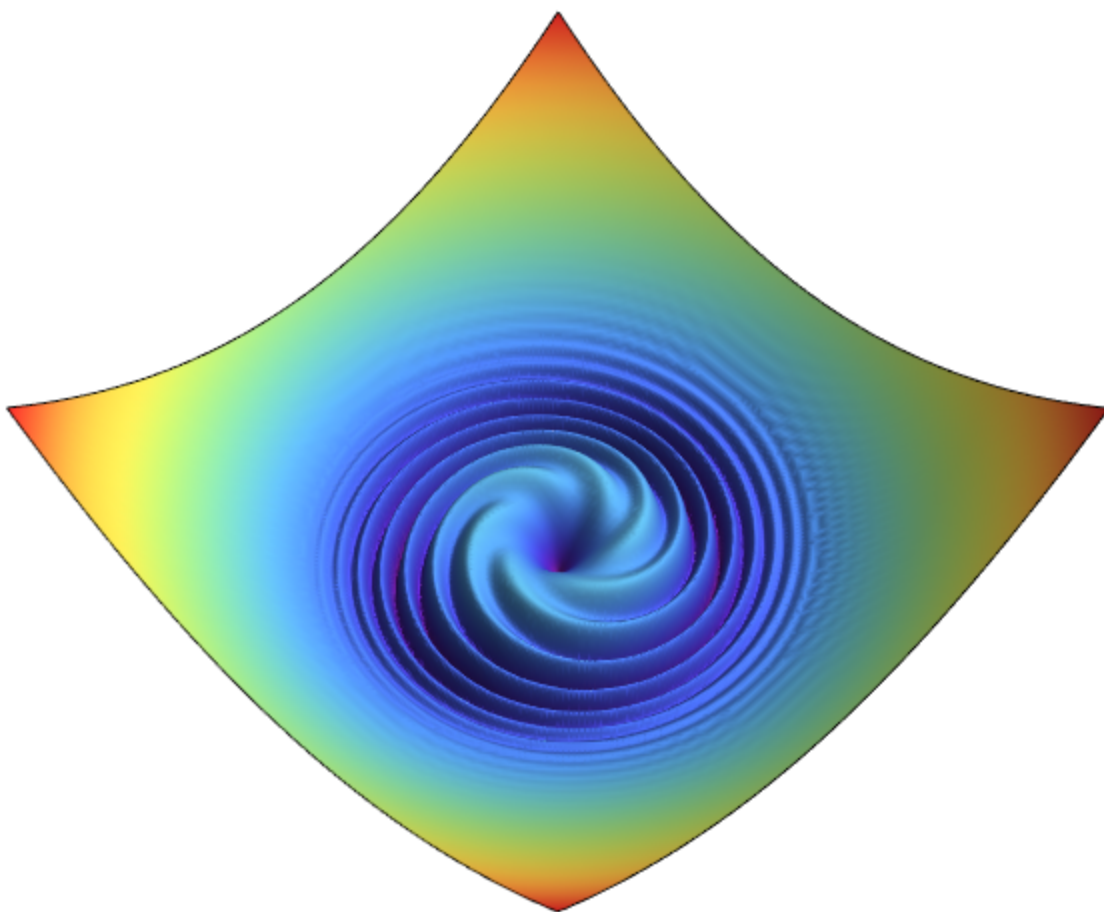
References

[1]   Juan P Torres and Lluis Torner, editors. *Twisted Photons*. Wiley-VCH, 2011.

[2]   Alison M. Yao and Miles J. Padgett. Orbital angular momentum: origins, behavior and applications. *Adv. Opt. Photonics*, 3(2):161, jun 2011.

[3]   David L Andrews and Mohamed Babiker, editors. *The Angular Momentum of Light*. Cambridge, 2013.

[4]   M. Zürch, C. Kern, P. Hansinger, A. Dreischuh, and Ch. Spielmann. Strong-field physics with singular light beams. *Nature Phys.*, 8(10):743–746, aug 2012.

[5]   Carlos Hernández-García, Antonio Picón, Julio San Román, and Luis Plaja. Attosecond Extreme Ultraviolet Vortices from High-Order Harmonic Generation. *Phys. Rev. Lett.*, 111(8):083602, aug 2013.

[6]   Genevieve Gariepy, Jonathan Leach, Kyung Taec Kim, T. J. Hammond, E. Frumker, Robert W. Boyd, and P. B. Corkum. Creating High-Harmonic Beams with Controlled Orbital Angular Momentum. *Phys. Rev. Lett.*, 113(15):153901, oct 2014.

[7]   V. E. Lembessis, M. Babiker, and D. Ellinas. The role of Gouy phase on the mechanical effects of Laguerre-Gaussian light interacting with atoms. In *AIP Conf. Proc.*, page 030009, Gizan, Saudi Arabia, 2016. AIP Publishing.

[8]   Mohammad Vaziri, Mojtaba Golshani, Sozha Sohaily, and Alireza Bahrampour. Electron acceleration by linearly polarized twisted laser pulse with narrow divergence. *Phys. Plasmas*, 22(3):033118, mar 2015.

[9]   Gabriel Molina-Terriza, Juan P Torres, and Lluis Torner. Twisted photons. *Nature Phys.*, 3:305–310, 2007.

[10]   Qingsheng Xiao, Charalambos Klitis, Shimao Li, Yueyang Chen, Xinlun Cai, Marc Sorel, and Siyuan Yu. Generation of photonic orbital angular momentum superposition states using vortex beam emitters with superimposed gratings. *Opt. Express*, 24(4):3168–3176, Feb 2016.

[11]   Gabriel Molina-Terriza, Juan P Torres, and Lluis Torner. Twisted photons. *Nat. Phys.*, 3(5):305–310, may 2007.

[12]   Les Allen and Miles Padgett. The Orbital Angular Momentum of Light: An Introduction. In *Twist. Photons*, pages 1–12. Wiley-VCH Verlag GmbH & Co. KGaA, Weinheim, Germany, 2011.

[13]   Carlos Hernández-García, Jorge Vieira, Jose Mendonça, Laura Rego, Julio San Román, Luis Plaja, Primoz Ribic, David Gauthier, and Antonio Picón. Generation and Applications of Extreme-Ultraviolet Vortices. *Photonics*, 4(2):28, apr 2017.

[14]   Sophia Marriott Lloyd. *Electron Beams with Orbital Angular Momentum*. PhD thesis, University of York, U.K., 2013.

[15]   K.Y. Bliokh, I.P. Ivanov, G. Guzzinati, L. Clark, R. Van Boxem, A. Béché, R. Juchtmans, M.A. Alonso, P. Schattschneider, F. Nori, and J. Verbeeck. Theory and applications of free-electron vortex states. *Phys. Rep.*, 690:1–70, may 2017.

[16]   S. M. Lloyd, M. Babiker, G. Thirunavukkarasu, and J. Yuan. Electron vortices: Beams with orbital angular momentum. *Rev. Mod. Phys.*, 89(3):035004, aug 2017.

[17]   Kayn A Forbes and David L Andrews. Optical orbital angular momentum: twisted light and chirality. *Opt. Lett.*, 43(3):435, feb 2018.

[18]   Andrei Afanasev, Carl E Carlson, Christian T Schmiegelow, Jonas Schulz, Ferdinand Schmidt-Kaler, and Maria Solyanik. Experimental verification of position-dependent angular-momentum selection rules for absorption of twisted light by a bound electron. *New J. Phys.*, 20(2):023032, feb 2018.

[19]   Qingsheng Xiao, Charalambos Klitis, Shimao Li, Yueyang Chen, Xinlun Cai, Marc Sorel, and Siyuan Yu. Generation of photonic orbital angular momentum superposition states using vortex beam emitters with superimposed gratings. *Opt. Express*, 24(4):3168, feb 2016.

[20]   A. E. Siegman. *Lasers*. University Science Books, 1986.

[21]   M.W. Beijersbergen, R.P.C. Coerwinkel, M. Kristensen, and J.P. Woerdman. Helical-wavefront laser beams produced with a spiral phaseplate. *Opt. Commun.*, 112(5-6):321–327, dec 1994.

[22]   G.A. Turnbull, D.A. Robertson, G.M. Smith, L. Allen, and M.J. Padgett. The generation of free-space Laguerre-Gaussian modes at millimetre-wave frequencies by use of a spiral phaseplate. *Opt. Commun.*, 127(4-6):183–188, jun 1996.

[23]   S. S. R. Oemrawsingh, J. A. W. van Houwelingen, E. R. Eliel, J. P. Woerdman, E. J. K. Verstegen, J. G. Kloosterboer, and G. W. 't Hooft. Production and characterization of spiral phase plates for optical wavelengths. *Appl. Opt.*, 43(3):688, jan 2004.

[24]   K. Sueda, G. Miyaji, N. Miyanaga, and M. Nakatsuka. Laguerre-Gaussian beam generated with a multilevel spiral phase plate for high intensity laser pulses. *Opt. Express*, 12(15):3548, 2004.

[25]   N. R. Heckenberg, R. McDuff, C. P. Smith, and A. G. White. Generation of optical phase singularities by computer-generated holograms. *Opt. Lett.*, 17(3):221, feb 1992.

[26]   Laura Rego, Julio San Román, Antonio Picón, Luis Plaja, and Carlos
        Hernández-García. Nonperturbative Twist in the Generation of
        Extreme-Ultraviolet Vortex Beams. *Phys. Rev. Lett.*, 117(16):163202, oct 2016.

[27]   Alex Turpin, Laura Rego, Antonio Picón, Julio San Román, and Carlos
        Hernández-García. Extreme Ultraviolet Fractional Orbital Angular Momentum
        Beams from High Harmonic Generation. *Sci. Rep.*, 7:43888, mar 2017.

[28]   Gerard A. Mourou, Toshiki Tajima, and Sergei V. Bulanov. Optics in the relativistic
        regime. *Rev. Mod. Phys.*, 78(2):309–371, apr 2006.

[29]   A. Di Piazza, C. Müller, K. Z. Hatsagortsyan, and C. H. Keitel. Extremely
        high-intensity laser interactions with fundamental quantum systems. *Rev. Mod.
        Phys.*, 84(3):1177–1228, aug 2012.

[30]   Julius Adams Stratton. *Electromagnetic Theory*. McGraw-Hill, 1941.

[31]   John David Jackson. *Classical Electrodynamics*. Wiley, 1995.

[32]   B. Richards and E. Wolf. Electromagnetic Diffraction in Optical Systems. II.
        Structure of the Image Field in an Aplanatic System. *Proc. R. Soc. A*,
        253(1274):358–379, dec 1959.

[33]   Melvin Lax, William H Louisell, and William B McKnight. From Maxwell to
        paraxial wave optics. *Phys. Rev. A*, 11(4):1365–1370, apr 1975.

[34]   J P Barton and D R Alexander. Fifth-order corrected electromagnetic field
        components for a fundamental Gaussian beam. *J. Appl. Phys.*, 66(7):2800, 1989.

[35]   Scott M Sepke and Donald P Umstadter. Exact analytical solution for the vector
        electromagnetic field of Gaussian, flattened Gaussian, and annular Gaussian laser
        modes. *Opt. Lett.*, 31(10):1447, 2006.

[36] Scott M Sepke and Donald P Umstadter. Analytical solutions for the electromagnetic fields of tightly focused laser beams of arbitrary pulse length. *Opt. Lett.*, 31(17):2589, 2006.

[37] S. X. Hu and Anthony F Starace. Laser acceleration of electrons to giga-electron-volt energies using highly charged ions. *Phys. Rev. E*, 73(6):066502, jun 2006.

[38] Yousef I. Salamin. Fields of a Gaussian beam beyond the paraxial approximation. *Appl. Phys. B*, 86(2):319–326, jan 2007.

[39] Liang-Wen Pi, S. X. Hu, and Anthony F. Starace. Favorable target positions for intense laser acceleration of electrons in hydrogen-like, highly-charged ions. *Phys. Plasmas*, 22(9):093111, sep 2015.

[40] C F R Caron and R M Potvliege. Free-space propagation of ultrashort pulses: Space-time couplings in Gaussian pulse beams. *J. Mod. Opt.*, 46(13):1881–1891, 1999.

[41] Miguel A Bandres and Julio C Gutiérrez-Vega. Higher-order complex source for elegant Laguerre-Gaussian waves. *Opt. Lett.*, 29(19):2213–5, 2004.

[42] Qiang Lin, Jian Zheng, and Wilhelm Becker. Subcycle Pulsed Focused Vector Beams. *Phys. Rev. Lett.*, 97(25):253902, dec 2006.

[43] Alexandre April. Ultrashort, Strongly Focused Laser Pulses in Free Space. In F. J. Duarte, editor, *Coherence and Ultrashort Pulse Laser Emission*, chapter 16, pages 355–382. InTech, 2010.

[44] Andrew Vikartofsky, Liang-Wen Pi, and Anthony F. Starace. Discontinuities in the electromagnetic fields of vortex beams in the complex source-sink model. *Phys. Rev. A*, 95(5):053826, may 2017.

[45] Andrew Vikartofsky, Liang-Wen Pi, and Anthony F Starace. Perturbative representation of ultrashort nonparaxial elegant Laguerre-Gaussian fields. *Phys. Rev. A*, 98, 2018.

[46] G. A. Deschamps. Gaussian beam as a bundle of complex rays. *Electron. Lett.*, 7(23):684–685, November 1971.

[47] S. Y. Shin and L. B. Felsen. Gaussian beam modes by multipoles with complex source points. *J. Opt. Soc. Am.*, 67(5):699–700, May 1977.

[48] A. L. Cullen and P. K. Yu. Complex Source-Point Theory of the Electromagnetic Open Resonator. *Proceedings of the Royal Society of London. Series A Mathematical and Physical Sciences*, 366:155, 1979.

[49] Marc Couture and Pierre A. Belanger. From Gaussian beam to complex-source-point spherical wave. *Phys. Rev. A*, 24(1):355–359, 1981.

[50] Z. Ulanowski and I. K. Ludlow. Scalar field of nonparaxial Gaussian beams. *Opt. Lett.*, 25(24):1792–1794, Dec 2000.

[51] Alexandre April. Nonparaxial elegant Laguerre-Gaussian beams. *Opt. Lett.*, 33(12):1392–1394, 2008.

[52] Vincent Marceau, Alexandre April, and Michel Piché. Electron acceleration driven by ultrashort and nonparaxial radially polarized laser pulses. *Opt. Lett.*, 37(13):2442, 2012.

[53] X. Chu. Evolution of elegant LaguerreâĂŞ-Gaussian beam disturbed by an opaque obstacle. *J. Electromagn. Waves Appl.*, 26(13):1749–1755, sep 2012.

[54] Vincent Marceau, Charles Varin, Thomas Brabec, and Michel Piché. Femtosecond 240-keV Electron Pulses from Direct Laser Acceleration in a Low-Density Gas. *Phys. Rev. Lett.*, 111(22):224801, nov 2013.

[55] A Sell and F X Kärtner. Attosecond electron bunches accelerated and compressed by radially polarized laser pulses and soft-x-ray pulses from optical undulators. *J. Phys. B At. Mol. Opt. Phys.*, 47(1):015601, 2014.

[56] François Fillion-Gourdeau, Catherine Lefebvre, and Steve MacLean. Scheme for the detection of mixing processes in vacuum. *Phys. Rev. A*, 91:031801, Mar 2015.

[57] Vincent Marceau, Pascal Hogan-Lamarre, Thomas Brabec, Michel Piché, and Charles Varin. Tunable high-repetition-rate femtosecond few-hundred keV electron source. *J. Phys. B At. Mol. Opt. Phys.*, 48(4):45601, 2015.

[58] Liang Jie Wong, Byron Freelon, Timm Rohwer, Nuh Gedik, and Steven G Johnson. All-optical three-dimensional electron pulse compression. *New J. Phys.*, 17(1):013051, jan 2015.

[59] Charles Varin, Vincent Marceau, Pascal Hogan-Lamarre, Thomas Fennel, Michel Piché, and Thomas Brabec. MeV femtosecond electron pulses from direct-field acceleration in low density atomic gases. *J. Phys. B At. Mol. Opt. Phys.*, 49(2):024001, 2016.

[60] C. J. R. Sheppard and S. Saghafi. Beam modes beyond the paraxial approximation: A scalar treatment. *Phys. Rev. A*, 57(4):2971–2979, apr 1998.

[61] Colin J. R. Sheppard. High-aperture beams: reply to comment. *J. Opt. Soc. Am. A*, 24(4):1211–1213, Apr 2007.

[62] Simin Feng and Herbert G Winful. Spatiotemporal structure of isodiffracting ultrashort electromagnetic pulses. *Phys. Rev. E*, 61(1):862–873, 2000.

[63] Milton Abramowitz and Irene A. Stegun, editors. *Handbook of mathematical functions*. National Bureau of Standards, 1972.

[64] L. W. Davis. Theory of electromagnetic beams. *Phys. Rev. A*, 19(3):1177–1179, 1979.

[65] G. P. Agrawal and D. N. Pattanayak. Gaussian beam propagation beyond the paraxial approximation. *J. Opt. Soc. Am.*, 69(4):575, 1979.

[66] S R Seshadri. Virtual source for a Laguerre-Gauss beam. *Opt. Lett.*, 27(21):1872–4, 2002.

[67] Miguel a Bandres and Julio C Gutiérrez-Vega. Higher-order complex source for elegant Laguerre-Gaussian waves. *Opt. Lett.*, 29(19):2213–5, 2004.

[68] Takashi Takenaka, Mitsuhiro Yokota, and Otozo Fukumitsu. Propagation of light beams beyond the paraxial approximation. *J. Opt. Soc. Am. A*, 2(6):826–829, 1985.

[69] Erich Zauderer. Complex argument Hermite-Gaussian and Laguerre-Gaussian beams. *J. Opt. Soc. Am. A*, 3(4):465–469, 1986.

[70] Pierre Favier, Kevin Dupraz, Kevin Cassou, Xing Liu, Aurélien Martens, Cheikh Fall Ndiaye, Themistoklis Williams, and Fabian Zomer. Short pulse laser beam beyond paraxial approximation. *J. Opt. Soc. Am. A*, 34(8):1351, aug 2017.

[71] S Y Shin and L B Felsen. Gaussian beam modes by multipoles with complex source points. *J. Opt. Soc. Am.*, 67(5):699, may 1977.

[72] Z Ulanowski and I K Ludlow. Scalar field of nonparaxial Gaussian beams. *Opt. Lett.*, 25(24):1792—-1794, 2000.

[73] Azat M Tagirdzhanov, Alexander S Blagovestchenskii, and Aleksei P Kiselev. âĂŸComplex source' wavefields: sources in real space. *J. Phys. A Math. Theor.*, 44(42):425203, oct 2011.

[74] M V Berry. Evanescent and real waves in quantum billiards and Gaussian beams. *J. Phys. A. Math. Gen.*, 27(11):L391–L398, 1994.

[75] John Lekner. TM, TE and 'TEM' beam modes: exact solutions and their problems. *J. Opt. A: Pure Appl. Opt.*, 3(5):407–412, 2001.

[76] C J R Sheppard. Comment on 'TM, TE and 'TEM' beam modes: exact solutions and their problems'. *J. Opt. A: Pure Appl. Opt.*, 4:217–218, 2002.

[77] John Lekner. Reply to 'Comment on "TM, TE and 'TEM' beam modes: exact solutions and their problems'". *J. Opt. A: Pure Appl. Opt.*, 4:219–220, 2002.

[78] S Saghafi and C J R Sheppard. Near field and far field of elegant Hermite-Gaussian and Laguerre- Gaussian modes. *J. Mod. Opt.*, 45(10):1999–2009, 1998.

[79] Miguel A Porras. Ultrashort pulsed Gaussian light beams. *Phys. Rev. E*, 58(1):1086, 1998.

[80] J.-Y. Lu and J.F. Greenleaf. Nondiffracting X waves-exact solutions to free-space scalar wave equation and their finite aperture realizations. *IEEE Trans. Ultrason. Ferroelectr. Freq. Control*, 39(1):19–31, jan 1992.

[81] Colin J R Sheppard. Bessel pulse beams and focus wave modes. *J. Opt. Soc. Am. A*, 18(10):2594–2600, 2001.

[82] Kevin J. Parker and Miguel A. Alonso. Longitudinal iso-phase condition and needle pulses. *Opt. Express*, 24(25):28669, 2016.

[83] John David Jackson. *Classical Electrodynamics*. Wiley, 1995.

[84] Julius Adams Stratton. *Electromagnetic Theory*. McGraw-Hill, 1941.

[85] A. E. Siegman. *Lasers*. University Science Books, Mill Valley, CA, 1986.

[86] Sadri Hassani. *Mathematical Methods: For Students of Physics and Related Fields*. Springer, New York, 2009.

[87] Zhongyang Wang, Zhengquan Zhang, Zhizhan Xu, and Qiang Lin. Space-time profiles of an ultrashort pulsed Gaussian beam. *IEEE J. Quantum Electron.*, 33(4):566–573, apr 1997.

[88] Milton Abramowitz and Irene A. Stegun. *Handbook of mathematical functions.* Dover Publications, New York, 1972.

[89] Harry Bateman and Arthur Erdélyi. *Higher transcendental functions*, volume 3. 01 1953.

[90] I. S. Gradshteyn and Iosif M. Ryžik. *Table of Integrals, Series, and Products.* Academic Press, 7th ed edition, 2007.

[91] A A Ishchenko, S A Aseyev, V N Bagratashvili, V Ya Panchenko, and E A Ryabov. Ultrafast electron diffraction and electron microscopy: present status and future prospects. *Physics-Uspekhi*, 57(7):633–669, jul 2014.

[92] Matthew Weyland and Paul Midgley. Electron Tomography. In *Transm. Electron Microsc.*, chapter 12, pages 343–376. Springer, 2016.

[93] C. Pellegrini, A. Marinelli, and S. Reiche. The physics of x-ray free-electron lasers. *Rev. Mod. Phys.*, 88(1):015006, mar 2016.

[94] A.W. Chao and W. Chou. *Reviews of Accelerator Science and Technology: Volume 9: Technology and Applications of Advanced Accelerator Concepts.* World Scientific, 2017.

[95] Masashi Mizumoto, Yoshiko Oshiro, Toshiyuki Okumura, Nobuyoshi Fukumitsu, Haruko Numajiri, Kayoko Ohnishi, Teruhito Aihara, Hitoshi Ishikawa, Koji Tsuboi, and Hideyuki Sakurai. Proton Beam Therapy for Hepatocellular Carcinoma: A Review of the University of Tsukuba Experience. *Int. J. Part. Ther.*, 2(4):570–578, mar 2016.

[96] S. X. Hu and Anthony F. Starace. GeV Electrons from Ultraintense Laser Interaction with Highly Charged Ions. *Phys. Rev. Lett.*, 88(24):245003, jun 2002.

[97] Eric Esarey and Mark Pilloff. Trapping and acceleration in nonlinear plasma waves. *Phys. Plasmas*, 2(5):1432–1436, may 1995.

[98] Devki Nandan Gupta, Niti Kant, Dong Eon Kim, and Hyyong Suk. Electron acceleration to GeV energy by a radially polarized laser. *Phys. Lett. A*, 368(5):402–407, aug 2007.

[99] A Sell and Franz X. Kärtner. Attosecond electron bunches accelerated and compressed by radially polarized laser pulses and soft-x-ray pulses from optical undulators. *J. Phys. B*, 47(1):015601, jan 2014.

[100] C I Moore, A Ting, T Jones, E Briscoe, B. Hafizi, R F Hubbard, and P Sprangle. Measurements of energetic electrons from the high-intensity laser ionization of gases. *Phys. Plasmas*, 8(5):2481–2487, may 2001.

[101] E. Esarey, C. B. Schroeder, and W. P. Leemans. Physics of laser-driven plasma-based electron accelerators. *Rev. Mod. Phys.*, 81(3):1229–1285, aug 2009.

[102] P.M. Woodward. A method of calculating the field over a plane aperture required to produce a given polar diagram. *J. Inst. Electr. Eng. - Part IIIA Radiolocation*, 93(10):1554–1558, 1946.

[103] J.D. Lawson. Lasers and Accelerators. *Nucl. Sci. IEEE Trans.*, 26(3):4217–4219, 1979.

[104] Robert B. Palmer. A laser-driven grating LINAC. *Part. Accel.*, 11:81–90, 1980.

[105] Charles Varin, Michel Piché, and Miguel A. Porras. Acceleration of electrons from rest to GeV energies by ultrashort transverse magnetic laser pulses in free space. *Phys. Rev. E*, 71(2):026603, feb 2005.

[106] W.H. Press, B.P. Flannery, S.A. Teukolsky, and W.T. Vetterling. *Numerical Recipes in FORTRAN 77: Volume 1, Volume 1 of Fortran Numerical Recipes: The Art of Scientific Computing*. Cambridge University Press, 2nd edition, 1992.

[107] Harjit Singh Ghotra and Niti Kant. Sensitiveness of axial magnetic field on electron acceleration by a radially polarized laser pulse in vacuum. *Opt. Commun.*, 356(6):118–122, dec 2015.

[108] Steven Roman. The Formula of FAA Di Bruno. *Am. Math. Mon.*, 87(10):805, dec 1980.

[109] Warren P Johnson. The Curious History of Faa di Bruno's Formula. *Am. Math. Mon.*, 109(3):217, mar 2002.

[110] Harley Flanders. From Ford to Faà. *Am. Math. Mon.*, 108(6):559, jun 2001.

[111] L. Hernández Encinas, A. Martín Del Rey, and J. Muñoz Masqué. Faà di Bruno's formula, lattices, and partitions. *Discret. Appl. Math.*, 148(3):246–255, 2005.